Rapid solid-state metathesis reactions for the formation of cobalt-iron monoboride solid-solutions and investigation of their water splitting electrocatalytic activity

Janaka P. Abeysinghe and Edward G. Gillan*

Department of Chemistry, University of Iowa, Iowa City, Iowa 52242 USA

Edward Gillan (ORCID: 0000-0002-2047-0929) Email: edward-gillan@uiowa.edu
Janaka Abeysinghe (ORCID: 0000-0002-0444-3525) Email: janaka-abeysinghe@uiowa.edu

Abstract

Metal borides have received increased attention as potentially robust water splitting electrocatalysts. Some studies have reported synergistic electrocatalytic effects on hydrogen and/or oxygen evolution reactions (HER/OER) using mixed metal borides. This report describes the single-step, solvent-free, and rapid (few seconds) synthesis of a series of crystalline $Co_{1-x}Fe_xB$ (x = 0-1) solid solutions in high isolated product yields (>80%) from exothermic, self-propagating solid-state metathesis (SSM) reactions between metal halides and elemental Mg/B reactants. Powder X-ray diffraction shows the $Co_{1-x}Fe_xB$ products are single-phase with crystallite sizes near 60 nm. SEM/EDS and elemental analysis indicate products contain homogeneous Co/Fe distributions and form large micrometer-sized particle aggregates. The electrocatalytic HER with these well-structured crystalline $Co_{1-x}Fe_xB$ materials in 1 M KOH shows increased HER activity at lower applied potentials as cobalt content increases. The OER activity of $Co_{1-x}Fe_xB$ also generally shows improvement with increased cobalt content. Crystalline $Co_{1-x}Fe_xB$ catalysts exhibit good long-term 24 h HER and OER stability in 1 M KOH. Post-electrochemistry $Co_{1-x}Fe_xB$ analyses confirm the retention of product crystallinity after long term electrocatalysis.

Keywords: crystalline metal borides, solid-state metathesis, exothermic, thermochemistry, cobalt boride, iron boride, metal boride solid-solutions, hydrogen evolution electrocatalysis, oxygen evolution electrocatalysis

Introduction

Providing sustainable energy alternatives to fossil fuels using renewable, low-cost, and environmentally friendly energy sources is a daunting challenge because global energy demand is expected to double or triple in the next few decades.[1, 2] Hydrogen (H_2) is a major contender as a future fuel due to its high gravimetric energy density, renewable potential, and environmentally friendly use, and many countries have begun to examine hydrogen-fueled energy applications.[1, 2] Several significant barriers exist for large-scale and sustained H_2 consumption including development of efficient, low-cost, and environmentally benign H_2 production methods and design of gravimetrically useful H_2 storage containment. Three methods used for large scale H_2 production today are natural gas reforming, coal gasification, and water electrolysis. While water electrolysis only accounts for a few percent of global hydrogen production, it is potentially the most sustainable, lowest greenhouse gas emission H_2 production process. Water electrolysis ($H_2O \rightarrow H_2 + ½O_2$) consists of two chemical reactions: the hydrogen evolution reaction (HER) and the oxygen evolution reaction (OER). A major issue with water electrolysis is that currently useful electrocatalysts for HER and OER are very expensive and rare (*e.g.*, Pt, Pd, IrO_2, and RuO_2). Extensive research is being conducted to identify robust electrocatalysts for water electrolysis that use more earth abundant and less expensive transition-metals, particularly those from the 3d series (*e.g.*, Cr to Cu).

Cobalt and iron compounds have been widely studied as HER and OER electrocatalysts. Some iron and/or cobalt transition metal phosphides,[3, 4] oxide/hydroxides,[5, 6] sulphides,[7, 8] nitrides,[9, 10] and borides[11, 12] show moderate to good electrocatalytic activity for water electrolysis. Metal borides are an intriguing class of electrocatalyst materials because of their properties such as high electrical conductivity, thermal and corrosion resistance, high melting temperatures (>1000 °C), and chemical stability.[13-21] Several metal borides in crystalline or amorphous structures (*e.g.*, CoB_x,[22] NiB_x,[23] MoB_x,[24] VB_2,[25] WB_x[26]) have been studied as electrocatalysts for HER and/or OER. Some boride studies have focused on improving the electrocatalytic activity of metal borides via control of particle morphology (*e.g.*, nanoparticles, nanosheets or amorphous structures), synthesis of more complex mixed metal borides and composites, and use of catalyst support (*e.g.*, Ni mesh, carbon cloth).[27-31]

Metal borides can form a range of structures from metal-rich to boron-rich compositions that contain metal-metal interactions, boron-boron covalent bonds, and metal-boron bonds leading to diverse physical and chemical properties.[32] Typical metal boride syntheses either produce poorly crystalline products or require high temperature synthesis or post-reaction annealing to obtain crystalline products. Metal boride syntheses use traditional high-temperature elemental reactions and lower temperature precursor approaches, including arc melting,[33, 34] reactive sintering,[35] solution-phase synthesis,[36-38] mechanochemical methods,[39] metal flux

synthesis,[40, 41] electrodeposition,[42] electroless deposition,[43] molten salt synthesis,[26, 44] and hydrothermal reactions.[45] Several of these reactions use relatively inert elemental boron (mp ~2000 °C) as a reactant in metal boride synthesis. A recent iodide exchange synthetic strategy with BI_3 and metal powders produced a range of metal-rich and boride-rich metal borides at moderate ~600-800 °C temperatures.[46]

An alternative to externally heated materials synthesis that uses thermochemical energy provided by chosen reactants is known as solid-state metathesis (SSM).[47-50] Self-propagating SSM reactions can be initiated by brief reactant heating with a heated filament (ignition reaction) and the exothermic energy released is sufficient to initiate further reactions from surrounding reactants. SSM reactions are complete in a few seconds and usually yield polycrystalline micrometer-sized particle aggregates. The exothermicity of SSM reactions is often dictated by the formation of a stable byproduct salt (e.g., NaCl or $MgCl_2$) that becomes briefly molten during the reaction and can facilitate diffusion and crystallization.[48] Ignition SSM reactions have been used to synthesize a variety of transition metal compounds including metal phosphides,[51, 52] nitrides,[53, 54] oxides,[55, 56] sulphides,[57] and few ternary mixed metal and non-metal compounds.[57-60] Typical SSM approaches to metal boride synthesis rely on either ignition or furnace initiated reactions between metal halides and MgB_2.[24, 61] Our recent work showed that a rapid SSM strategy is successful with three mixed reactants [metal chloride, magnesium powder, and amorphous boron] to produce crystalline FeB, CoB, and NiB.[62] Several of these metal borides show moderate activity in HER and OER electrocatalysis.

Some recent studies have measured HER or OER electrocatalytic enhancements for mixed metal borides over their binary boride parent structures that are ascribed to synergistic effects from both metals being present on the boride surface. The mixed metal borides' increased catalytic activity has also been linked to the formation of specific morphologies[63, 64] or favorable alterations in electronic structure or conductivity.[11, 12, 65] Co-Fe-B structures have been produced as crystalline or amorphous phases via liquid phase synthesis methods (chemical reduction, hydrothermal reactions, and molten-salt assisted borothermal reduction), but post-reaction calcination is often required to obtain crystalline metal borides.[11, 12, 63-67] Some prior studies used amorphous or poorly crystalline mixed-metal borides, making it difficult to clearly compare catalytic metal boride activities from different studies.

Since Co and Fe are two relatively earth-abundant metals, a clear comparison of well-structured Co-Fe-B solid-solution effects on HER and OER electrocatalysis is highly desirable. Our prior SSM work showed reaction success using mixed Mg/B reactants for metal boride synthesis.[62] In this study we describe the rapid SSM synthesis of a wide range of crystalline $Co_{1-x}Fe_xB$ solid solutions (x = 0-1) between mixtures of $FeCl_2/CoCl_2$ and Mg/B powders. This work demonstrates that a surprising level of atomic mixing is

possible in rapid (few seconds) SSM reactions using four reactants with five different elements, to produce crystalline $Co_{1-x}Fe_xB$ and byproduct $MgCl_2$. Powder X-ray diffraction, SEM/EDS, XRF, and bulk elemental analysis support solid-solution formation with compositions that closely reflect the ratios of elements in the reaction mixture. The $Co_{1-x}Fe_xB$ materials were examined in HER and OER electrocatalysis in KOH electrolyte to identify trends in activity versus composition.

Experimental Procedures

Starting materials and reagents. Anhydrous commercial reagents were stored in an inert atmosphere glove box and utilized as purchased: $CoCl_2$ (Alfa-Aesar, 99.7%), $FeCl_2$ (Aldrich Chemicals, 98%), Mg (Sigma-Aldrich, 99.5%, powder, -325 mesh), and amorphous B (Alfa-Aesar, 95-97%, powder (APS < 1 micron)). 0.1 M HCl (Fisher Scientific, 12.4 M diluted with DI H_2O) was used for the product washing. ICP calibration standards were prepared by diluting Co (Thermo Fisher Scientific 999 ± 5 μg mL^{-1}), Fe (Thermo Fisher Scientific 1003 ± 6 μg mL^{-1}), B (Alfa Aesar 1000 μg mL^{-1}), Mg (Thermo Fisher Scientific 999 ± 5 μg mL^{-1}) in 5 vol% HNO_3 (from Sigma-Aldrich, 14 M and 18 MΩ ultrapure water). Materials used for electrochemical studies: synthetic graphite powder (<20 μm, Sigma-Aldrich), paraffin wax (mp ≥ 65 °C, Sigma-Aldrich), 1.0 M KOH (Sigma-Aldrich, KOH pellets dissolved with 18 MΩ ultra-pure water), 10% Pt on Vulcan XC-72 carbon (C1- 10 fuel cell grade, E-Tek), and RuO_2 (Alfa-Aesar, 99.9%).

Safety considerations. SSM reactions are highly exothermic (and potentially explosive) reactions that, according to theoretical calculations, can release >300 kJ/mol energy into the surrounding environment, achieving reaction temperatures of over 1000 °C in a matter of seconds. Before and during any SSM reaction, the following precautions should be taken: understand its reaction exothermicity and adiabatic (maximum) temperature, use a protective shield (outer closed container) around the reaction vessel, and run new reactions on a small scale (<1 gram of reactants) until the energetic hazards are better understood.

Rapid SSM synthesis of CoB, FeB, and $Co_{1-x}Fe_xB$ solid solutions. CoB and FeB were synthesized using three-component displacement and redox reactions between $CoCl_2$ or $FeCl_2$ with Mg/B mixtures as we previously reported.[62] The total mass of the reactants used was approximately one gram. Typical reactant amounts used for CoB and FeB formation were 6 mmol MCl_2 ($CoCl_2$ or $FeCl_2$) with 6 mmol Mg and 12 mmol B. In the case of $Co_{1-x}Fe_xB$ solid solution synthesis, four-component displacement and redox reactions between $CoCl_2$/$FeCl_2$ and Mg/B mixtures were performed. The reaction stoichiometries were chosen to produce a 1:1:1 molar ratio of $Co_{1-x}Fe_xB$, B, and $MgCl_2$ salt byproduct. The typical reactant amounts used in these SSM reactions were 5 mmol MCl_2 (1-x $CoCl_2$ + x $FeCl_2$ for x = 0.2, 0.4, 0.5, 0.6, and 0.8) with 5 mmol Mg and 10 mmol B. Because rapid SSM reactions are complete in seconds and 3 or

4 reactants are involved in the reaction, an intimate mixing of reactants was performed to promote complete and homogeneous reactions. In an argon-filled glove box, $CoCl_2$, $FeCl_2$, Mg, and B powders were added sequentially to an agate mortar and ground together for 30-40 seconds after each reactant addition to obtain a homogeneous powder mixture. The reactant mixture was transferred to a cone-shaped quartz crucible (top OD = 3.6 cm, bottom OD = 1.3 cm, height = 4.9 cm), which was placed in a cylindrical stainless-steel reactor (ID = 3.8 cm, OD = 5.0 cm, height = 6.2 cm) with a loose screwcap lid.[62] A coiled nichrome wire with five loops was connected to two electrical feedthroughs on the lid to increase contact with the reactant powder mixture. The closed reactor was moved from the glove box to a fume hood. A Variac transformer set to 15.5 V was connected to the nichrome filament and turned on for about 6-8 seconds to resistively heat the filament. Within ~3 s, resistive heating raises the temperature of the nichrome wire to 750 – 800 °C. Wisps of white "smoke" emerging from the reactor lid indicated reaction initiation/propagation. After the SSM reactions were cooled to near room temperature, the reactor was opened and its contents, a dark product and white salt byproduct, were ground to a fine powder. Unreacted starting materials and byproduct $MgCl_2$ were removed by washing with 50 mL of stirred 0.1 M HCl for 30 min, followed by washing with 100 mL distilled water for 30 min. After each washing step, the product powders were isolated by centrifugation. The products were oven-dried for 20 minutes in air at 130 °C and mass yields were calculated using the recovered product mass and theoretical masses of metal boride products.

Sample characterization. Powder X-ray diffraction (XRD) was performed to characterize the structure and crystallinity of mixed metal boride products using a Bruker D8 DaVinci diffractometer with nickel-filtered Cu Kα X-ray irradiation (40 kV, 40 mA) from 5-80 degrees 2θ (0.05° step size). Ground metal boride powders were placed on a vacuum greased glass slide. Reference XRD patterns and crystal structure representations were generated using CrystalMaker software (http://www.crystalmaker.com/index.html) and literature data for orthorhombic FeB, CoB, and $Co_{0.5}Fe_{0.5}B$.[68-70] CrystalDiffract software was used to match experimental data to simulated ternary $Co_{1-x}Fe_xB$ diffraction patterns based on a $Co_{0.5}Fe_{0.5}B$ crystal reference pattern (PDF 01-079-2846) (http://www.crystaldiffract.com/index.html). The morphologies and particle sizes of the products were identified using a Hitachi S-4800 field emission scanning electron microscopy (SEM) at 2-3 kV and Hitachi S-7800 transmission electron microscopy (TEM) with an accelerating voltage of 80 kV. Ground samples were affixed to carbon tape on aluminum stubs for SEM analysis or sonicated in methanol and drop cast on carbon coated Ni mesh grids for TEM analysis. Energy dispersive spectroscopy (EDS) with SEM was used to perform semiquantitative analysis of Co/Fe ratios and qualitative element specific mapping on bulk powders by metal borides affixed to carbon wax electrode tips. X-ray fluorescence spectroscopy (XRF) was used to further evaluate the quantitative elemental analysis of mixed metal borides (Rigaku ZSX Primus IV dispersive X-ray fluorescence spectrometer).

Metal boride powders are compressed to 10,000 psi in a hydraulic press to form compact pellets for XRF analysis. A Quantachrome Nova 1200 nitrogen surface area analyzer was used to quantify surface areas for vacuum dried samples (120 °C for more than 3 hours). Inductively coupled plasma-optical emission spectroscopy (ICP-OES) measurements for bulk elemental analysis were performed using PerkinElmer Optima 7000 DV ICP-OES spectrometer. The metal boride samples were dissolved in heated 5 mL concentrated HNO_3 and diluted to 100 mL with 18 MΩ ultrapure water. Linear elemental calibration curves were produced from commercial ICP standards (Fe, Co, B, and Mg) diluted in 5% (v/v) HNO_3.

Working electrode preparation. Working carbon wax (C_{wax}) electrodes for electrocatalytic measurements were prepared using a graphite/paraffin wax mixture (50% graphite : 50% wax) inside PTFE tubes as previously reported by our group.[3, 62, 71] These C_{wax} electrodes allow direct electrocatalyst-electrolyte contact without the need for binders or conducting coatings. Working electrode tips were 1.4 cm long with a 3.2 mm ID, and 6.4 mm OD, and a 0.080 cm^2 geometrical surface area. A brass current collector rod was embedded into the blank C_{wax} electrode tip and submerged in a pre-heated water bath (55 °C) for 20 minutes prior to catalyst loading. Brief sonication of ~10mg of the catalyst powder with 100 µL of methanol was used to make a homogeneous catalyst suspension, and ~20-30 µL aliquots were placed in an aluminum weigh boat to air dry. The air-dried catalyst-containing aluminum weigh boat was tared in a microbalance before being placed in a preheated hot plate (55 °C). The softened C_{wax} blank electrode tips were gently pressed onto the catalyst, and excess catalyst powder on the PTFE tip was carefully removed and returned to the aluminum weigh boat. The electrode tip was pressed several times in a clear space in the weigh boat to ensure that the sample powders were firmly embedded on the wax. Following catalyst loading, the aluminum weigh boat was weighed on the previously tared microbalance, and the mass of the loaded catalyst was recorded. Sample mass loadings on the electrode typically ranged from ~0.5–2.0 mg. The open end of the brass connecting rod was connected to the potentiostat (**Figure S1**).

Electrochemical measurements. Electrochemical measurements were performed in a 1.0 M KOH electrolyte solution using a three-electrode cell with a C_{wax} working electrode, Hg/HgO reference electrode (20% KOH), and a graphite rod counter electrode (Alfa Aesar, 6.2 mm diam., SPK grade, 99.9995%). The Hg/HgO electrode potential values were converted to standard hydrogen electrode potentials using the $E_{RHE} = E_{Hg/HgO} + 0.059pH + E_{0\ Hg/HgO}$, with pH = 14 and $E_{0\ Hg/HgO} = 0.098$ V. 1.0 M KOH electrolyte pH values were measured with a pH meter. All potentials are referenced to RHE values unless indicated. Reported current densities are scaled relative to the geometric area of the C_{wax} electrode (0.080 cm^2). The electrodes were attached to a PINE WaveDriver 200 bipotentiostat and placed in a single compartment cell, which consists of a Pyrex beaker and a PTFE lid similar to our prior work.[3, 62] A magnetic stir bar was placed ~6

mm away from the working electrode and spun at ~500 RPM throughout the electrochemical tests to remove gas bubbles (H_2 or O_2) that formed on the electrode surface. The electrolyte solutions were purged with O_2 or H_2 gases that were pre-humidified by passing them through a water bubbler. The gas purging started 30 minutes before the electrochemical measurements and lasted the duration of the experiment. The activity and stability of metal boride HER and OER were assessed using 50 linear sweep voltammograms (LSVs) in H_2 (ultra-high purity 99.999%, Praxair) purged electrolyte for HER or O_2 (99.5% purity, Praxair) purged electrolyte for OER. The LSV data were collected without *iR* compensation and later manually corrected for 85% *iR* compensation. The measured cell resistances for catalysts on C_{wax} electrodes in 1.0 M KOH were ~15-30 Ω. Data for standard 10% Pt/C HER and RuO_2 OER catalysts on C_{wax} electrodes were obtained for comparison.

The long-term activity of the metal borides as HER and OER catalysts was investigated using 24-hour time base chronoamperometry studies (CA) at constant potentials in 1.0 M KOH with selected applied potentials targeting a current density of ~10 mA cm^{-2}. The electrochemical surface areas (ECSA) of each metal boride were determined by measuring the double-layer capacitance (C_{dl}) in the non-Faradaic region (-100 to 300 mV vs RHE) with H_2 gas purging before HER CA measurements. ECSA analysis was performed using cyclic voltammetry (CV) data at scan rates of 10, 25, 50, 75, and 100 mV s^{-1}. Calculated capacitance values were converted to approximate areas using a 35 μF/cm^2 relationship.[72]

Post-electrochemistry analysis of metal boride catalyst particles on C_{wax} electrodes. The crystallinity of CoB, FeB, and $Co_{1-x}Fe_xB$ catalysts on C_{wax} electrode tips after 24 h CA experiments was examined using powder XRD (27-60° 2θ, 0.02° step size). XRD samples were prepared from post-electrochemical electrodes by cutting ~1 mm slices from the end of the C_{wax} electrode with a thin surface coating of embedded metal boride powders and placing them in the well of an XRD sample holder for XRD analysis. SEM imaging and EDS mapping were also obtained for the catalysts embedded on C_{wax} after CA experiments. XRD and EDS mapping for metal boride powders embedded on C_{wax} electrode tips prior to electrochemical use were also collected for comparison.

Results and Discussion

Solid-solution $Co_{1-x}Fe_xB$ metal boride synthesis via SSM reactions. Previous studies have shown that solvent-free rapid ignition SSM reactions are effective for the synthesis of several binary transition-metal borides (**Table S1**). The formation of a highly stable (ΔH_f = -644 kJ/mol) $MgCl_2$ salt in addition to the metal boride product drives these SSM reactions. Most reported SSM reactions for MB_x synthesis use an MgB_2 reactant and furnace heating to overcome reaction activation energies and promote atom diffusion

and boride crystallization. Some challenges with rapid ignition SSM reactions are the potential for heterogeneous mixing in the rapidly cooled product and non-propagation for stable reactants with high activation energies or for low exothermicity reactions. In select cases, local ignition heating can lead to successful self-propagating SSM metal boride reactions, such as in our prior work with MCl_2 reacting with either MgB_2 or Mg/2B mixtures to form FeB, NiB, and CoB.[62] The Mg/2B reactions are more exothermic than corresponding MgB_2 reactions and result in high yields of crystalline metal borides. In this study, we demonstrate the successful use of exothermic ignition SSM reactions between well-mixed MCl_2/Mg/B reactants for the rapid formation of crystalline $Co_{1-x}Fe_xB$ solid solution borides. The SSM reactions targeting CoB, FeB, and $Co_{1-x}Fe_xB$ solid solutions are salt-balanced to form $MgCl_2$ (**Equation 1**).

$$(1\text{-}x)\ CoCl_2(s) + x\ FeCl_2(s) + Mg(s) + 2B(s) \rightarrow \mathbf{Co_{1-x}Fe_xB(s)} + B(s) + MgCl_2(s) \quad (1)$$
$$(x = 0, 0.2, 0.4, 0.5, 0.6, 0.8, 1)$$

Consistent with our prior rapid SSM metal boride work, these rapid SSM reactions were performed with excess amorphous boron reactant as it is necessary to produce single-phase CoB and FeB from rapid MCl_2/Mg/2B reactions and avoid metal-rich phases (*e.g.*, Fe_2B).[62] Most of the excess boron in the product remains as inert amorphous boron rather than being converted to soluble forms of boron such as B_2O_3 or BCl_3.[62] The exothermic reactions between mixed metal reactants shown in **Equation 1** should achieve a molten salt intermediate state allowing for rapid reaction, heating, and crystallization of metal borides as shown schematically in **Figure 1**. A range of elemental or ionic intermediates may be present in the hot wavefront.

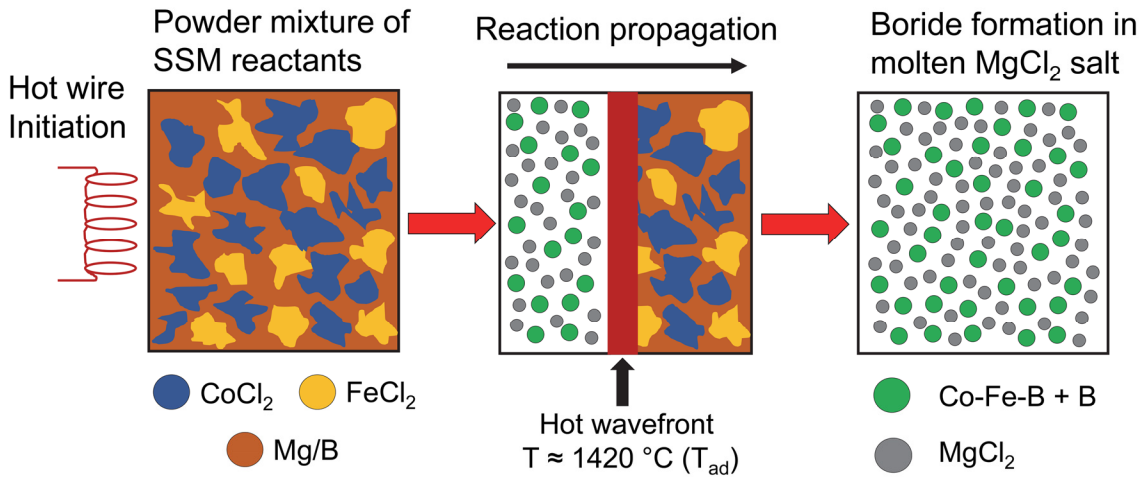

Figure 1. Illustration of hot wire initiation of mixtures of cobalt and iron dichlorides with magnesium reductant and amorphous boron in a rapidly self-propagating and exothermic SSM reaction.

The wide compositional range of SSM reactions described by **Equation 1** all rapidly initiate and enter a self-propagating state, yielding a dark product and a white $MgCl_2$ transport (**Figure 2A, B**). A series of black to brown products were isolated after 0.1 M HCl and DI water washing (**Figure 2C**). A wide range of crystalline $Co_{1-x}Fe_xB$ materials (x = 0.2, 0.4, 0.5, 0.6, 0.8) were rapidly synthesized in high yields (>80%) using varying ratios of $CoCl_2$ and $FeCl_2$ with Mg/2B balanced SSM reactions according to **Equation 1**.

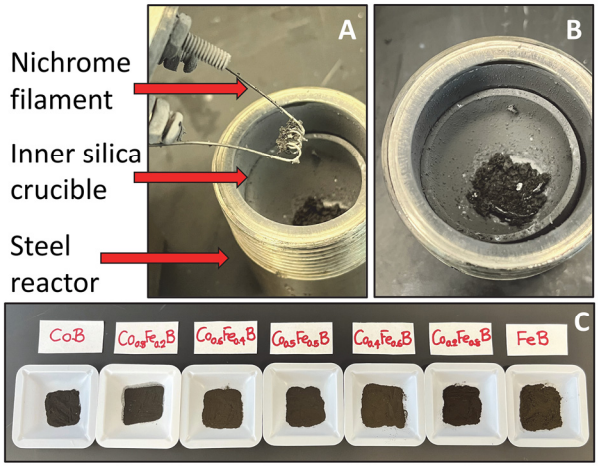

Figure 2. (A) After SSM reaction completion, some metal boride product particles are fused to the nichrome ignition wire. (B) Black metal boride particles are at the bottom of the reaction vessel with white $MgCl_2$ deposits. (C) Images of black to brown $Co_{1-x}Fe_xB$ products ranging from CoB (far left) to FeB (far right) with solid solutions in between these end members.

The single metal (x=0 or 1) Mg/2B reactions produce CoB (PDF 04-003-2122) and FeB (PDF 04-013-1637), which both crystallize in similar orthorhombic structures but with different space groups (CoB-Pbnm, FeB-Pnma, **Table S2**), leading to different lattice orientations and (hkl) designations for some peaks (**Figure 3**). One useful feature of the CoB and FeB powder X-ray diffraction (XRD) patterns that can help identify the transition of CoB to FeB to solid-solution metal borides is that overlapped (111) and (120) XRD peaks at 41.3° in CoB systematically separate into two (111) and (201) peaks with the incorporation of iron into the $Co_{1-x}Fe_xB$ structure.

Powder XRD shows the $Co_{1-x}Fe_xB$ products each appear as single-phase structures with expected peak shifts for solid-solution mixing (**Figure 3**). XRD peak positions of synthesized $Co_{1-x}Fe_xB$ solid solution products shift from CoB and FeB peak positions with increasing iron in the reactant mixture, but overall XRD patterns are comparable to CoB and FeB end members. A literature reference pattern for $Co_{0.5}Fe_{0.5}B$ (PDF 01-079-2846) is a very good match to SSM synthesized $Co_{0.5}Fe_{0.5}B$ (**Table S2** and **Figure S2**) and

this structure was used as the basis for determining the lattice parameters from XRD peak positions of the other $Co_{1-x}Fe_xB$ products (**Tables S2** and **S3**). The systematic shifting of XRD peak positions and lattice parameters with changes in ideal x value in $Co_{1-x}Fe_xB$ is shown graphically in **Figure 4**, where two lattice parameters decrease and one increases with increases in cobalt content, leading to a net decrease in unit cell volume (and as expected from atomic radii Fe > Co). A plot of unit cell parameters versus ideal Co content shows a linear correlation (**Figure 4**) and a Vegard's Law like composition/lattice parameter dependence that supports the successful formation of a full range of $Co_{1-x}Fe_xB$ solid solutions from these rapid SSM reactions. To our knowledge, this is the first study that demonstrates crystalline solid-solution metal boride formation from rapid ignition SSM reactions.

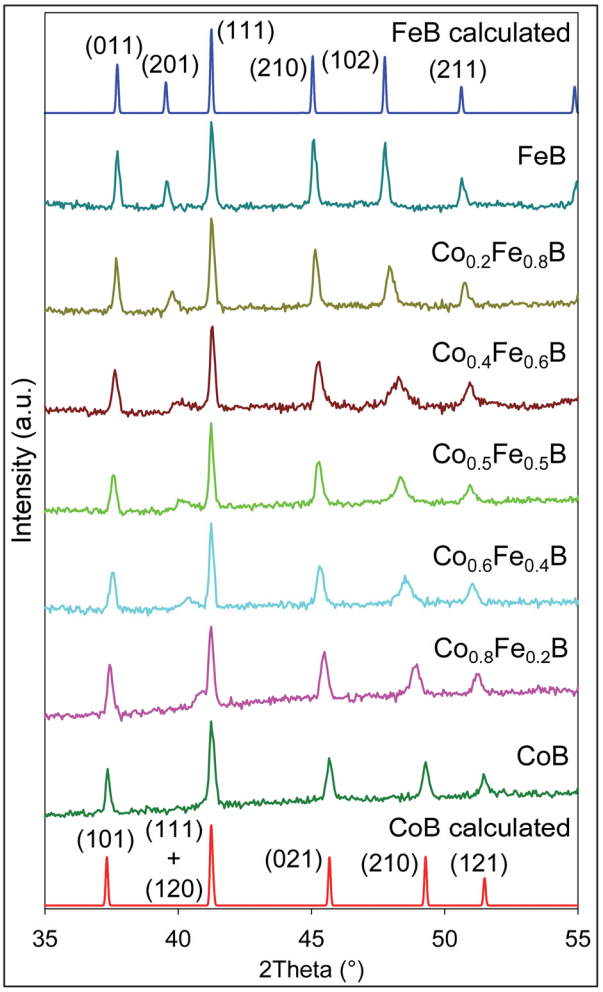

Figure 3. Powder XRD stack plot of orthorhombic CoB, FeB, and $Co_{1-x}Fe_xB$ solid solutions. Miller indices (hkl) are listed for FeB and CoB end members.

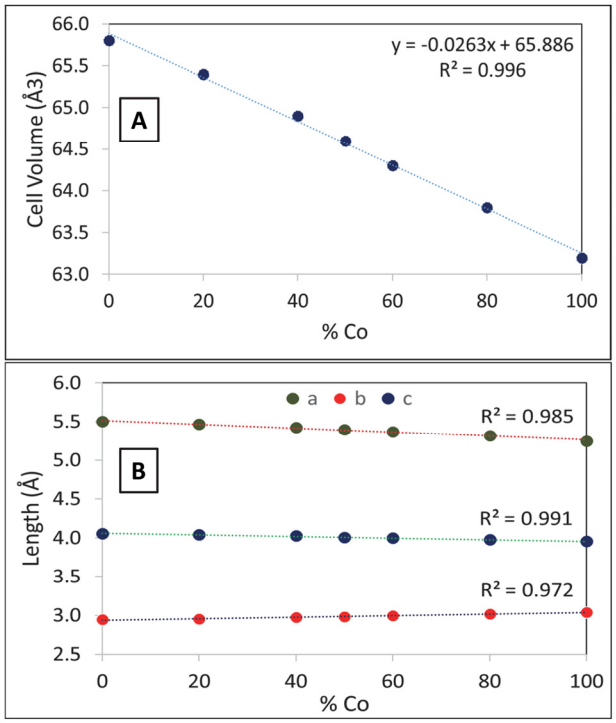

Figure 4. Ideal percent Co in $Co_{1-x}Fe_xB$ versus (A) unit cell volume, (B) unit cell parameters (a, b, c). Linear regression lines for each data set are shown as dashed lines.

A summary of SSM reactant molar ratios, isolated yields, surface areas, crystallite sizes, and bulk $Co_{1-x}Fe_xB$ chemical composition by ICP-OES analysis is shown in **Table 1**. Bulk elemental analysis shows that total metal (Co+Fe) versus B atomic ratios are close to expected ratios based on SSM production formation (MB+B or M:B = 33:67). There is lower than ideal excess boron in some cases, perhaps due to loss during the wash process if MgB_x side products were formed. The Co/Fe ratios of different $Co_{1-x}Fe_xB$ products closely agree with the SSM reactant Co/Fe ratios. XRF and EDS composition metals analysis of Co and Fe similarly show product metal ratios are close to the SSM reactant ratios (**Table S4**). Plots of ICP and EDS compositions versus unit cell volume resulted in similar linear correlations to those shown above for the ideal solid-solution concentrations (**Figure S3**).

Table 1. Characterization results for $Co_{1-x}Fe_xB$ formed from $CoCl_2/FeCl_2/Mg/B$ SSM reactions.

SSM reaction molar ratios	Ideal Product (% yield)	ICP (at%) Co/Fe/B/Mg $Co_{1-x}Fe_xB + B^1$	BET (m^2g^{-1})	Crystallite Size (nm)
$CoCl_2/Mg/2B$	CoB + B (85)	35/0/64/1 CoB + 0.83B	2	48
$0.8CoCl_2/0.2FeCl_2/Mg/2B$	$Co_{0.8}Fe_{0.2}B$ + B (81)	34/8/56/2 $Co_{0.81}Fe_{0.19}B$ + 0.33B	3	50
$0.6CoCl_2/0.4FeCl_2/Mg/2B$	$Co_{0.6}Fe_{0.4}B$ + B (81)	19/14/65/1 $Co_{0.58}Fe_{0.42}B$ + 0.91B	11	60
$0.5CoCl_2/0.5FeCl_2/Mg/2B$	$Co_{0.5}Fe_{0.5}B$ + B (80)	16/17/66/1 $Co_{0.48}Fe_{0.52}B$ + 1.0B	11	70
$0.4CoCl_2/0.6FeCl_2/Mg/2B$	$Co_{0.4}Fe_{0.6}B$ + B (83)	13/22/64/1 $Co_{0.37}Fe_{0.63}B$ + 0.83B	17	60
$0.2CoCl_2/0.8FeCl_2/Mg/2B$	$Co_{0.2}Fe_{0.8}B$ + B (86)	6/29/64/1 $Co_{0.17}Fe_{0.83}B$ + 0.83B	8	65
$FeCl_2/Mg/2B$	FeB + B (104)	0/37/63/0 FeB + 0.70B	9	65

1) product formulas calculated assuming monoboride (MB) formation with excess boron.

The distribution of Co, Fe, and B was examined using SEM-EDS elemental mapping and confirmed that a relatively uniform distribution of metals and boron exists in these $Co_{1-x}Fe_xB$ products (**Figure 5**). These EDS elemental maps qualitatively show a decrease in Co with increasing Fe as x increases in $Co_{1-x}Fe_xB$ products. There are regions where boron is abundant and the metal content is low, which could be excess amorphous boron present in these washed products.

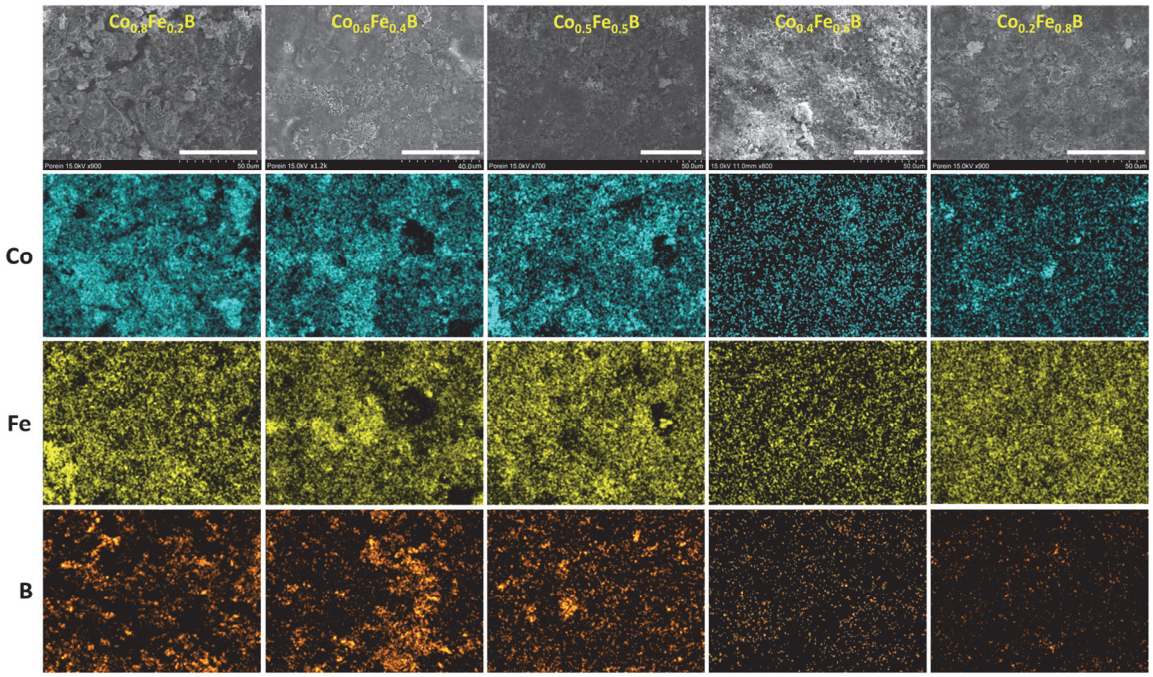

Figure 5. EDS elemental mapping images of $Co_{1-x}Fe_xB$ solid-solutions showing the transition from cobalt-rich to iron-rich products (left to right). The white scale bar in the SEM images is 40 µm for $Co_{0.6}Fe_{0.4}B$ and 50 µm for other solid-solutions.

SEM imaging was used to investigate the morphology and particle size distribution of the different metal borides from these rapid SSM reactions that theoretically reach temperatures near 1400 °C and grow from molten $MgCl_2$. As shown in **Figures 6**, **S4**, and **S5**, FeB and iron-rich borides are primarily composed of round and relatively smooth particles with some that have well-defined-edges, and these particles form large 5-50 µm aggregates. The CoB and cobalt-rich solid-solution products show large (~25-50 µm) monolithic blocky aggregates with some smaller (~3-5 µm) particles forming sheet-like aggregates (**Figures 6**, **S4**, and **S5**). While moving from Fe-rich to Co-rich appears to alter the larger particle morphologies from round particles to faceted blocks, all products have small particle sheet-like aggregates (**Figure S4**). These sheets often have holes in them that may be a consequence of metal boride growth in molten $MgCl_2$, and holes represent areas where $MgCl_2$ was removed during washing.

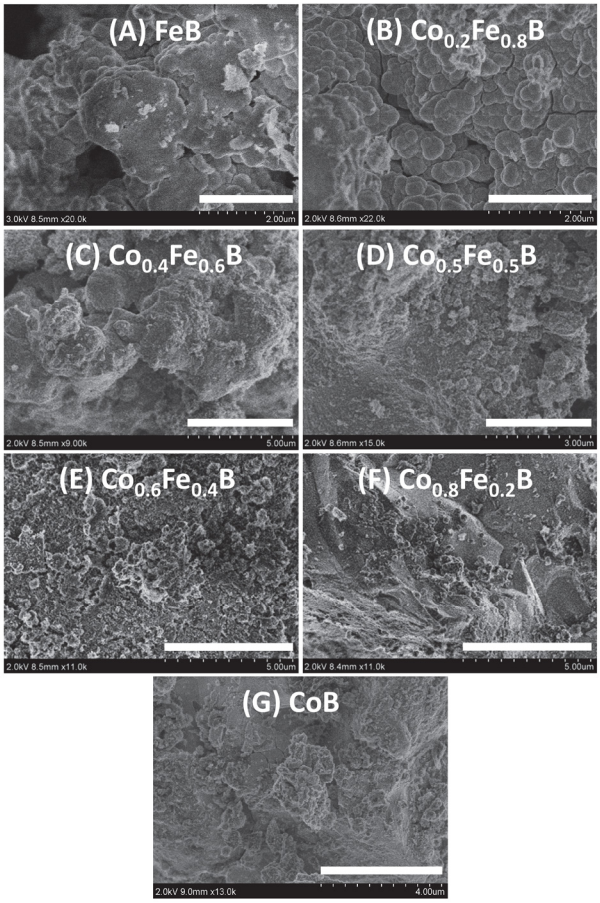

Figure 6. Comparison of SEM particle morphologies for CoB, FeB and $Co_{1-x}Fe_xB$ solid-solutions. Scale bar lengths are: (A) 2 µm, (B) 2 µm, (C) 5 µm, (D) 3 µm, (E) 5 µm, (F) 5 µm, (G) 4 µm.

The bulk gas adsorption BET surface areas for these SSM synthesized $Co_{1-x}Fe_xB$ are all relatively low (< 20 m^2/g) and consistent with the aggregated SEM images (**Table 1**). There appears to be a slight increase in surface area for the middle of the solid-solution series, with iron-rich samples showing relatively higher BET values. Since the amount of amorphous boron (BET SA = 12 m^2g^{-1}) is similar in these different products, it is likely that the observed differences are related to the aggregation of the boride particles.

As shown in **Table 1** (and **Table S5**), the metal boride XRD average crystallite sizes are in the range of ~50 to 70 nm, which is much smaller than the particulate sizes observed by SEM. TEM images from alcohol suspensions of smaller particles in several products show that FeB particles are nearly spherical with ~100 to 200 nm diameters, while CoB and other solid-solution particles are irregular agglomerated nanoparticles in the 100 nm range (**Figures S6** and **S7**). There is a wide range of aggregated particle sizes (~50-400 nm), as well as semi-transparent and irregular wrinkled layer-like regions that are similar to

amorphous boron (**Figure S7**). Excess boron in metal boride products is likely physically distributed throughout the sample.

Thermochemical exothermicity and temperature predictions for metal borides. Reaction thermochemistry plays a vital role in SSM reactions because the reaction enthalpy (ΔH_{rxn}) must be significantly large and negative for the reaction to efficiently self-propagate and self-heat. A thermochemical analysis of reaction intermediate steps can provide information on favored intermediates and predict an ideal maximum reaction temperature assuming adiabatic conditions (T_{ad}). The enthalpy values and predicted temperatures (ΔH_{rxn}, T_{ad}) for metal boride formation from MCl_2/Mg/2B were calculated using Hess's law and product heat capacities/phase changes, assuming complete reaction and that reaction enthalpy released is used to heat the products (MB, B, and $MgCl_2$). Thermochemical values for $Co_{1-x}Fe_xB$ solid-solutions were estimated using end member data in ratios of (1-x) CoB and x FeB. A sample ΔH_{rxn} graph and T_{ad} calculation are shown in **Figure S8** (and associated text). All $Co_{1-x}Fe_xB$ formation reactions are predicted to reach the $MgCl_2$ boiling point (1412 °C) and have sufficient additional enthalpy to evaporate much of the $MgCl_2$ salt (**Table 2**).[73-76]

Stable $MgCl_2$ formation (ΔH_f = -644 kJ/mol) drives highly exothermic and self-sustaining metal boride SSM reactions. The byproduct $MgCl_2$ salt (mp/bp = 707/1412 °C) undergoes two energy absorbing melting and boiling phase transitions that moderate reaction temperatures. A majority of the released enthalpy is absorbed during $MgCl_2$ melting and vaporization (**Figure S8**). The molten $MgCl_2$ salt also functions as a short-lived flux that can assist in metal boride growth by providing a medium for facile diffusion of reactants to form small boride particles that can aggregate and are later encased in a solidified salt matrix.

Table 2. Thermochemical data on the formation of $Co_{1-x}Fe_xB$ solid solutions from $CoCl_2$/$FeCl_2$/Mg/B reactions.

Reaction	Targeted Product	ΔH_{rxn} (kJ mol^{-1} MB)	T_{ad} (°C)	% $MgCl_2$ vaporized
$CoCl_2$+Mg+2B	CoB + B + $MgCl_2$	-425.8	1412	100
0.8$CoCl_2$+0.2$FeCl_2$+Mg+2B	$Co_{0.8}Fe_{0.2}B$ + B + $MgCl_2$	-415.7	1412	94
0.6$CoCl_2$+0.4$FeCl_2$+Mg+2B	$Co_{0.6}Fe_{0.4}B$ + B + $MgCl_2$	-405.6	1412	89
0.5$CoCl_2$+0.5$FeCl_2$+Mg+2B	$Co_{0.5}Fe_{0.5}B$ + B + $MgCl_2$	-400.6	1412	86
0.4$CoCl_2$+0.6$FeCl_2$+Mg+2B	$Co_{0.4}Fe_{0.6}B$ + B + $MgCl_2$	-395.6	1412	83
0.2$CoCl_2$+0.8$FeCl_2$+Mg+2B	$Co_{0.2}Fe_{0.8}B$ + B + $MgCl_2$	-385.5	1412	77
$FeCl_2$+Mg+2B	FeB + B + $MgCl_2$	-375.4	1412	72

Evaluation of metal boride SSM reaction intermediates. Previous SSM studies have proposed that SSM reactions progress through the formation of transient elemental intermediates via ionic exchange reactions.[47, 48] SSM reactions appear to progress through at least two formation energy barriers, the first being byproduct salt formation (E_{a1}), followed by product formation (E_{a2}).[48, 61] The rapid self-propagation nature of SSM reactions makes a direct study of reaction mechanisms and reaction intermediates challenging.[48, 52] We previously demonstrated in FeB, CoB, and NiB formation from rapid SSM reactions that the salt byproduct formation reaction ($MCl_2+Mg \rightarrow M+MgCl_2$) is sufficient to overcome the E_{a1} activation barrier, whereas the product formation ($M+B \rightarrow MB$) requires high temperature heating to proceed.[62] In the Co-Fe-B mixed metal boride reactions, three intermediate metal salt reduction reactions were examined (**Equation 2**). All these three reduction reactions are highly exothermic (>300 kJ/mol) (**Table S6**).

$$(1\text{-}x)CoCl_2(s) + xFeCl_2(s) + Mg(s) \rightarrow \mathbf{Co_{1-x}Fe_x(s)} + MgCl_2(s) \quad (2)$$
$$(x = 0.2, 0.5, 0.8)$$

Hot filament SSM reactions were successfully initiated and self-propagated to form elemental Co and Fe, though some XRD peak shifts and peak shoulders indicate that some metal mixing occurs in the products (**Figure S9**). XRD shows no Co peak in the 20% Co reaction, but EDS elemental mapping and semi-quantitative elemental analysis confirm the presence of Co near the targeted ratio (**Figure S10**). SEM analysis shows that an 80% Co sample consists of monolithic blocks (20-200 μm) and aggregates of small nanometer-sized particles, while Fe-rich particle morphologies are mainly aggregated particles (5-50 μm) (**Figure S11**). These results support the idea that exothermic metal reduction and salt formation are thermochemically favored as initial steps in these rapid SSM reactions.

Examination of electrocatalytic water splitting with Co-Fe-B mixed metal borides

Hydrogen evolution reaction (HER) electrocatalysis with metal borides. Several metal borides have been examined as HER electrocatalysts, but many prior studies use products that are nanostructured, supported, or poorly crystalline or amorphous (see **Table S7** for literature summary of HER electrocatalysis using Fe/Co borides and other element crystalline borides). Some Co-Fe-B mixed-metal boride nanoparticles show enhanced HER activity versus either CoB or FeB that are described as synergistic effects of both Co and Fe in the structure and on the surface.[11] We examined the HER activities of crystalline $Co_{1-x}Fe_xB$ from SSM reactions in H_2 saturated 1.0 M KOH and compared their activities to the FeB and CoB end members. Representative linear sweep voltammetry (LSV) plots show that the HER activity of SSM synthesized CoB and FeB is comparable to our previous report showing that these crystalline 3d metal borides are HER active (**Figure 7**).[62] The crystalline CoB powder exhibits similar

electrocatalytic activity to other reported crystalline and amorphous cobalt borides (**Table S7**). There is no HER activity from amorphous boron alone, which is useful to see as each metal boride product contains ~50 mol% boron based on reaction balance and elemental analysis.

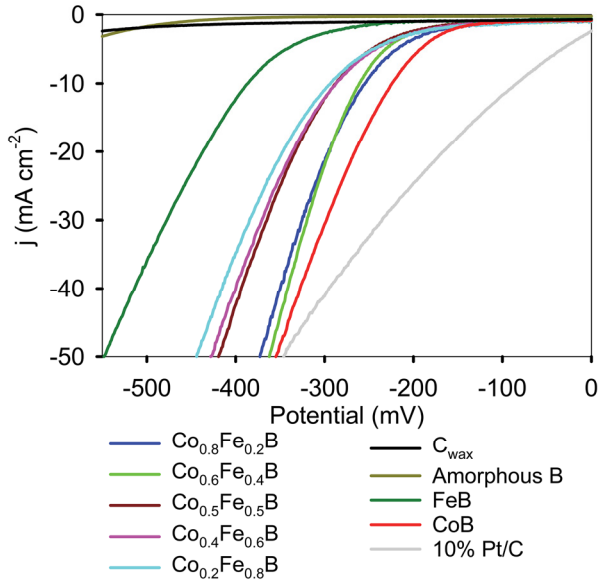

Figure 7. Representative HER LSV results of CoB, FeB, and $Co_{1-x}Fe_xB$ solid-solutions. Plots for the C_{wax} and amorphous B are shown for comparison. Data was obtained using 1.0 M KOH in a three-electrode cell at 5 mV/s scan rate with Hg/HgO reference and graphite rod counter electrodes. Current densities are scaled using the geometric electrode area (0.08 cm^2).

The HER activities of $Co_{1-x}Fe_xB$ materials show a systematic trend of increasing HER activity at lower applied potentials as more cobalt is substituted into FeB, with groupings of Co-rich (60-80% Co) and Co-poor samples (20-50% Co) (**Figures 7** and **S12**). The crystalline $Co_{1-x}Fe_xB$ materials show comparable HER activity to previously reported crystalline or amorphous ternary metal borides containing Co and/or Fe (**Table S8**). The overall HER activity to achieve 10 mA cm^{-2} (η_{10}) current density is ordered as FeB < $Co_{0.2}Fe_{0.8}B$ ~ $Co_{0.4}Fe_{0.6}B$ ~ $Co_{0.5}Fe_{0.5}B$ < $Co_{0.6}Fe_{0.4}B$ ~ $Co_{0.8}Fe_{0.2}B$ < CoB with applied potentials ranging from -223 mV to -395 mV. The average HER activities over multiple LSV scans are summarized in **Table 3**. At high current densities, the HER activity of the highest cobalt content $Co_{1-x}Fe_xB$ solid solutions are comparable to the benchmark 10% Pt/C. Graphical representations of applied potentials for several current densities (10, 20, 50 mA cm^{-2}) as a function of run number are shown in **Figure S13**. The LSV data shown in **Figure 7** is not *iR* compensated as this may obscure differences in catalyst activity due to surface charge transfer interactions.[77, 78] LSV overlay results for 85% *iR* compensated data are shown in **Figure S14** and

reported in **Table 3**, with ~10-15 mV lower applied potentials to achieve 10 mA cm^{-2} current densities versus uncompensated results. The electrochemical surface area (ECSA) trend for these metal borides is similar to physical BET surface areas (**Table 1**) with the solid solutions having higher ECSA than CoB. The geometric electrode area normalized LSV and the ECSA normalized data for $Co_{1-x}Fe_xB$ show the same trend of increasing HER activity as Fe is replaced by Co (**Figure S15**).

Table 3. Summary of HER electrocatalysis using SSM synthesized Co-Fe-B metal borides.

Sample	(η_{10}) (mV)[1]	(η_{20}) (mV)[1]	Tafel (mV/dec)	ECSA (cm^2)
CoB	-223 ± 4 (-211 ± 4)	-265 ± 4 (-240 ± 4)	-105 (-90)	22
$Co_{0.8}Fe_{0.2}B$	-262 ± 10 (-249 ± 10)	-304 ± 11 (-278 ± 10)	-136 (-103)	31
$Co_{0.6}Fe_{0.4}B$	-260 ± 6 (-250 ± 7)	-294 ± 6 (-274 ± 6)	-103 (-82)	52
$Co_{0.5}Fe_{0.5}B$	-289 ± 10 (-274 ± 10)	-333 ± 11 (-303 ± 11)	-150 (-117)	49
$Co_{0.4}Fe_{0.6}B$	-289 ± 11 (-275 ± 11)	-338 ± 11 (-310 ± 11)	-160 (-131)	56
$Co_{0.2}Fe_{0.8}B$	-297 ± 4 (-286 ± 4)	-350 ± 3 (-327 ± 3)	-177 (-150)	52
FeB	-395 ± 3 (-382 ± 3)	-444 ± 3 (-418 ± 3)	-136 (-120)	43
B	n/a	n/a	-	3
10% Pt/C	-83 ±24 (-62 ± 24)	-163 ± 34 (-120 ± 34)	-89 (-83)	34

1) applied potentials reported versus RHE in 1.0 M KOH and current densities normalized to geometric electrode area of 0.08 cm^2 (85% manual *iR* compensation results in parentheses). Deviations are for 50 LSV runs with no iR compensation and with 85% manual *iR* compensation. n/a means not achieved.

These HER electrocatalysis results for crystalline $Co_{1-x}Fe_xB$ solid-solutions demonstrate that Co-Fe mixing leads to a trend that more closely follows a compositional linear trend rather than a synergistic enhancement effect of both Fe and Co metals in the solid-solution boride. After normalizing for differences in surface area and resistance, our HER results in acidic electrolyte indicates that the cobalt content of the $Co_{1-x}Fe_xB$ solid solution catalyst particles is the more relevant determining factor for increased HER activity at lower applied potentials. To investigate the effect of Co-Fe mixing on electrocatalytic activity, physical mixtures of CoB and FeB were made that mirror the chemical compositions of the $Co_{1-x}Fe_xB$ solid solutions. The HER electrocatalytic activities of these physically mixed (1-x)CoB/xFeB materials were between the FeB and CoB activities and they had lower ECSA values than the chemically mixed $Co_{1-x}Fe_xB$ materials (**Table S9** and **Figure S16**). In the solid-solution and physical mixture experiments, CoB is more active despite its lower ECSA or surface area, suggesting that a major factor in HER activity is the cobalt content.

The initial LSV (Tafel) slopes can provide insight on the H_2 formation process that occurs on the catalyst surface. Three HER reactions at low coverage are a Volmer step – proton adsorption-reduction (120 mV dec^{-1}), a Heyrovsky step – hydride/proton interaction with reduction and H_2 desorption (40 mV dec^{-1}), and a Tafel step – hydride migration and H_2 desorption (30 mV dec^{-1}) in water and hydronium-ion reduction reactions.[79] At higher proton surface coverage, the Heyrovsky step may reach 120 mV dec^{-1}. The metal borides examined here have Tafel slopes around or above 120 mV dec^{-1} (105 to 177 mV dec^{-1}), indicating that initial proton adsorption and reduction processes on the boride surfaces may be rate limiting (**Table 3** and **Figure S17**). The lowest Tafel slope is found for the most active CoB material and so initial proton adsorption to surface cobalt sites is likely a key reaction step in basic electrolyte. These solid-solution metal boride HER electrocatalysis results provide useful comparative data for theoretical studies on the energetics of surface hydrogen evolution reactions.

The extended electrocatalytic HER stability of $Co_{1-x}Fe_xB$ materials was examined in 1.0 M KOH at a constant potential to maintain ~10 mA cm^{-2} current density for a 24-hour period. These chronoamperometry (CA) studies show that the cobalt-rich $Co_{1-x}Fe_xB$ solid solutions show relatively constant activity similar to CoB (**Figure S18**). The iron-rich $Co_{1-x}Fe_xB$ and FeB show a small increase in activity over the 24-hour period that is also evident in LSVs taken after the CA experiments (**Table S10**). SEM particle morphologies of FeB after CA experiments show smoother particles with fewer edges than prior to electrochemistry (**Figure S19**), indicating that some surface chemical and physical changes occur on iron-rich boride surfaces. The bulk crystallinity of the post-CA samples on electrode tips was examined by XRD and all $Co_{1-x}Fe_xB$ samples showed key XRD peaks for their original metal boride structures, indicating the bulk structure survives extended HER reactions in 1 M KOH (**Figure S20**). EDS elemental maps of metal borides on C_{wax} electrodes after extended HER electrochemistry experiments show that metal and boron are still present and distributed uniformly on the electrode surface (**Figures S21** and **S22**). While it is difficult to get quantitative compositional data from the small amount of metal boride on these electrode tip samples, EDS analysis suggests that some samples may lose cobalt relative to iron after extended 24-hour cycling (**Table S11**), even when bulk XRD structures remain intact.

OER electrocatalysis using metal borides. The literature evidence suggests that Fe is important in Co-Fe-solid solution OER electrocatalysts, but the precise function of Fe is not well understood. Post-electrochemistry XPS results confirm that Fe compounds readily form OOH-like species that may increase the catalytic activity of Co_x-Fe-B.[65] Active surface oxygen species thought to play an important role in OER catalysis include Co(O)OH, Fe(O)OH, and FeCo(O)OH.[11, 65, 66] The OER activities of crystalline Co_{1-}

$_x$Fe$_x$B solid-solutions were examined in this study to investigate the influence of Fe mixing with Co in borides on OER electrocatalytic activity as compared to activities of the CoB and FeB end members. Representative metal boride LSVs are shown in **Figure 8** and illustrate CoB and Co-rich $Co_{1-x}Fe_xB$ solid-solutions possess higher OER activity as compared to FeB and Fe-rich $Co_{0.2}Fe_{0.8}B$ samples (**Figure S23**). Very similar OER activity is seen for CoB and $Co_{1-x}Fe_xB$ solid-solutions up to ~ 40 at% Co with only a ~14 mV potential difference at 10 mA/cm^2 current density.

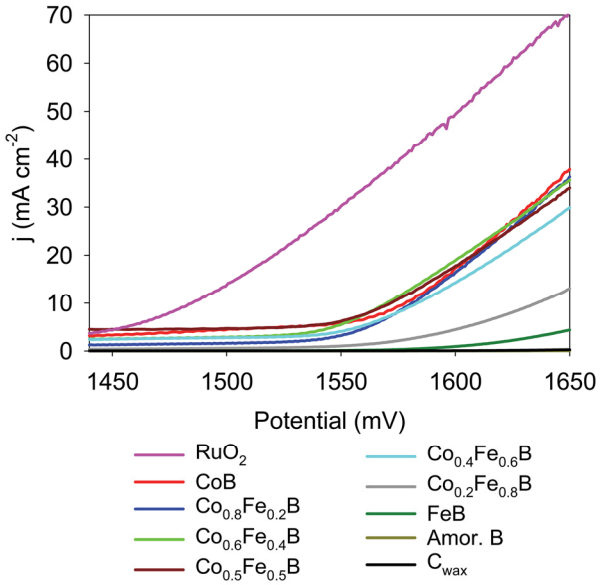

Figure 8. Representative OER LSV results of CoB, FeB, and $Co_{1-x}Fe_xB$ solid-solutions. Plots for the C_{wax} and boron are shown for comparison. Data was obtained in O_2 purged 1.0 M KOH in a three-electrode cell at 5 mV s^{-1} scan rate with Hg/HgO reference and graphite rod counter electrodes. Current densities are scaled using the geometric electrode area (0.08 cm^2). Amorphous boron and C_{wax} data are at baseline levels.

Initial LSV scans for several samples show Co^{2+} to Co^{3+}oxidation peaks, likely creating CoOOH surface species.[80] Six LSVs were performed as conditioning runs to achieve reproducible, overlapping LSVs (**Figure S24**). This Co^{2+} oxidation peak shifts to higher potentials with Fe incorporation and decreases in magnitude (**Figure S25**), which could indicate some redox interactions between Co and Fe in $Co_{1-x}Fe_xB$.[65] The average applied potentials to achieve 10 and 20 mA/cm^{-2} current densities are reported in **Table 4** and show similar OER activities for CoB and the $Co_{1-x}Fe_xB$ solid solutions with $x \geq 0.4$ with relatively stable OER over multiple LSV runs with and without *iR* compensation (**Figures S26** and **S27**). Based on the LSVs results, there is no evidence for a synergistic Fe-Co enhancement of OER activity with these crystalline solid solutions versus a more systematic trend of higher Co content leading to higher OER

activity. As shown in Figure 8, once the solid-solution material reaches ~50 mol% Co content, the OER activity is similar to the activity of the CoB end member.

Table 4. Summary of OER electrocatalysis of SSM synthesized metal borides.

Sample	Applied potential @ 10 mA cm^{-2} (mV)[1]	Applied potential @ 20 mA cm^{-2} (mV)[1]	Tafel (mV dec^{-1})
CoB	1575 ± 12 (1562 ± 12)	1608 ± 1 (1581 ± 1)	95 (55)
$Co_{0.8}Fe_{0.2}B$	1581 ± 5 (1568 ± 5)	1609 ± 6 (1583 ± 6)	66 (44)
$Co_{0.6}Fe_{0.4}B$	1570 ± 2 (1553 ± 2)	1603 ± 3 (1569 ± 3)	79 (49)
$Co_{0.5}Fe_{0.5}B$	1568 ± 17 (1553 ± 17)	1607 ± 6 (1578 ± 6)	103 (68)
$Co_{0.4}Fe_{0.6}B$	1583 ± 7 (1568 ± 7)	1618 ± 9 (1590 ± 9)	87 (63)
$Co_{0.2}Fe_{0.8}B$	1633 ± 10 (1616 ± 10)	1675 ± 13 (1640 ± 13)	78 (67)
FeB	1686 ± 4 (1673 ± 4)	1735 ± 6 (1707 ± 6)	52 (51)
RuO_2	1484 ± 3 (1469 ± 3)	1520 ± 3 (1489 ± 3)	99 (68)
B	n/a	n/a	3

1) Applied potentials reported versus RHE in 1.0 M KOH and current densities normalized to geometric electrode area of 0.08 cm^2 (85% manually calculated *iR* compensation results in parentheses). Deviations are for 50 LSV runs with and without *iR* compensation, after 6 conditioning runs. n/a means current density not achieved.

The extended 24-hour OER activities of CoB, FeB, and $Co_{1-x}Fe_xB$ solid-solutions were examined in 1.0 M KOH using CA experiments with a set potential to maintain ~10 mA cm^{-2} current density. While the cobalt-containing metal borides display very good overall extended OER stability, the less active FeB exhibits some improved OER electrocatalytic activity over time (**Figure S28** and **Table S12**). The post-CA analysis of catalyst particles on electrode tips shows that the bulk crystallinity of the metal borides is retained after extended oxidizing electrocatalysis (**Figure S20**). EDS elemental maps show that a relatively uniform distribution of metal and B on the catalyst surface remains after extended CA experiments, with higher surface oxygen as expected (**Figure S29**). The Co/Fe metal ratio of $Co_{1-x}Fe_xB$ solid-solutions is similar to those of the starting boride catalyst, indicating these boride solid solution materials are fairly robust even if some surface oxyhydroxide formation occurs (**Table S11**).

Conclusions

In this study, we demonstrated that the solvent-free, rapid and exothermic SSM reactions produce crystalline $Co_{1-x}Fe_xB$ solid-solution metal borides with compositions that reflect the stoichiometric ratios of $CoCl_2$, $FeCl_2$, Mg, and B reactants. This work highlights the successful atomic level mixing and reaction of four reactants in a hot filament initiated rapid (few seconds) SSM reactions leading to metal boride crystal growth in molten $MgCl_2$ where reaction temperatures may transiently reach ~1400 °C. This four-component SSM reaction successfully produced crystalline $Co_{1-x}Fe_xB$ compositions with a wide range of x values (x = 0, 0.2, 0.4, 0.5, 0.6, 0.8, 1). The changes in unit cell parameters follow a nearly linear relationship with compositional changes in $Co_{1-x}Fe_xB$. An examination of reaction intermediates indicates that exothermic MCl_2/Mg reduction reactions form metal alloys that can react with amorphous boron in the molten salt. The HER and OER activities of this series of mixed metal borides were examined in 1.0 M KOH and both show higher activity for the more cobalt-rich phases. The cobalt containing borides showed very good extended electrocatalytic stability and bulk crystallinity of $Co_{1-x}Fe_xB$ on carbon wax electrodes is retained after electrocatalysis. The observed HER activity trend correlates well with cobalt composition, indicating that these crystalline microparticulate metal boride catalysts show a systematic rather than synergistic impact of iron additions to CoB. This work also provides new support for the utility of a magnesium reduction strategy for rapid SSM reactions that allows facile tuning of reaction products and mixed metal boride structures.

Author Contributions. Corresponding author (Edward G. Gillan, edward-gillan@uiowa.edu). The authors declare no competing financial interest. JA performed all metal boride SSM experiments, conducted all product analyses, and ran all the electrochemical experiments. JA and EG both contributed to experimental designs, manuscript preparation, and the creation of graphical and tabular content.

Conflicts of Interest. There are no conflicts to declare.

Acknowledgments. The authors thank Matthew Lovander for assistance with electrochemical data analysis and initial graphite wax electrode designs. This material is based upon work supported by the National Science Foundation under Grant No. 1954676.

Supporting Information. Unit cell parameters of metal borides, 2θ (d-spacing) values of crystal planes, ICP and EDS Co/Fe ratios, EDS maps of metal borides before and after electrochemistry measurements, additional product SEM and TEM images, thermochemical reaction calculations and graphs for CoB, FeB

and $Co_{0.5}Fe_{0.5}B$, mechanistic study results of SSM reactions, graphical and tabular results for electrocatalytic HER and OER studies, *iR* compensated HER and OER overlay graphs, chronoamperometric measurements, tables of literature comparison data, and XRD data on borides on C_{wax} tips after 24-hour electrocatalysis after HER and OER.

References

(1) Sharma, S.; Ghoshal, S. K. Hydrogen the future transportation fuel: From production to applications. *Renew. Sustain. Energy Rev.* **2015**, *43*, 1151-1158. DOI: 10.1016/j.rser.2014.11.093.
(2) van den Berg, A. W. C.; Arean, C. O. Materials for hydrogen storage: current research trends and perspectives. *Chem. Commun.* **2008**, (6), 668-681. DOI: 10.1039/b712576n.
(3) Coleman, N., Jr.; Lovander, M. D.; Leddy, J.; Gillan, E. G. Phosphorus-Rich Metal Phosphides: Direct and Tin Flux-Assisted Synthesis and Evaluation as Hydrogen Evolution Electrocatalysts. *Inorg. Chem.* **2019**, *58* (8), 5013-5024. DOI: 10.1021/acs.inorgchem.9b00032.
(4) Xu, J.; Li, J.; Xiong, D.; Zhang, B.; Liu, Y.; Wu, K.-H.; Amorim, I.; Li, W.; Liu, L. Trends in activity for the oxygen evolution reaction on transition metal (M = Fe, Co, Ni) phosphide pre-catalysts. *Chem. Sci.* **2018**, *9* (14), 3470-3476. DOI: 10.1039/c7sc05033j.
(5) Burke, M. S.; Kast, M. G.; Trotochaud, L.; Smith, A. M.; Boettcher, S. W. Cobalt−Iron (Oxy)hydroxide Oxygen Evolution Electrocatalysts: The Role of Structure and Composition on Activity, Stability, and Mechanism. *J. Am. Chem. Soc.* **2015**, *137* (10), 3638-3648. DOI: 10.1021/jacs.5b00281.
(6) Guo, D.; Kang, H.; Wei, P.; Yang, Y.; Hao, Z.; Zhang, Q.; Liu, L. A high-performance bimetallic cobalt iron oxide catalyst for the oxygen evolution reaction. *CrystEngComm* **2020**, *22* (25), 4317-4323. DOI: 10.1039/d0ce00401d.
(7) Huang, S.-Y.; Sodano, D.; Leonard, T.; Luiso, S.; Fedkiw, P. S. Cobalt-Doped Iron Sulfide as an Electrocatalyst for Hydrogen Evolution. *J. Electrochem. Soc.* **2017**, *164* (4), F276-F282. DOI: 10.1149/2.0761704jes.
(8) Zhou, Y.; Luo, M.; Zhang, Z.; Li, W.; Shen, X.; Xia, W.; Zhou, M.; Zeng, X. Iron doped cobalt sulfide derived boosted electrocatalyst for water oxidation. *Appl. Surf. Sci.* **2018**, *448*, 9-15. DOI: 10.1016/j.apsusc.2018.04.080.
(9) Li, D.; Xing, Y.; Yang, R.; Wen, T.; Jiang, D.; Shi, W.; Yuan, S. Holey Cobalt-Iron Nitride Nanosheet Arrays as High-Performance Bifunctional Electrocatalysts for Overall Water Splitting. *ACS Appl. Mater. Interfaces* **2020**, *12* (26), 29253-29263. DOI: 10.1021/acsami.0c05219.
(10) Wang, Y.; Liu, D.; Liu, Z.; Xie, C.; Huo, J.; Wang, S. Porous cobalt-iron nitride nanowires as excellent bifunctional electrocatalysts for overall water splitting. *Chem. Commun.* **2016**, *52* (85), 12614-12617. DOI: 10.1039/c6cc06608a.
(11) Qiang, C.; Zhang, L.; He, H.; Liu, Y.; Zhao, Y.; Sheng, T.; Liu, S.; Wu, X.; Fang, Z. Efficient electrocatalytic water splitting by bimetallic cobalt iron boride nanoparticles with controlled electronic structure. *J. Colloid Interface Sci.* **2021**, *604*, 650-659. DOI: 10.1016/j.jcis.2021.07.024.
(12) Li, Y.; Huang, B.; Sun, Y.; Luo, M.; Yang, Y.; Qin, Y.; Wang, L.; Li, C.; Lv, F.; Zhang, W.; et al. Multimetal Borides Nanochains as Efficient Electrocatalysts for Overall Water Splitting. *Small* **2019**, *15*, 1804212. DOI: 10.1002/smll.201804212.
(13) Weimer, A. W. *Carbide, Nitride and Boride Materials Synthesis and Processing*; Chapman and Hall, 1997.
(14) Gu, Q.; Krauss, G.; Steurer, W. Transition Metal Borides: Superhard versus Ultra-incompressible. *Adv. Mater.* **2008**, *20* (19), 3620-3626. DOI: 10.1002/adma.200703025.
(15) Fokwa, B. P. T. Borides: Solid-State Chemistry. In *Encyclopedia of Inorganic and Bioinorganic Chemistry*, Wiley, 2014; pp 1-14. DOI: 10.1002/9781119951438.eibc0022.pub2.

(16) Wang, P.; Kumar, R.; Sankaran, E. M.; Qi, X.; Zhang, X.; Popov, D.; Cornelius, A. L.; Li, B.; Zhao, Y.; Wang, L. Vanadium Diboride (VB_2) Synthesized at High Pressure: Elastic, Mechanical, Electronic, and Magnetic Properties and Thermal Stability. *Inorg. Chem.* **2018**, *57* (3), 1096-1105. DOI: 10.1021/acs.inorgchem.7b02550.
(17) Demirskyi, D.; Solodkyi, I.; Nishimura, T.; Sakka, Y.; Vasylkiv, O. High-temperature strength and plastic deformation behavior of niobium diboride consolidated by spark plasma sintering. *J. Am. Ceram. Soc.* **2017**, *100* (11), 5295-5305. DOI: 10.1111/jace.15048.
(18) Cumberland, R. W.; Weinberger, M. B.; Gilman, J. J.; Clark, S. M.; Tolbert, S. H.; Kaner, R. B. Osmium Diboride, an Ultra-Incompressible, Hard Material. *J. Am. Chem. Soc.* **2005**, *127* (20), 7264-7265. DOI: 10.1021/ja043806y.
(19) Aronsson, B.; Lundström, T.; Rundqvist, S. *BORIDES, SILICIDES AND PHOSPHIDES*; John Wiley & Sons Inc, 1965.
(20) Chung, H.-Y.; Weinberger, M. B.; Levine, J. B.; Kavner, A.; Yang, J.-M.; Tolbert, S. H.; Kaner, R. B. Synthesis of Ultra-Incompressible Superhard Rhenium Diboride at Ambient Pressure. *Science* **2007**, *316* (5823), 436-439. DOI: 10.1126/science.1139322.
(21) Campos-Silva, I. E.; Rodríguez-Castro, G. A. Boriding to improve the mechanical properties and corrosion resistance of steels. In *Thermochemical Surface Engineering of Steels*, Mittemeijer, E. J., Somers, M. A. J. Eds.; Woodhead Publishing, 2015; pp 651-702.
(22) Hao, W.; Wu, R.; Zhang, R.; Ha, Y.; Chen, Z.; Wang, L.; Yang, Y.; Ma, X.; Sun, D.; Fang, F.; et al. Electroless Plating of Highly Efficient Bifunctional Boride-Based Electrodes toward Practical Overall Water Splitting. *Adv. Energy Mater.* **2018**, *8* (26), 1801372. DOI: 10.1002/aenm.201801372.
(23) Zeng, M.; Wang, H.; Zhao, C.; Wei, J.; Qi, K.; Wang, W.; Bai, X. Nanostructured Amorphous Nickel Boride for High-Efficiency Electrocatalytic Hydrogen Evolution over a Broad pH Range. *ChemCatChem* **2016**, *8* (4), 708-712. DOI: 10.1002/cctc.201501221.
(24) Jothi, P. R.; Zhang, Y.; Scheifers, J. P.; Park, H.; Fokwa, B. P. T. Molybdenum diboride nanoparticles as a highly efficient electrocatalyst for the hydrogen evolution reaction. *Sustainable Energy Fuels* **2017**, *1*, 1928-1934. DOI: 10.1039/c7se00397h.
(25) Jothi, P. R.; Zhang, Y.; Yubuta, K.; Culver, D. B.; Conley, M.; Fokwa, B. P. T. Abundant Vanadium Diboride with Graphene-like Boron layers for Hydrogen Evolution. *ACS Appl. Energy Mater.* **2019**, *2* (1), 176-181. DOI: 10.1021/acsaem.8b01615.
(26) Guo, F.; Wu, Y.; Ai, X.; Chen, H.; Li, G.-D.; Chen, W.; Zou, X. A class of metal diboride electrocatalysts synthesized by a molten salt-assisted reaction for the hydrogen evolution reaction. *Chem. Commun.* **2019**, *55* (59), 8627-8630. DOI: 10.1039/c9cc03638e.
(27) Yao, Y.; Zhang, Z.; Jiao, L. Development Strategies in Transition Metal Borides for Electrochemical Water Splitting. *Energy Environ. Mater.* **2022**, *5* (2), 470-485. DOI: 10.1002/eem2.12198.
(28) Pu, Z.; Liu, T.; Zhang, G.; Liu, X.; Gauthier, M. A.; Chen, Z.; Sun, S. Nanostructured Metal Borides for Energy-Related Electrocatalysis: Recent Progress, Challenges, and Perspectives. *Small Methods* **2021**, *5* (10), 2100699. DOI: 10.1002/smtd.202100699.
(29) Gupta, S.; Patel, M. K.; Miotello, A.; Patel, N. Metal Boride-Based Catalysts for Electrochemical Water-Splitting: A Review. *Adv. Funct. Mater.* **2020**, *30* (1), 1906481. DOI: 10.1002/adfm.201906481.
(30) Jiang, Y.; Lu, Y. Designing transition-metal-boride-based electrocatalysts for applications in electrochemical water splitting. *Nanoscale* **2020**, *12* (17), 9327-9351. DOI: 10.1039/d0nr01279c.
(31) Chen, Z.; Duan, X.; Wei, W.; Wang, S.; Zhang, Z.; Ni, B.-J. Boride-based electrocatalysts: Emerging candidates for water splitting. *Nano Res.* **2020**, *13* (2), 293-314. DOI: 10.1007/s12274-020-2618-y.
(32) Chen, H.; Zou, X. Intermetallic borides: structures, synthesis and applications in electrocatalysis. *Inorg. Chem. Front.* **2020**, *7* (11), 2248-2264. DOI: 10.1039/d0qi00146e.
(33) Park, H.; Zhang, Y.; Lee, E.; Shankhari, P.; Fokwa, B. P. T. High-Current-Density HER Electrocatalysts: Graphene-like Boron Layer and Tungsten as Key Ingredients in Metal Diborides. *ChemSusChem* **2019**, *12* (16), 3726-3731. DOI: 10.1002/cssc.201901301.

(34) Mann, D. K.; Xu, J.; Mordvinova, N. E.; Yannello, V.; Ziouani, Y.; Gonzalez-Ballesteros, N.; Sousa, J. P. S.; Lebedev, O. I.; Kolen'ko, Y. V.; Shatruk, M. Electrocatalytic water oxidation over $AlFe_2B_2$. *Chem. Sci.* **2019**, *10* (9), 2796-2804. DOI: 10.1039/c8sc04106g.
(35) Sitler, S. J.; Raja, K. S.; Charit, I. Metal-Rich Transition Metal Diborides as Electrocatalysts for Hydrogen Evolution Reactions in a Wide Range of pH. *J. Electrochem. Soc.* **2016**, *163* (13), H1069-H1075. DOI: 10.1149/2.0201613jes.
(36) Sheng, M.; Wu, Q.; Wang, Y.; Liao, F.; Zhou, Q.; Hou, J.; Weng, W. Network-like porous Co-Ni-B grown on carbon cloth as efficient and stable catalytic electrodes for hydrogen evolution. *Electrochem. Commun.* **2018**, *93*, 104-108. DOI: 10.1016/j.elecom.2018.06.017.
(37) Gupta, S.; Patel, N.; Fernandes, R.; Kadrekar, R.; Dashora, A.; Yadav, A. K.; Bhattacharyya, D.; Jha, S. N.; Miotello, A.; Kothari, D. C. Co–Ni–B nanocatalyst for efficient hydrogen evolution reaction in wide pH range. *Appl. Catal. B* **2016**, *192*, 126-133. DOI: 10.1016/j.apcatb.2016.03.032.
(38) Klemenz, S.; Schuch, J.; Hawel, S.; Zieschang, A. M.; Kaiser, B.; Jaegermann, W.; Albert, B. Synthesis of a Highly Efficient Oxygen-Evolution Electrocatalyst by Incorporation of Iron into Nanoscale Cobalt Borides. *ChemSusChem* **2018**, *11* (18), 3150-3156. DOI: 10.1002/cssc.201801547.
(39) Ma, X.; Wen, J.; Zhang, S.; Yuan, H.; Li, K.; Yan, F.; Zhang, X.; Chen, Y. Crystal Co_xB (x = 1-3) Synthesized by a Ball-Milling Method as High-Performance Electrocatalysts for the Oxygen Evolution Reaction. *ACS Sustainable Chem. Eng.* **2017**, *5* (11), 10266-10274. DOI: 10.1021/acssuschemeng.7b02281.
(40) Alameda, L. T.; Holder, C. F.; Fenton, J. L.; Schaak, R. E. Partial Etching of Al from MoAlB Single Crystals To Expose Catalytically Active Basal Planes for the Hydrogen Evolution Reaction. *Chem. Mater.* **2017**, *29* (21), 8953-8957. DOI: 10.1021/acs.chemmater.7b02511.
(41) Jothi, P. R.; Yubuta, K.; Fokwa, B. P. T. A Simple, General Synthetic Route toward Nanoscale Transition Metal Borides. *Adv. Mater.* **2018**, *30* (14), 1704181. DOI: 10.1002/adma.201704181.
(42) Sun, Z.; Hao, S.; Ji, X.; Zheng, X.; Xie, J.; Li, X.; Tang, B. Efficient alkaline hydrogen evolution electrocatalysis enabled by an amorphous Co-Mo-B film. *Dalton Trans.* **2018**, *47* (23), 7640-7643. DOI: 10.1039/c8dt01296b.
(43) Wang, S.; He, P.; Xie, Z.; Jia, L.; He, M.; Zhang, X.; Dong, F.; Liu, H.; Zhang, Y.; Li, C. Tunable nanocotton-like amorphous ternary Ni-Co-B: A highly efficient catalyst for enhanced oxygen evolution reaction. *Electrochim. Acta* **2019**, *296*, 644-652. DOI: 10.1016/j.electacta.2018.11.099.
(44) Gouget, G.; Beaunier, P.; Portehault, D.; Sanchez, C. New route toward nanosized crystalline metal borides with tuneable stoichiometry and variable morphologies. *Faraday Discuss.* **2016**, *191*, 511-525. DOI: 10.1039/c6fd00053c.
(45) Liang, X.; Dong, R.; Li, D.; Bu, X.; Li, F.; Shu, L.; Wei, R.; Ho, J. C. Coupling of Nickel Boride and $Ni(OH)_2$ Nanosheets with Hierarchical Interconnected Conductive Porous Structure Synergizes the Oxygen Evolution Reaction. *ChemCatChem* **2018**, *10* (20), 4555-4561. DOI: 10.1002/cctc.201800993.
(46) Woo, K. E.; Kong, S.; Chen, W.; Chang, T. H.; Viswanathan, G.; Díez, A. M.; Sousa, V.; Kolen'ko, Y. V.; Lebedev, O. I.; Costa Figueiredo, M.; et al. Topotactic BI3-assisted borodization: synthesis and electrocatalysis applications of transition metal borides. *Journal of Materials Chemistry A* **2022**, *10* (40), 21738-21749. DOI: 10.1039/d2ta04266e.
(47) Gillan, E. G.; Kaner, R. B. Synthesis of Refractory Ceramics via Rapid Metathesis Reactions between Solid-State Precursors. *Chem. Mater.* **1996**, *8*, 333-343. DOI: 10.1021/cm950232a.
(48) Parkin, I. P. Solid State Metathesis Reaction For Metal Borides, Silicides, Pnictides and Chalcogenides: Ionic or Elemental Pathways. *Chem. Soc. Rev.* **1996**, *25* (3), 199-207.
(49) Wustrow, A.; Neilson, J. R. 5.03 - Metathesis routes to materials. In *Comprehensive Inorganic Chemistry III (Third Edition)*, Reedijk, J., Poeppelmeier, K. R. Eds.; Elsevier, 2023; pp 24-39.
(50) Abeysinghe, J. P.; Gillan, E. G. Thermochemical reaction strategies for the rapid formation of inorganic solid-state materials. In *Dynamic Processes in Solids*, 1st ed.; House, J. E. Ed.; Elsevier, 2023; pp 51-95.
(51) Jarvis, R. F., Jr.; Jacubinas, R. M.; Kaner, R. B. Self-Propagating Metathesis Routes to Metastable Group 4 Phosphides. *Inorg. Chem.* **2000**, *39* (15), 3243-3246. DOI: 10.1021/ic000057m.

(52) Treece, R. E.; Conklin, J. A.; Kaner, R. B. Metathetical Synthesis of Binary and Ternary Antiferromagnetic Gadolinium Pnictides (P, As, and Sb). *Inorg. Chem.* **1994**, *33* (25), 5701-5707. DOI: 10.1021/ic00103a016.
(53) Fitzmaurice, J. C.; Hector, A.; Parkin, I. P. RAPID SYNTHESIS OF TiN, HfN AND ZrN FROM SOLID-STATE PRECURSORS. *polyhedron* **1993**, *12* (11), 1295-1300.
(54) Gillan, E. G.; Kaner, R. B. Rapid Solid-State Synthesis of Refractory Nitrides. *Inorg. Chem.* **1994**, *33* (25), 5693-5700. DOI: 10.1021/ic00103a015.
(55) Wiley, J. B.; Gillan, E. G.; Kaner, R. B. RAPID SOLID STATE METATHESIS REACTIONS FOR THE SYNTHESIS OF COPPER OXIDE AND OTHER METAL OXIDES. *Mat. Res. Bull.* **1993**, *28* (9), 893-900. DOI: 10.1016/0025-5408(93)90035-c.
(56) Gillan, E. G.; Kaner, R. B. Rapid, energetic metathesis routes to crystalline metastable phases of zirconium and hafnium dioxide. *J. Mater. Chem.* **2001**, *11* (7), 1951-1956. DOI: 10.1039/b102234m.
(57) Bonneau, P. R.; Jarvis, R. F., Jr.; Kaner, R. B. Solid-State Metathesis as a Quick Route to Transition-Metal Mixed Dichalcogenides. *Inorg. Chem.* **1992**, *31* (11), 2127-2132. DOI: 10.1021/ic00037a027.
(58) Coleman, N., Jr.; Perera, S.; Gillan, E. G. Rapid solid-state metathesis route to transition-metal doped titanias. *J. Solid State Chem.* **2015**, *232*, 241-248. DOI: 10.1016/j.jssc.2015.09.028.
(59) Perera, S.; Zelenski, N. A.; Pho, R. E.; Gillan, E. G. Rapid and exothermic solid-state synthesis of metal oxyhalides and their solid solutions via energetic metathesis reactions. *J. Solid State Chem.* **2007**, *180* (10), 2916-2925. DOI: 10.1016/j.jssc.2007.08.005.
(60) Bonneau, P. R.; Kaner, R. B. High-quality mixed-transition-metal dichalcogenides from solid-state exchange reactions. *Inorganic Chemistry* **1993**, *32* (26), 6084-6087. DOI: 10.1021/ic00078a028.
(61) Rao, L.; Gillan, E. G.; Kaner, R. B. Rapid synthesis of transition-metal borides by solid-state metathesis. *J. Mater. Res.* **1995**, *10* (2), 353-361.
(62) Abeysinghe, J. P.; Kolln, A. F.; Gillan, E. G. Rapid and Energetic Solid-State Metathesis Reactions for Iron, Cobalt, and Nickel Boride Formation and Their Investigation as Bifunctional Water Splitting Electrocatalysts. *ACS Mater. Au* **2022**, *2* (4), 489-504. DOI: 10.1021/acsmaterialsau.1c00079.
(63) Patil, K.; Babar, P.; Li, X.; Karade, V.; Kim, S.; Jang, S. Y.; Bhoite, P.; Kim, J. H. Co–Fe–B Nanochain Electrocatalysts for Oxygen Evolution at High Current Density. *ACS Appl. Nano Mater.* **2022**, *5* (5), 6260-6267. DOI: 10.1021/acsanm.2c00312.
(64) Liu, X.; He, G.; Liu, H.; Zhu, Y.; Xiao, J.; Han, L. Boron-doped cobalt-iron bimetal phosphides nanosheets for enhanced oxygen evolution. *J. Alloys Compd.* **2022**, *893*. DOI: 10.1016/j.jallcom.2021.162208.
(65) Chen, H.; Ouyang, S.; Zhao, M.; Li, Y.; Ye, J. Synergistic Activity of Co and Fe in Amorphous Co*x*-Fe-B Catalyst for Efficient Oxygen Evolution Reaction. *ACS Appl. Mater. Interfaces* **2017**, *9* (46), 40333-40343. DOI: 10.1021/acsami.7b13939.
(66) Zou, X.; Zhang, W.; Zhou, X.; Song, K.; Ge, X.; Zheng, W. The surface of metal boride tinted by oxygen evolution reaction for enhanced water electrolysis. *J. Energy Chem.* **2022**, *72*, 509-515. DOI: 10.1016/j.jechem.2022.05.0392095-4956.
(67) Nsanzimana, J. M. V.; Gong, L.; Dangol, R.; Reddu, V.; Jose, V.; Xia, B. Y.; Yan, Q.; Lee, J. M.; Wang, X. Tailoring of Metal Boride Morphology via Anion for Efficient Water Oxidation. *Adv. Energy Mater.* **2019**, *9* (28), 1901503. DOI: 10.1002/aenm.201901503.
(68) Kapfenberger, C.; Albert, B.; Pottgen, R.; Huppertz, H. Structure refinements of iron borides Fe_2B and FeB. *Z Kristallogr* **2006**, *221* (5-7), 477-481. DOI: 10.1524/zkri.2006.221.5-7.477.
(69) Bjurstrom, T. Rontgenanalyse der Systeme Eisen-Bor, Kobalt-Bor und Nickel-Bor. *Ark. Kemi, Mineral. Geo.* **1933**, *11A*, 1.
(70) Gianoglio, C.; Quadrini, E. Sul sistema cobalto-ferro-boro. *Atti Accad. Sci. Torino, Cl. Sci. Fis., Mat. Nat.* **1980**, *114*, 125.
(71) Coleman, N., Jr.; Liyanage, I. A.; Lovander, M. D.; Leddy, J.; Gillan, E. G. Facile Solvent-Free Synthesis of Metal Thiophosphates and Their Examination as Hydrogen Evolution Electrocatalysts. *Molecules* **2022**, *27* (16), 5053. DOI: 10.3390/molecules27165053.

(72) McCrory, C. C.; Jung, S.; Peters, J. C.; Jaramillo, T. F. Benchmarking heterogeneous electrocatalysts for the oxygen evolution reaction. *J. Am. Chem. Soc.* **2013**, *135* (45), 16977-16987. DOI: 10.1021/ja407115p.
(73) Binnewies, M.; Milke, E. *Thermochemical Data of Elements and Compounds*; Weinheim, 1999.
(74) *CRC Handbook of Chemistry and Physics, 102nd Edition (Internet Version 2021)*; Rumble, J. R., Ed.; CRC Press/Taylor & Francis.
(75) Kubaschewski, O.; Alcock, C. B. *Metallurgical Thermochemistry*; Pergamon Press Inc., Maxwell House, 1979.
(76) NIST Chemistry Webbook. Standard Reference Database. (accessed 7/5/2021).
(77) Yu, L.; Ren, Z. Systematic study of the influence of iR compensation on water electrolysis. *Mater. Today Phys.* **2020**, *14*. DOI: 10.1016/j.mtphys.2020.100253.
(78) Anantharaj, S.; Ede, S. R.; Karthick, K.; Sankar, S. S.; Sangeetha, K.; Karthik, P. E.; Kundu, S. Precision and correctness in the evaluation of electrocatalytic water splitting: revisiting activity parameters with a critical assessment. *Energy Environ. Sci.* **2018**, *11* (4), 744-771. DOI: 10.1039/c7ee03457a.
(79) Shinagawa, T.; Garcia-Esparza, A. T.; Takanabe, K. Insight on Tafel slopes from a microkinetic analysis of aqueous electrocatalysis for energy conversion. *Sci. Rep.* **2015**, *5*, 13801. DOI: 10.1038/srep13801 From NLM PubMed-not-MEDLINE.
(80) Masa, J.; Weide, P.; Peeters, D.; Sinev, I.; Xia, W.; Sun, Z.; Somsen, C.; Muhler, M.; Schuhmann, W. Amorphous Cobalt Boride (Co_2B) as a Highly Efficient Nonprecious Catalyst for Electrochemical Water Splitting: Oxygen and Hydrogen Evolution. *Adv. Energy Mater.* **2016**, *6*, 1502313. DOI: 10.1002/aenm.201502313.

TOC Entry (graphical abstract)

Rapid solid-state metathesis (SSM) reactions between four reactants form crystalline solid-solution cobalt iron monoborides. These mixed metal borides show improved HER activity that primarily correlates with higher cobalt content.

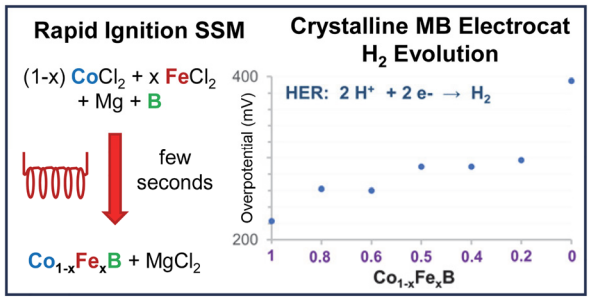

Supporting Information for

Rapid solid-state metathesis reactions for the formation of cobalt-iron monoboride solid-solutions and investigation of their water splitting electrocatalytic activity

Janaka P. Abeysinghe, Edward G. Gillan*
Department of Chemistry, University of Iowa, Iowa City, Iowa 52242
E-mail: edward-gillan@uiowa.edu

Tables and Figures are ordered as they are first referenced in the main text of the paper.

List of Experimental, Tabular, and Graphical Supporting Information

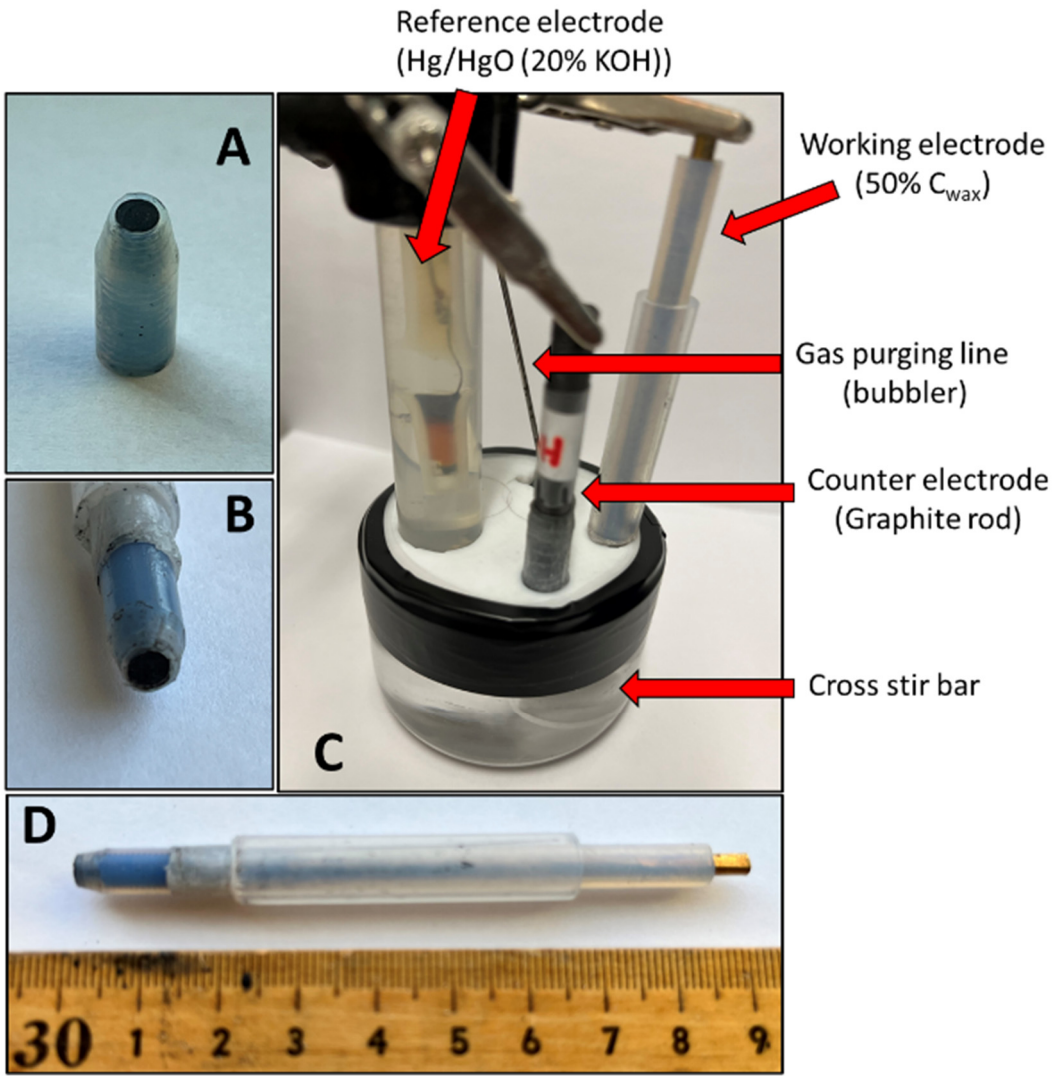

Figure S1. Images of electrochemical cell and electrode tip. (A) bare C_{wax} electrode tip (B) C_{wax} electrode tip with MB powder on it, (C) Three electrode electrochemical cell (working electrode-C_{wax}, counter electrode-graphite rod, reference electrode- Hg/HgO (20% KOH), bubbler, and cross stir bar, (D) assembled C_{wax} electrode tip+brass rod connector.

Table S1. Literature table for metal compounds synthesized from SSM reactions.
RT = room temperature; Filament initiation (ignition SSM) reactions can initiate at room temperature by passing a current through nichrome/ cu wire, however locally nichrome wire temperature rises to <=850 °C when passing the current and initiate the reaction. * Can be named as magnesiothermic reduction reaction as well. # Not a single-phase product.

Year	Material	Starting Materials	Initiation	Reaction Initiation Temp (°C)	Time	Ref.
1995	TiB_2, ZrB_2, HfB_2	MCl_x+MgB_2	Ampoule	850	18 h	1
	VB_2, NbB_2, TaB_2, FeB, CrB_2#, MoB_2#		Filament	RT	in sec	
2002	UB_4	UCl_4+MgB_2	Ampoule	850	1 day	2
2012	MB_6 (M=Ca, Ba, Sr)	MCl_2+MgB_2	quartz tube	850-900 (10^{-3} Torr)	12 hr	3
2013	CeB_6, NdB_6, SmB_6, EuB_6, GdB_6, YbB_6	$MCl_3.6H_2O+MgB_2$	Reactants in an Alsint boat covered by a silicon wafer and then inserted in a Quartz tube	650	1 hr	4
2017	MoB_2	$MoCl_5+MgB_2$	Quartz tube	650	24 hr	5
2019	CrB_2#, MnB_4, FeB, CoB	MCl_2+MgB_2		850	10 hr	6
	TiB_2, ZrB_2, HfB_2	MCl_4+MgB_2		850	10 hr	
	VB_2	VCl_3+MgB_2		850	10 hr	
	NbB_2, TaB_2, MoB_2	MCl_5+MgB_2		850	10 hr	
	WB_x	WCl_6+MgB_2		850	10 hr	
	ReB_2	$K_2ReCl_6+MgB_2$		850	10 hr	
	OsB_2#	$K_2OsCl_6+MgB_2$		1100	10 hr	
	RuB_2	$K_2RuCl_5+MgB_2$		950	3 hr	
2020	MB (M=V,Cr,Nb,Mo,Ru, Ta,W)	MCl_x+MgB_2+Mg*	Quartz tube	800-950	5-9 hr	7
2020	Ru_7B_3, RuB	$K_2RuCl_5+MgB_2+$ Mg*	Quartz tube	700-950	3-10 hr	8
	Ru_2B_3, RuB_2	K_2RuCl_5 +MgB_2				
2022	FeB, CoB, NiB#	MCl_x+MgB_2	Filament	RT	In sec	9
	FeB, CoB, NiB	$MCl_x+Mg+(x/2)B$ *				

Table S2. Unit cell parameters of CoB, FeB, and $Co_{1-x}Fe_xB$ crystalline systems.

	Co %	a (Å)	b (Å)	c (Å)	Cell volume (Å^3)
CoB standard pattern (PDF 04-003-2122)		3.948	5.243	3.037	62.9
CoB	100	3.9557	5.2498	3.0417	63.2
CoB (conv.)	100	5.2498	3.0417	3.9557	63.2
$Co_{0.8}Fe_{0.2}B$	80	5.3177	3.0166	3.9793	63.8
$Co_{0.6}Fe_{0.4}B$	60	5.3718	2.9949	3.9981	64.3
$Co_{0.5}Fe_{0.5}B$	50	5.3984	2.9806	4.012	64.6
$Co_{0.4}Fe_{0.6}B$	40	5.424	2.973	4.0276	64.9
$Co_{0.2}Fe_{0.8}B$	20	5.4713	2.9563	4.0454	65.4
FeB	0	5.5006	2.9476	4.0600	65.8
FeB standard pattern (PDF 04-013-1637)	0	5.504	2.945	4.056	65.7
$Co_{0.5}Fe_{0.5}B$ standard pattern (PDF 01-079-2846)	50	5.4042	2.9803	4.0072	64.5

CoB, FeB, and $Co_{0.5}Fe_{0.5}B$ ($CoFeB_2$) crystalize in the orthorhombic crystal system. However, space groups of CoB (Pnma) are different from FeB and $Co_{0.5}Fe_{0.5}B$ (Pnma). The unit cell growth of CoB along a, b, and c axis are different from FeB or $Co_{1-x}Fe_xB$ solid-solutions. The a, b, and c values of CoB swapped to match with FeB and $Co_{1-x}Fe_xB$ cell directions are also shown (blue-color values).

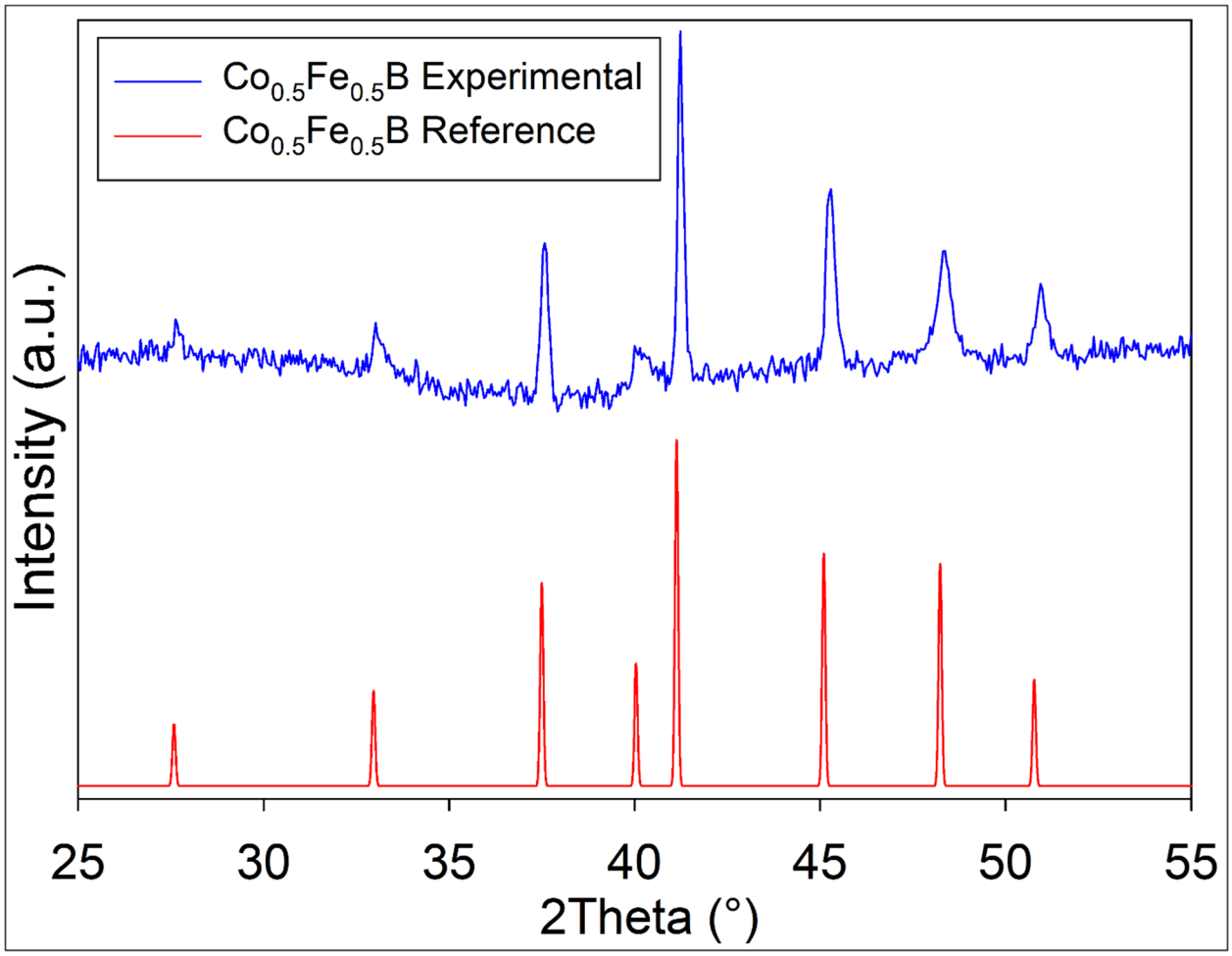

Figure S2. XRD comparison of experimentally obtained versus reference $Co_{0.5}Fe_{0.5}B$ (PDF 01-079-2846).

Table S3a. 2θ and d-spacing values of crystal planes (hkl) of FeB, $Co_{0.2}Fe_{0.8}B$, $Co_{0.4}Fe_{0.6}B$, and $Co_{0.5}Fe_{0.5}B$. Peak alignment was made using an internal Si standard.

	FeB		**$Co_{0.2}Fe_{0.8}B$**		**$Co_{0.4}Fe_{0.6}B$**		**$Co_{0.5}Fe_{0.5}B$**	
hkl	**d (Å)**	**2θ**	**d (Å)**	**2θ**	**d (Å)**	**2θ**	**d (Å)**	**2θ**
101	3.26656	27.3008	3.25282	27.4184	3.23360	27.5846	3.22012	27.6785
200	2.75030	32.5558	2.73565	32.7351	2.71200	33.0287	2.69919	33.1612
011	2.38526	37.7123	2.38688	37.6858	2.39193	37.6032	2.39258	37.5598
201	2.27703	39.5777	2.26614	39.7759	2.24955	40.0817	2.23953	40.2335
111	2.18837	41.2526	2.18775	41.2647	2.18857	41.2487	2.18737	41.2360
210	2.01089	45.0842	2.00788	45.1557	2.00360	45.2573	2.00071	45.2860
102	1.90445	47.7559	1.89720	47.9496	1.88788	48.2014	1.88039	48.3621
211	1.80198	50.6571	1.79853	50.7611	1.79389	50.9017	1.79044	50.9608
301	1.67103	54.9462	1.66262	55.2479	1.64943	55.7279	1.64188	55.9554
112	1.59962	57.6228	1.59669	57.7383	1.59371	57.8565	1.59035	57.9368
020	1.47380	63.0768	1.47815	62.8699	1.48650	62.4769	1.49028	62.2422

Table S3b. 2θ and d-spacing values of crystal planes (hkl) of $Co_{0.6}Fe_{0.4}B$, $Co_{0.8}Fe_{0.2}B$, and CoB.

	$Co_{0.6}Fe_{0.4}B$		**$Co_{0.8}Fe_{0.2}B$**		**CoB**		
hkl	**d (Å)**	**2θ**	**d (Å)**	**2θ**	**hkl**	**d (Å)**	**2θ**
101	3.20730	27.8154	3.18604	28.0047	**110**	3.15925	28.2471
200	2.68590	33.3590	2.65885	33.7084	**020**	2.62490	34.1577
011	2.39699	37.5209	2.40392	37.4086	**101**	2.41126	37.2905
201	2.22952	40.4575	2.21077	40.8159	**111**	2.19119	41.1972
111	2.18895	41.2411	2.19050	41.2107	**120**	2.18717	41.2764
210	1.99907	45.3655	1.98967	45.5919	**021**	1.98724	45.6509
102	1.87355	48.5939	1.86350	48.8728	**210**	1.85085	49.2290
211	1.78838	51.0698	1.78316	51.2300	**121**	1.77575	51.4594
301	1.63419	56.2934	1.61919	56.8622	**130**	1.60033	57.5946
112	1.58835	58.0703	1.58539	58.1893	**211**	1.58114	58.3607
020	1.49745	61.9693	1.50828	61.4758	**002**	1.52085	60.9135

Table S4. Co/Fe metal ratio comparison from ICP, XRF, and EDS results.

SSM reaction molar ratios	Final Products	Theoretical Co/Fe	ICP Co/Fe	XRF Co/Fe	EDS Co/Fe
4$CoCl_2$/$FeCl_2$/5Mg/10B	$Co_{0.8}Fe_{0.2}B$+B	80/20	81/19	78/22	78/22
3$CoCl_2$/2$FeCl_2$/5Mg/10B	$Co_{0.6}Fe_{0.4}B$+B	60/40	58/42	-	55/45
2.5$CoCl_2$/2.5$FeCl_2$/5Mg/10B	$Co_{0.5}Fe_{0.5}B$+B	50/50	48/52	49/51	45/55
2$CoCl_2$/3$FeCl_2$/5Mg/10B	$Co_{0.4}Fe_{0.6}B$+B	40/60	38/62	-	33/67
$CoCl_2$/4$FeCl_2$/5Mg/10B	$Co_{0.2}Fe_{0.8}B$+B	20/80	17/83	21/79	19/81

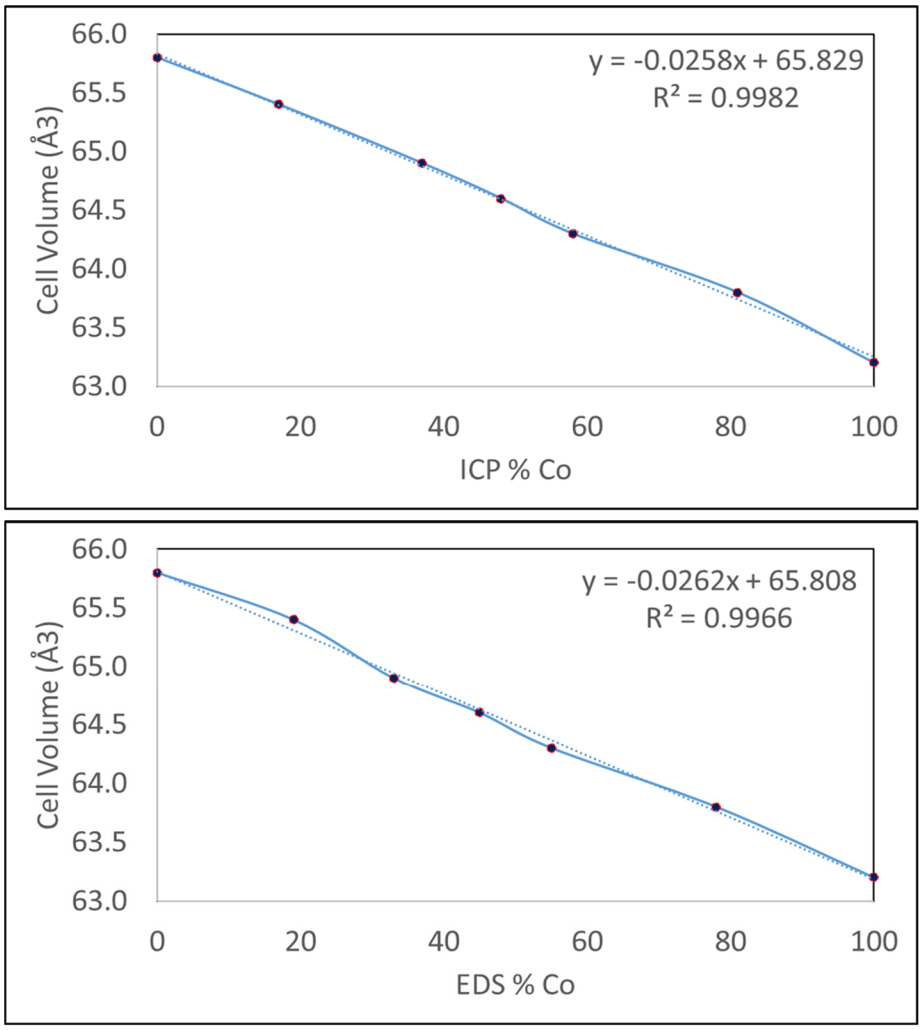

Figure S3. Unit cell volume changes with ICP and EDS measurements obtained %Co values of $Co_{1-x}Fe_xB$ solid-solutions. Dashed lines are linear regression results.

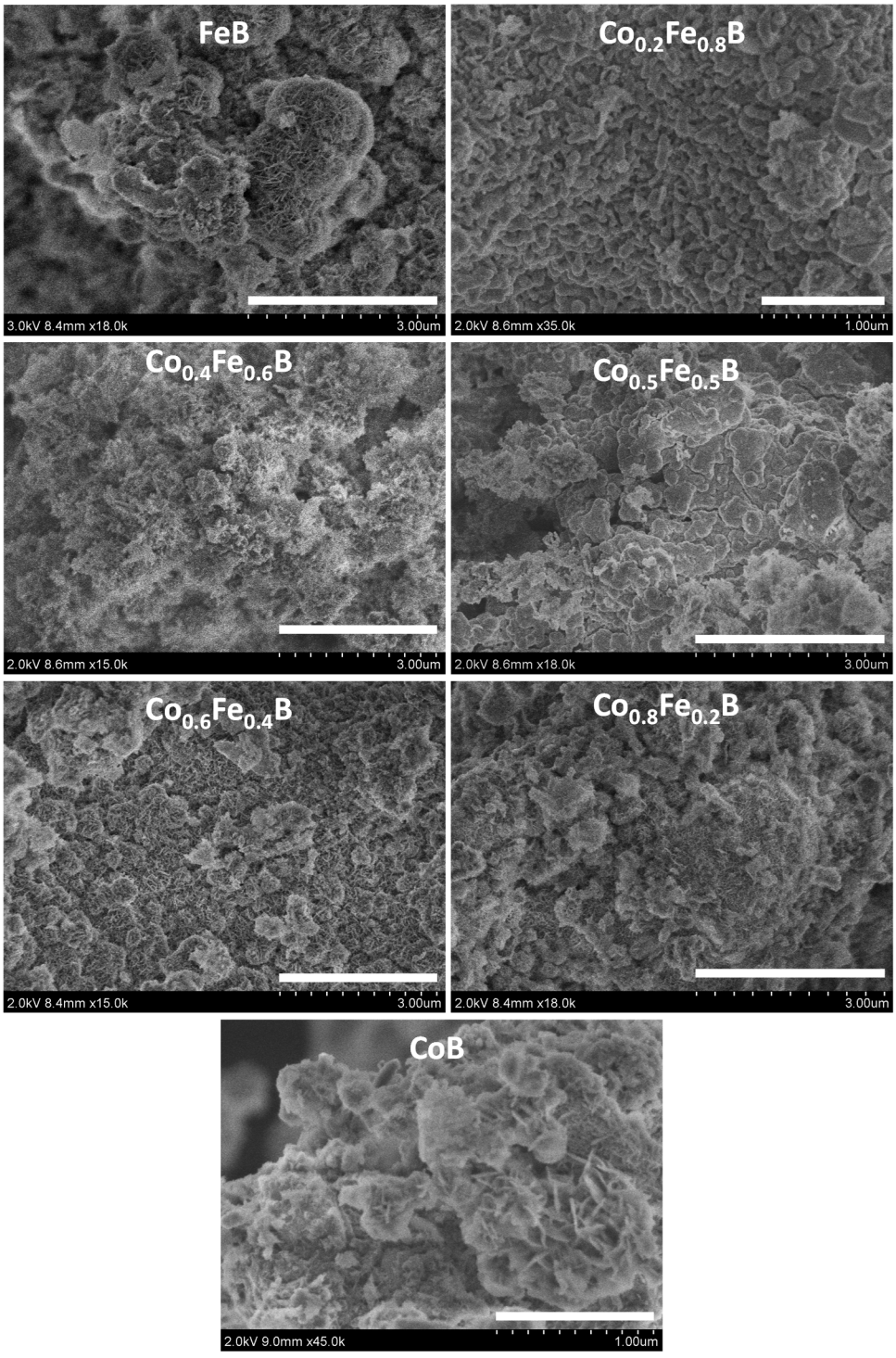

Figure S4. Additional high-magnification SEM images of FeB, $Co_{1-x}Fe_xB$ solid-solutions, and CoB. In all samples vertically grown plate-like structure morphology can be observed that may receive on metal boride surfaces after washing out $MgCl_2$ byproduct from product. The lengths of the scale bars: FeB, $Co_{0.4}Fe_{0.6}B$, $Co_{0.5}Fe_{0.5}B$, $Co_{0.6}Fe_{0.4}B$, and $Co_{0.8}Fe_{0.2}B$ are 3 μm and $Co_{0.2}Fe_{0.8}B$ and CoB are 1 μm.

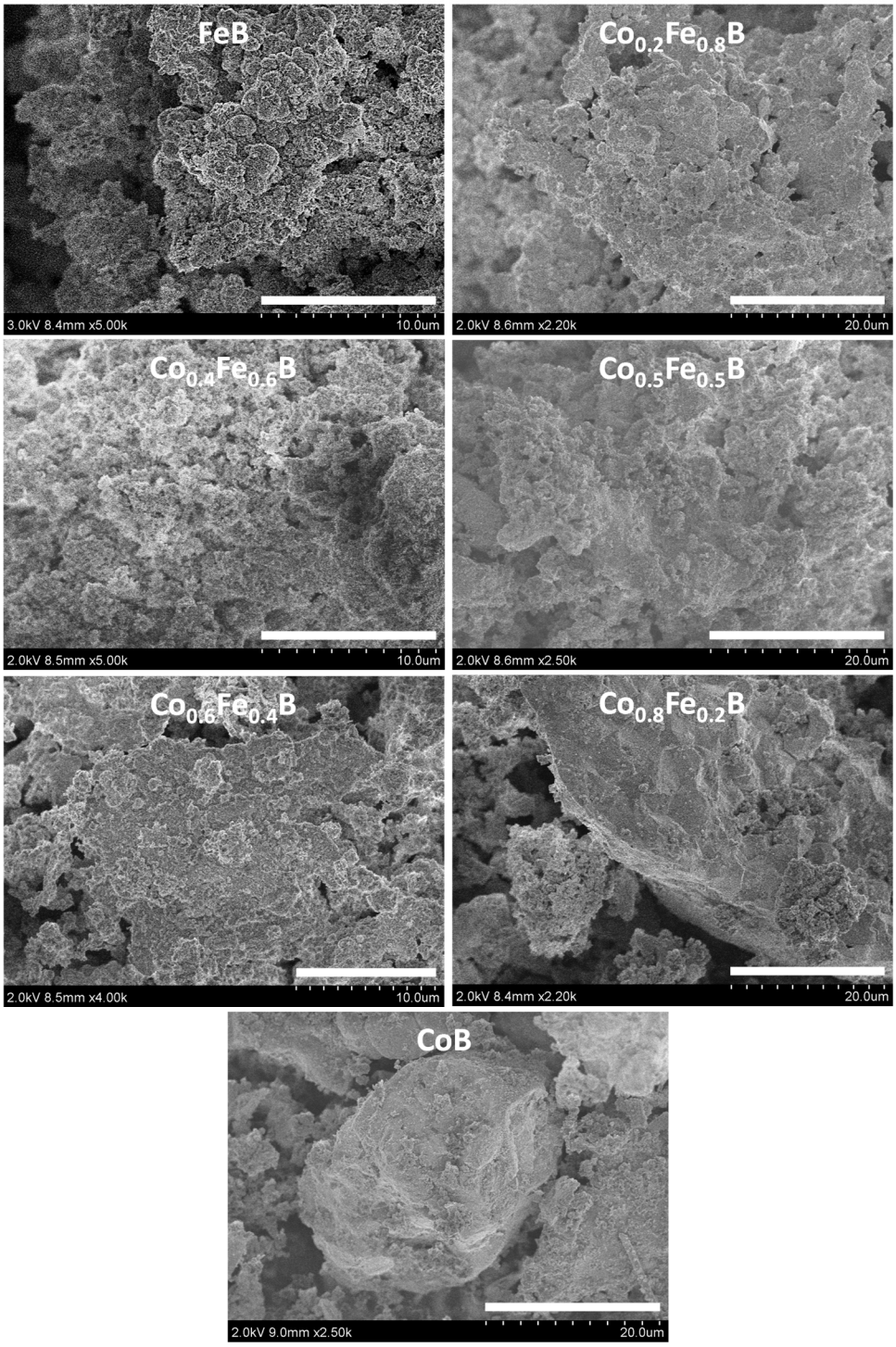

Figure S5. Low-magnification SEM images of FeB, $Co_{1-x}Fe_xB$ solid-solutions, and CoB. Apparent morphology transformation from aggregates of small and round-shaped FeB particles to large (μm-sized) monolithic blocks + aggregate particles of CoB through $Co_{1-x}Fe_xB$ solid-solutions can be seen from these low-magnification images. The lengths of the scale bars: FeB, $Co_{0.4}Fe_{0.6}B$, and $Co_{0.6}Fe_{0.4}B$ are 10 μm and $Co_{0.2}Fe_{0.8}B$, $Co_{0.5}Fe_{0.5}B$, $Co_{0.8}Fe_{0.2}B$, and CoB are 20 μm.

Table S5. The crystallite sizes of $Co_{1-x}Fe_xB$ solid-solutions determined by X-ray line broadening.

Metal boride	CoB	$Co_{0.8}Fe_{0.2}B$	$Co_{0.6}Fe_{0.4}B$	$Co_{0.5}Fe_{0.5}B$	$Co_{0.4}Fe_{0.6}B$	$Co_{0.2}Fe_{0.8}B$	FeB
Sample 1 (nm)	43.9	49.5	60.4	66.0	58.0	69.0	67.5
Sample 2 (nm)	52.5	50.9	60.4	73.4	61.4	60.8	62.0
Average (nm)	**48.2**	**50.2**	**60.4**	**69.7**	**59.7**	**64.9**	**64.8**

The (220) XRD peak at 47.3° 2θ of Si powder was used for instrument broadening and the (111) peaks of metal borides (41.236°) were used for the calculations. Two different sample scan results were obtained for each metal boride using Scherrer and Warren equations.

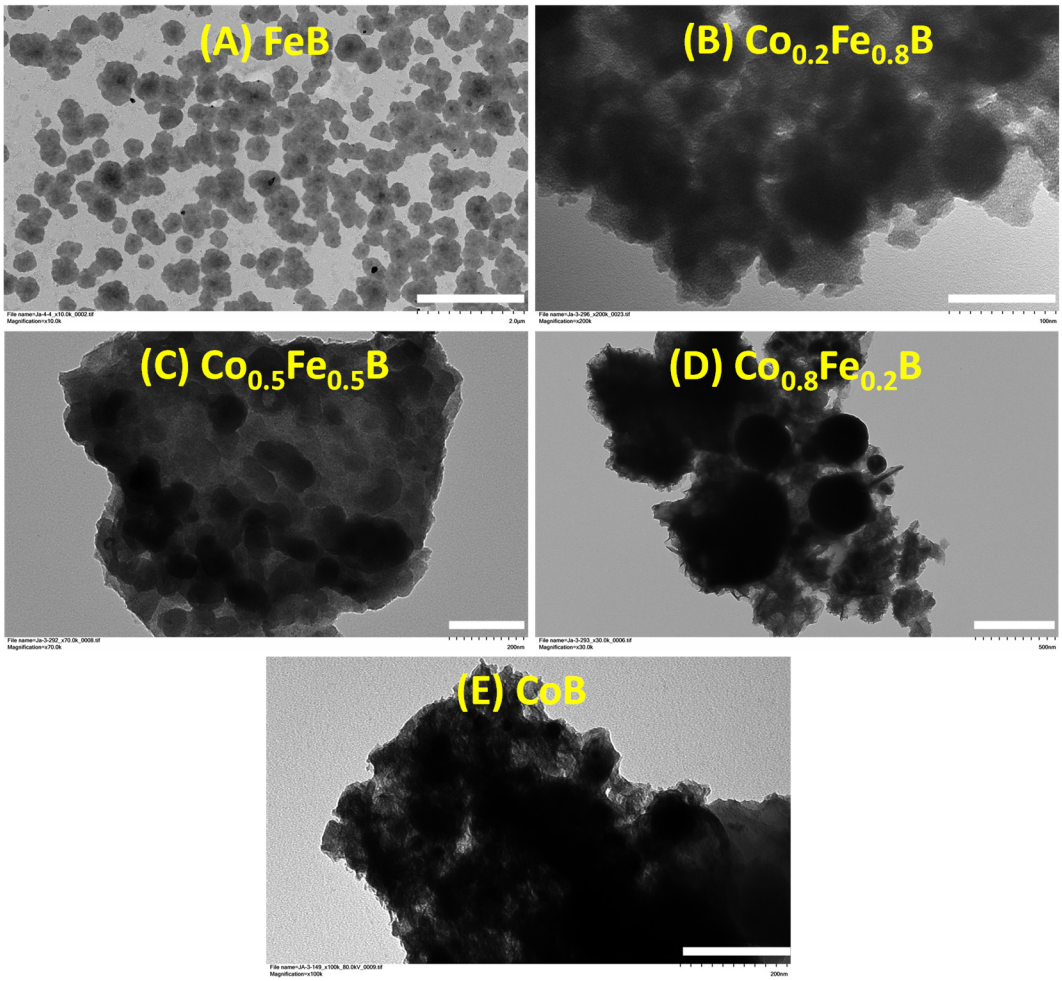

Figure S6. TEM images of FeB, CoB, and $Co_{1-x}Fe_xB$ solid-solutions. Scale bar length for images: (A) 2 μm, (B) 100 nm, (C) 200 nm, (D) 500 nm, (E) 200 nm.

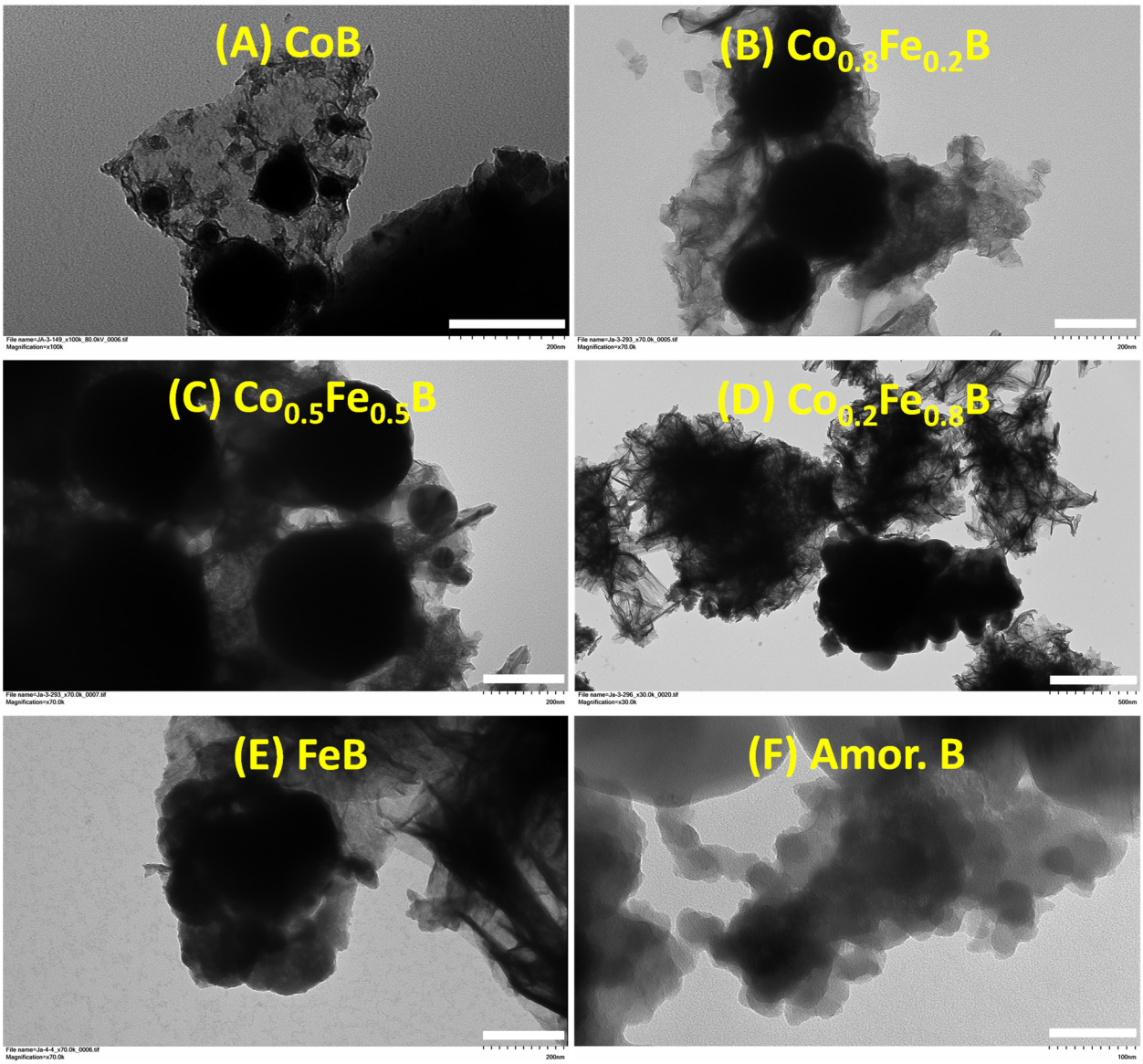

Figure S7. Additional TEM images of $Co_{1-x}Fe_xB$ solid-solutions, FeB, CoB, and amorphous B. Scale bar lengths: (A), (B), (C), (E) – 200 nm, (D) – 500 nm, (F) – 100 nm.

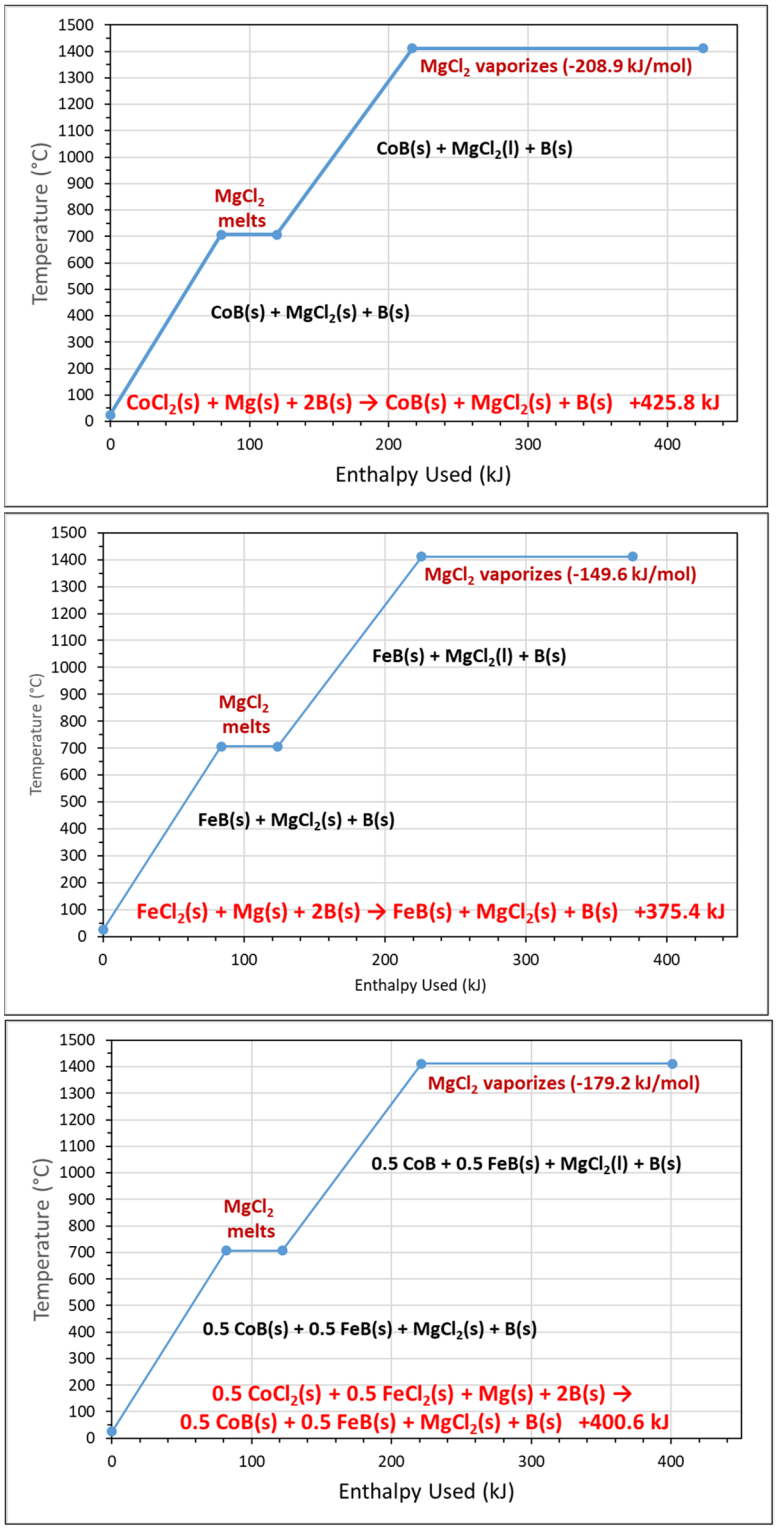

Figure S8. A plot of calculated adiabatic temperature data for CoB, FeB, and 0.5CoB+0.5FeB ($Co_{0.5}Fe_{0.5}B$) samples. Data points were calculated using the heat of reaction, standard heat capacities, and phase change energies. All three samples temperature-enthalpy graphs are very similar except reaction final step, $MgCl_2$ vaporization, acquired different enthalpies and resulting different % of $MgCl_2$ vaporizations (CoB: 100%, FeB: 72%, $Co_{0.5}Fe_{0.5}B$: 86%).

Sample calculations for reaction heat and adiabatic temperature

All thermochemical data of compounds were obtained from several thermochemical reference sources.[10, 11]

SSM reactions enthalpy calculations. An example of a thermochemical ΔH_{rxn} calculation that was done using Hess's Law for the $4CoCl_2/FeCl_2/5Mg/10B$ reaction. Since shortage of thermochemistry data of $Co_{1-x}Fe_xB$ solid solutions, CoB and FeB formation separately considered for the calculations.

	0.8 $CoCl_2$	+	0.2 $FeCl_2$	+	Mg	+	2B	→	0.8 CoB	+	0.2 FeB	+	$MgCl_2$	+	B
ΔH_f(kJ/mol)	-312.5		-341.6		0		0		-94.1		-72.8		-644.2		0

ΔH_{rxn} (kJ/mol CoB+FeB) $= \Sigma\Delta H_f$(products) - $\Sigma\Delta H_f$ (reactants) = -415.7

Maximum adiabatic reaction temperature (T_{ad}) calculations. For the T_{ad} calculations, complete reaction progress and no heat loss of reactions were assumed. Even though SSM reactions are very rapid, some heat loss from the reactor to the surrounding environment is possible in practice. As a result, actual maximum reaction temperatures may be lower than calculated adiabatic reaction temperatures (T_{ad}). The standard molar heat capacities (298 K and 1 atm) were used for solid compounds and molar heat capacities at melting and boiling temperatures were selected as the heat capacity of compounds in liquid and gas phases at 298 K.[10] Molar heat capacities of materials (mostly solids) generally increase with temperature, so the T_{ad} values represent upper limits of likely temperatures reached in these SSM reactions.

The T_{ad} calculation of $4CoCl_2/FeCl_2/5Mg/10B$ reaction.

	0.8 $CoCl_2$	+ 0.2 $FeCl_2$	+ Mg	+ 2 B	→	0.8 CoB	+ 0.2 FeB	+ $MgCl_2$	+ B	ΔH°_{rxn}	-415.7 (kJ/mol)
ΔH°_f (kJ/mol)	-312.5	-341.6	0	0		-94.1	-72.8	-644.2	0		
mp (C)	721	677	650	2077		1460	1590	707	2077		
bp (C)	1081	1020	1093	3866				1412	3866		
Heat of fusion (kJ/mol)						62.66	62.66	40.0			
Heat of vaporization (kJ/mol)								209.1			
C_p (j/mol K) (solid)						34.6	41.0	71.3	10.71		
C_p (j/mol K) (liquid)						61.5	68.3	92.8	31.75		
C_p (j/mol K) (gas)								57.1	20.8		

		ΔH =CpΔT
25 °C -707 °C	Products heat up to MgCl2 melting temp.	80.4
707 °C	$MgCl_2(s) \rightarrow MgCl_2(l)$	40.0
707 °C - 1412 °C	Products heat up to MgCl2 boiling temp.	98.3
1412 °C	$MgCl_2(l) \rightarrow MgCl_2(g)$	209.1

Final T_{ad} = 1412 °C

Table S6. Results for xCoCl$_2$ + (1-x)FeCl$_2$ + Mg rapid SSM reactions.

Reaction	% Yield based on target metal M	ΔH_f (kJ/mol)	Magnetic attraction
0.8CoCl$_2$ / 0.2FeCl$_2$/ Mg	55	-326	strong
0.5CoCl$_2$ / 0.5FeCl$_2$/ Mg	49	-317	strong
0.2CoCl$_2$ / 0.8FeCl$_2$/ Mg	46	-308	strong

All three products are ferromagnetic at room temperature, and they qualitatively show strong attraction to a permanent magnet.

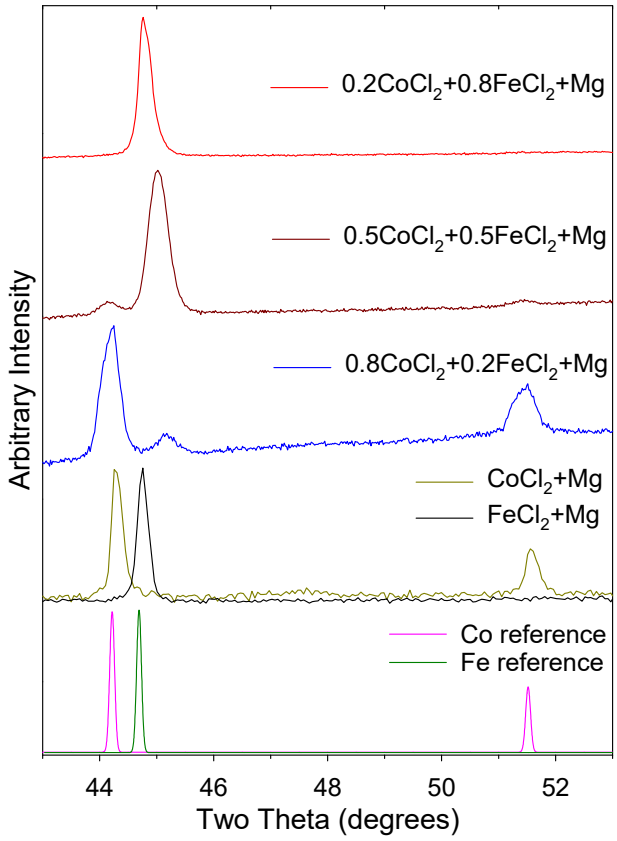

Figure S9. Powder XRD results of the (1-x)CoCl$_2$/xFeCl$_2$/Mg mechanistic study 1st half-reactions.

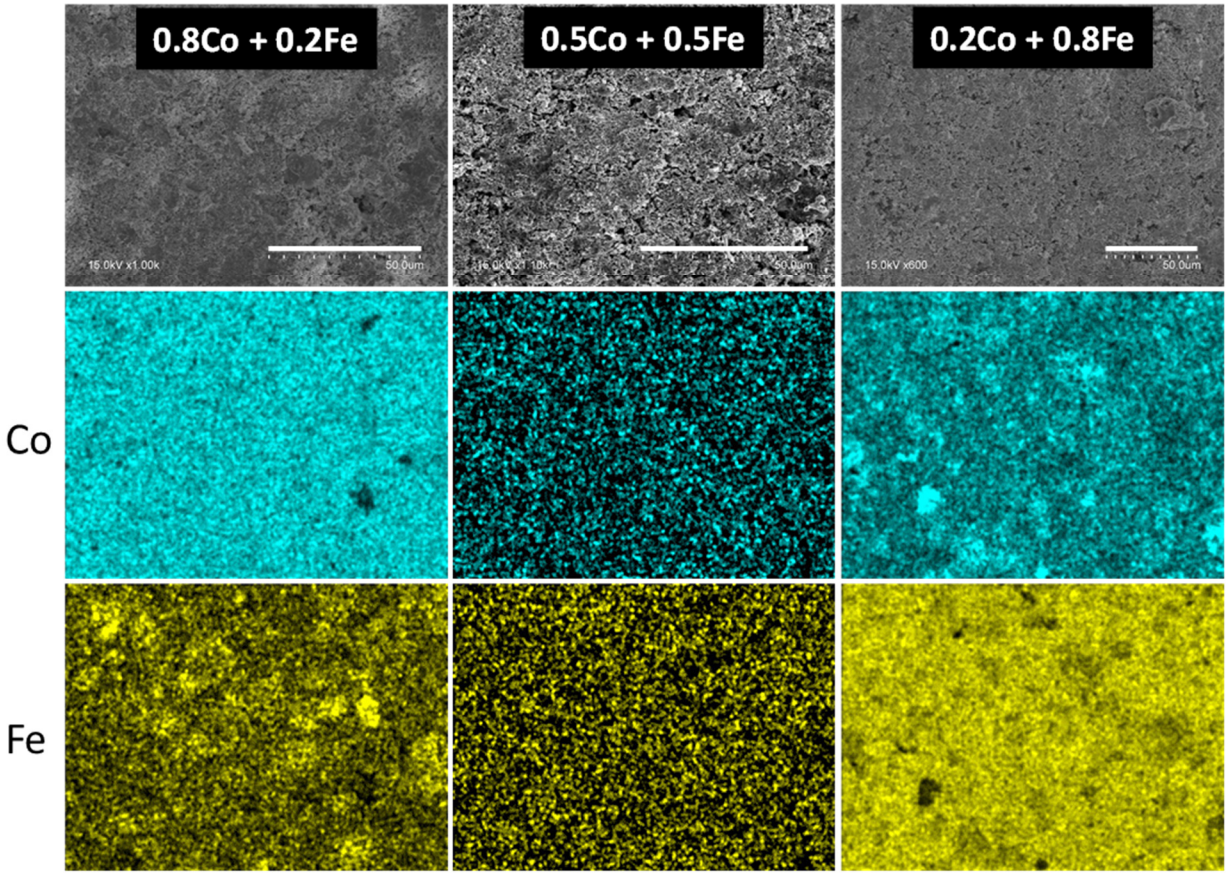

EDS analysis					
Co%	Fe%	Co%	Fe%	Co%	Fe%
90	10	59	41	30	70

Figure S10. EDS maps of (A) 0.8Co/0.2Fe, (B) 0.5Co/0.5Fe, and (C) 0.2Co/0.8Fe formed from x $CoCl_2$ + (1-x) $FeCl_2$+Mg mechanistic study reactions. The length of the scale bars are: (A, B, C) 50 μm.

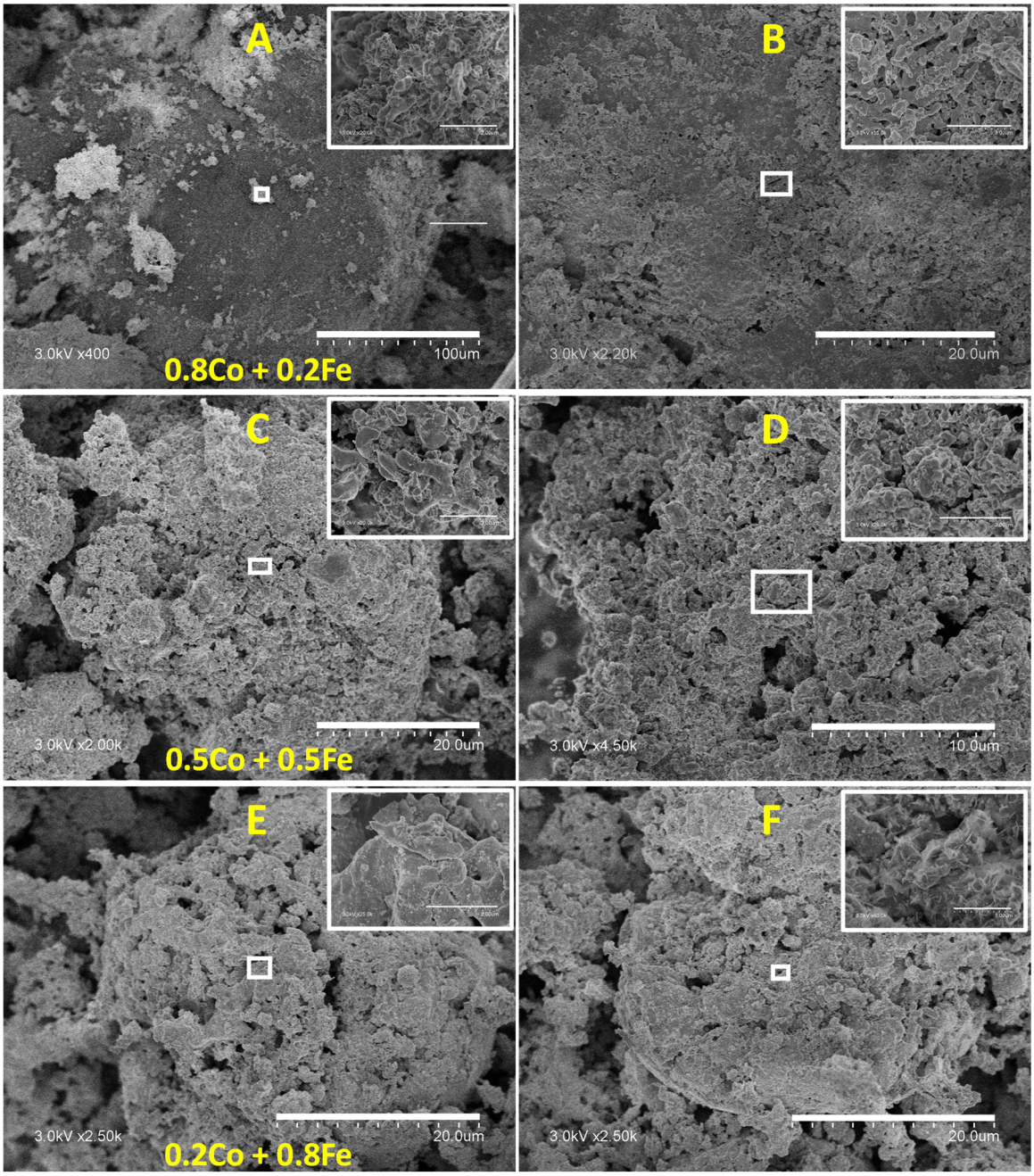

Figure S11. Scanning electron microscopy (SEM) comparison of particle morphologies obtained from SSM reactions of xCoCl$_2$ + (1-x)FeCl$_2$+Mg producing (A and B) 0.8Co/0.2Fe, (C and D) 0.5Co/0.5Fe, and (E and F) 0.2Co/0.8Fe (left column and right column are two representative SEM images of the same sample). Insets show a high magnification view of the highlighted white boxes in the low magnification images. The lengths of the scale bars are (main image, inset): (A) 100 µm and 2 µm, (B) 20 µm and 3 µm, (C) 20 µm and 2 µm, (D) 10 µm and 2 µm, (E) 20 µm and 2 µm, (F) 20 µm and 1 µm.

Table S7. Literature comparison table for crystalline and amorphous binary metal boride OER and HER activity in different electrolytes. All current densities are normalized for the geometric electrode area. The η_{10} overpotentials are calculated versus the ideal equilibrium 0 V and 1.23 V potentials for HER and OER water splitting.

MB (M= Fe, Co, Ni)	Electrode	OER (η_{10} mV)	HER (η_{10} mV)	Tafel slope (mV/dec) OER/HER	Electrolyte	Ref.
Crystalline metal borides (Co and Fe)						
CoB ($CoCl_2$/Mg/2B)	50% C_{wax}	345	-223	95/105	1.0 M KOH	this study
FeB ($FeCl_2$/Mg/2B)	50% C_{wax}	456	-395	52/136	1.0 M KOH	this study
FeB ($FeCl_3$/1.5MgB_2)	45% C_{wax}	418	-368	78/157	1.0 M KOH	[9]
FeB ($FeCl_3$/1.5Mg/B)	45% C_{wax}	480	-361	116/155	1.0 M KOH	[9]
CoB ($CoCl_2$/MgB_2)	45% C_{wax}	373	-293	54/109	1.0 M KOH	[9]
CoB ($CoCl_2$/Mg/2B)	45% C_{wax}	382	-279	69/100	1.0 M KOH	[9]
FeB_2	GC	296	-61	52/88	1.0 M KOH	[12]
Co_3B	CP	312		53	1.0 M KOH	[13]
Co_2B	GC	410		63	1.0 M KOH	[14]
Co_2B		380		45	0.1 M KOH	[15]
Co_2B	GC		-328	136, 177	1.0 M KOH	[15]
Co_2B	CP	287		51	1.0 M KOH	[13]
CoB	CP	340		63	1.0 M KOH	[13]
Crystalline metal borides (Other)						
NiB ($NiCl_2$/MgB_2)	45% C_{wax}	380	-312	72*/112	1.0 M KOH	[9]
NiB ($NiCl_2$/Mg/2B)	45% C_{wax}	346	-307	67*/111	1.0 M KOH	[9]
Ni_3B	-		-79	85	0.5 M H_2SO_4	[16]
NiB	GC	350		60	1.0 M KOH	[17]
Nano VB_2	CS		-192	68	0.5 M H_2SO_4	[18]
Bulk VB_2	CS		-348	126	0.5 M H_2SO_4	[18]
TiB_2	GC		-1070	196	0.5 M H_2SO_4	[19]
TiB_2	FTO	560			1.0 M $HClO_4$	[20]
TiB_2	GC		~-1100		0.5 M H_2SO_4	[21]
TiB_2-NaNAFT	GC		~-1000	146	0.5 M H_2SO_4	[21]
TiB_2-BuLi	GC		~-1000	158	0.5 M H_2SO_4	[21]
ZrB_2	GC		-970	173	0.5 M H_2SO_4	[19]
MoB/g-C_3N_4	GC		-152 (η_{20})	46	1.0 M KOH	[22]
MoB_2	CS		-154	49	0.5 M H_2SO_4	[5]
Mo_2B_5	GC		-740	118	0.5 M H_2SO_4	[23]
Mo_2B_5-BP treated	GC		-540	101	0.5 M H_2SO_4	[23]
RuB_2	GC		-28	29	1.0 M KOH	[6]
RuB_2	GC		-18	39	0.5 M H_2SO_4	[6]
RuB_2	GC		-35	28	0.5 M H_2SO_4	[24]
HfB_2	GC		-1050	194	0.5 M H_2SO_4	[19]
WB_2	GC		-203	65	0.5 M H_2SO_4	[24]
W_2B_5	GC		-680	115	0.5 M H_2SO_4	[23]
W_2B_5-BP treated	GC		-210	62	0.5 M H_2SO_4	[23]

Amorphous metal borides						
FeB	GC	392 (η_{20})		72	1.0 M KOH	[25]
Co_3B	GC	350 (η_{20})			1.0 M KOH	[26]
CoB pellet	-		-251	75	0.5 M KPi	[27]
CoB	GC		-203	79	0.5 M KPi	[28]
CoB	GC	344 (η_{20})		72	1.0 M KOH	[25]
CoB/C	GC	320		75	1.0 M KOH	[29]
CoB nanosheets	NF	265 (η_{20})		56	1.0 M KOH	[30]
CoB/NCNT		370		-	0.1 M KOH	[31]
CoB	Ni	140	-70	89/68	1.0 M KOH	[31]
Co-B@Co-Bi	GC	291		105	1.0 M KOH	[32]
CoB	GC	348		111	1.0 M KOH	[32]
Ni_3B-rGO films	CFP	290		88	1.0 M KOH	[33]
Ni_3B	CFP	340		81	1.0 M KOH	[33]
Ni_2B	GC	350		58	1.0 M KOH	[34]
NiB	GC		-132 (η_{20})	53, 112	1.0 M $HClO_4$	[35]
NiB	GC		-194 (η_{20})		1.0 M KOH	[35]
NiB	GC		-309	186	0.5 M KPi	[28]
Ni_2B/g-C_3N_4	GC		-707	221	1.0 M KOH	[36]
Ni-B@Ni-Bi	GC	310		150	1.0 M KOH	[32]
NiB	GC	365		100	1.0 M KOH	[32]
NiB	GC	331 (η_{20})		52	1.0 M KOH	[25]

50% C_{wax} = 50% graphite/50% paraffine wax, 45% C_{wax} = 45% graphite/55% paraffin wax, GC = glassy carbon, CP = carbon paper, CS = carbon sheet, FTO = fluorinated tin oxide glass, CFP = carbon fiber paper, NF = nickel foam *Approximate values due to pre-oxidation peaks having overlap with OER onset.

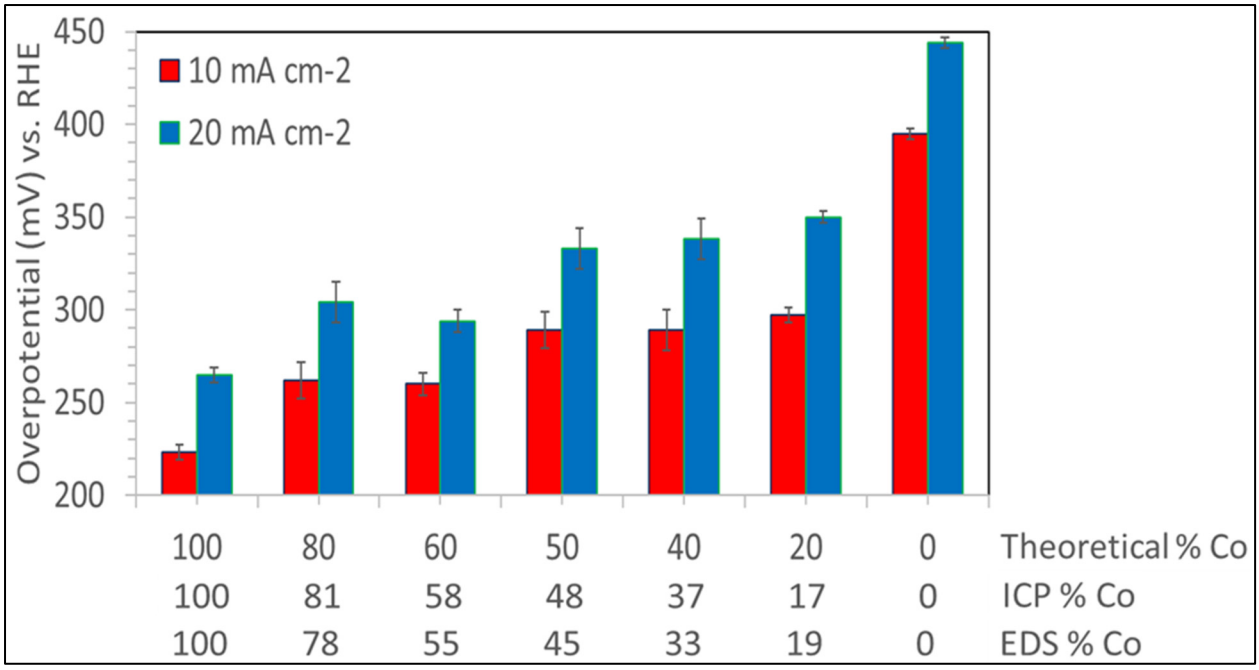

Figure S12. Graph of HER overpotentials at 10 mA cm^{-2} and 20 mA cm^{-2} current densities versus % Co (theoretical, ICP, and EDS).

Table S8. Literature comparison table for crystalline and amorphous ternary metal boride OER and HER activity in different electrolytes. All current densities are normalized for the geometric electrode area. The η_{10} overpotentials are calculated versus the ideal equilibrium 0 V and 1.23 V potentials for HER and OER water splitting.

MB	Crystalline/ amorphous	Electrode	OER (η_{10} mV)	HER (η_{10} mV)	Tafel slope (mV/dec) OER/HER	Electrolyte	Ref.
CoB $Co_{0.8}Fe_{0.2}B$ $Co_{0.6}Fe_{0.4}B$ $Co_{0.5}Fe_{0.5}B$ $Co_{0.4}Fe_{0.6}B$ $Co_{0.2}Fe_{0.8}B$ FeB	Cry	50% C_{wax}	345 351 340 338 353 403 456	223 262 288 289 289 297 392	95/105 66/139 79/163 103/150 87/160 78/177 52/169	1.0 M KOH	This study
Co_2MoB_4 Fe_2MoB_4	Cry	C_{cloth}	283 463	-	19.9 95.5	1.0 M KOH	[37]
Activated $FeCoB_2$	Cry	GCE	295	-	~84	1.0 M KOH	[38]
CoFeB CoB FeB	amor	NF	270 (η_{50}) 296 (η_{50}) 343 (η_{50})	-	36 109 68	1.0 M KOH	[39]
CoFeB CoB	Cry	GE	328 313	-	78.9 75.7	1.0 M KOH	[40]
NiFe-boride	amor	NF	167	-	25	1.0 M KOH	[41]
Co-Fe-B Co3-Fe-B Co-Fe3-B CoB FeB	Cry	-	280 330 360 400 450	129 194 201 212 267	38.9/67.3 65.4/94.6 66.7/79.5 65.9/86.8 58.4/99.9	1.0 M KOH	[42]
Fe_3Co_7B/CNT Fe_3Co_7B CoB/CNT FeB/CNT	Amor	GC	265 282 338 347	-	30 34 73 52	1.0 M KOH	[43]
$AlFe_2B_2$	Cry	NF	240	-	42	1.0 M KOH	[44]
NiCoFeB NiCoB CoB	Amor	GC	284 375 383	345 363 396	47/98 78.1/102 79/119	1.0 M KOH	[45]
CoNiB/CC	Amor	CC	-	80	88.2	1.0 M KOH	[46]
Co-3MoB	Amor	GC	96 66	- 320	56 155/67	KPi (pH 7) 1.0 M NaOH (pH 14)	[47]
Co2-Fe-B Co_2B Fe_2B	Amor	Cu sheet	298 340 472	-	62.6 97.3 81.6	1.0 M KOH	[48]

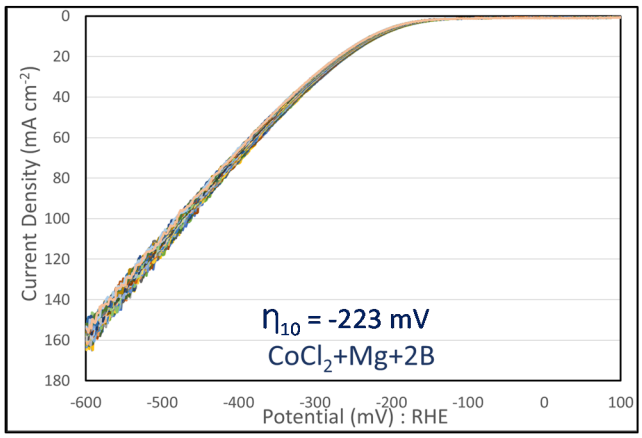
Current Density (mA cm-2)
Potential (mV) : RHE
η10 = -223 mV
CoCl2+Mg+2B

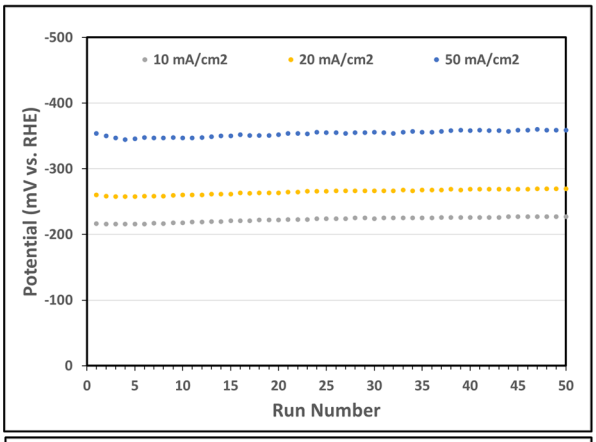
10 mA/cm2
20 mA/cm2
50 mA/cm2
Potential (mV vs. RHE)
Run Number

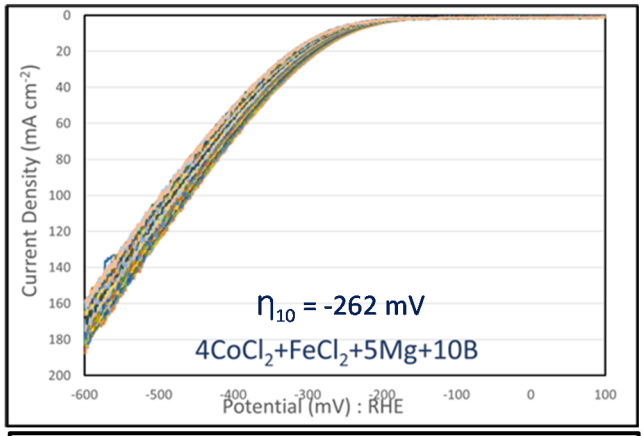
Current Density (mA cm-2)
Potential (mV) : RHE
η10 = -262 mV
4CoCl2+FeCl2+5Mg+10B

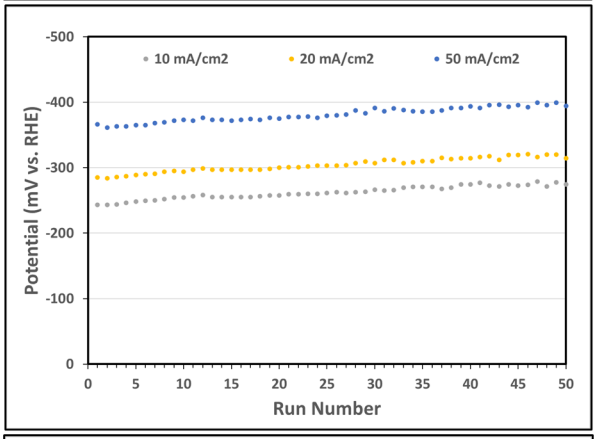
10 mA/cm2
20 mA/cm2
50 mA/cm2
Potential (mV vs. RHE)
Run Number

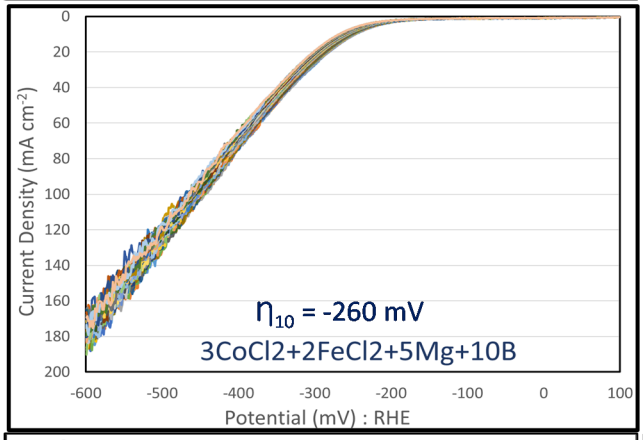
Current Density (mA cm-2)
Potential (mV) : RHE
η10 = -260 mV
3CoCl2+2FeCl2+5Mg+10B

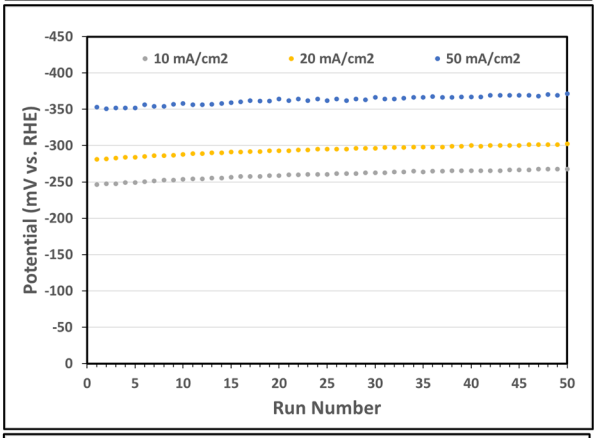
10 mA/cm2
20 mA/cm2
50 mA/cm2
Potential (mV vs. RHE)
Run Number

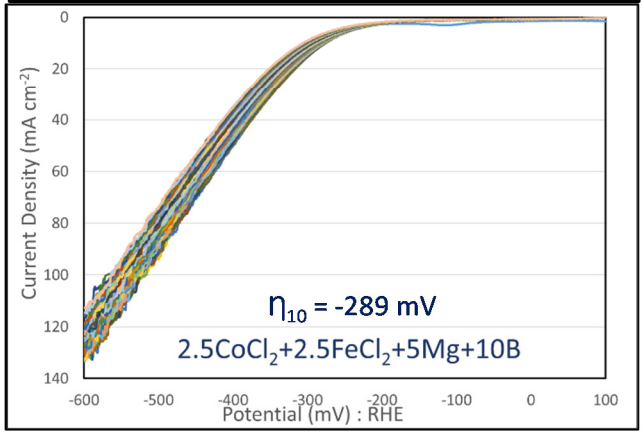
Current Density (mA cm-2)
Potential (mV) : RHE
η10 = -289 mV
2.5CoCl2+2.5FeCl2+5Mg+10B

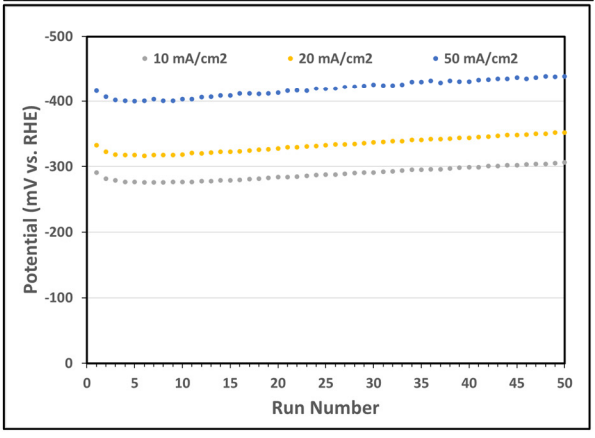
10 mA/cm2
20 mA/cm2
50 mA/cm2
Potential (mV vs. RHE)
Run Number

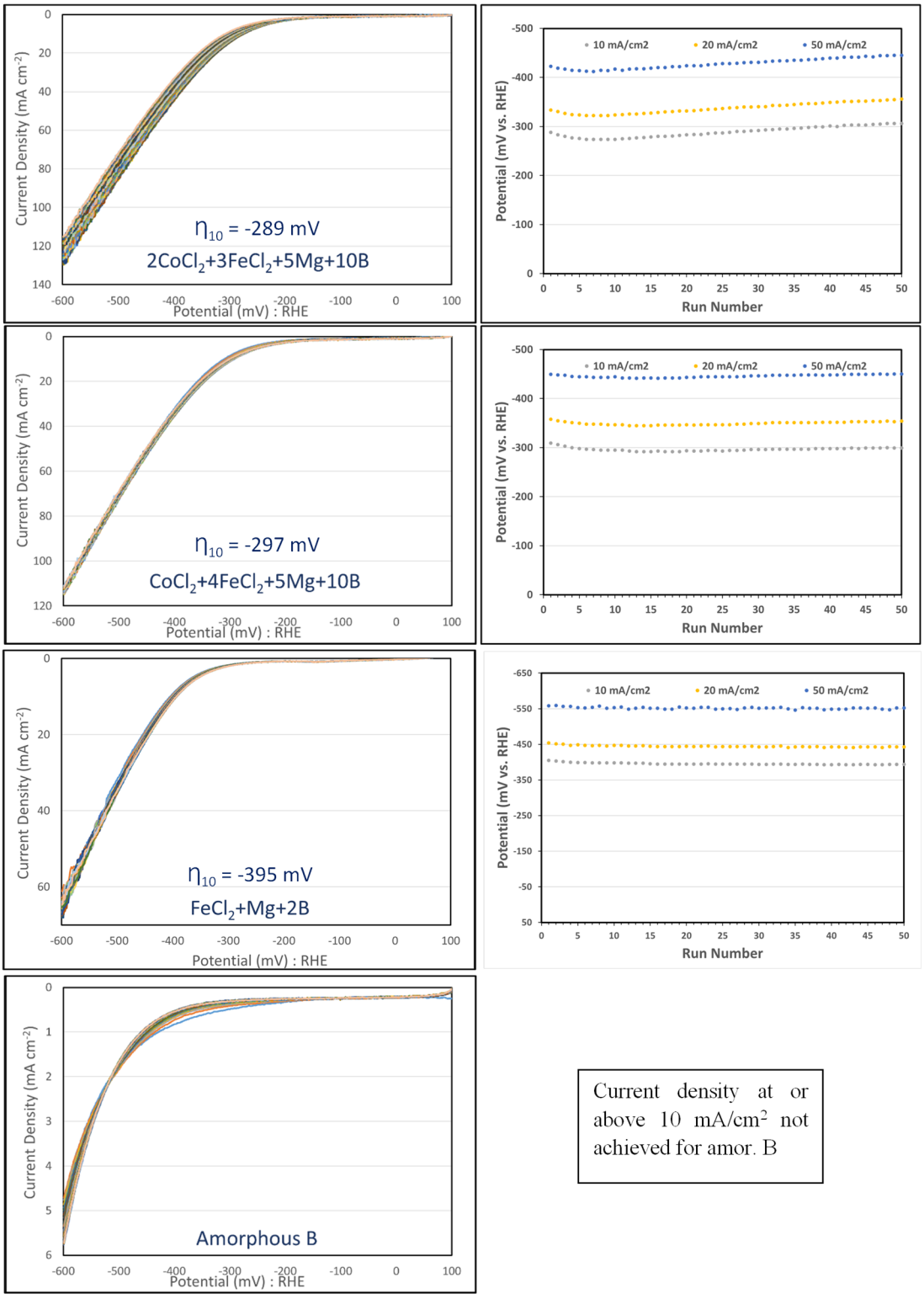

Figure S13. Left column: Overlay plots of 50 LSV scans of metal borides for HER in 1.0 M KOH at 5 mV s^{-1} scan rate. Right column: Plots of run number versus potentials at 10, 20, and 50 mA/cm^2 current densities extracted from left column overlay plots. Metal boride powders are embedded on C_{wax} working electrodes.

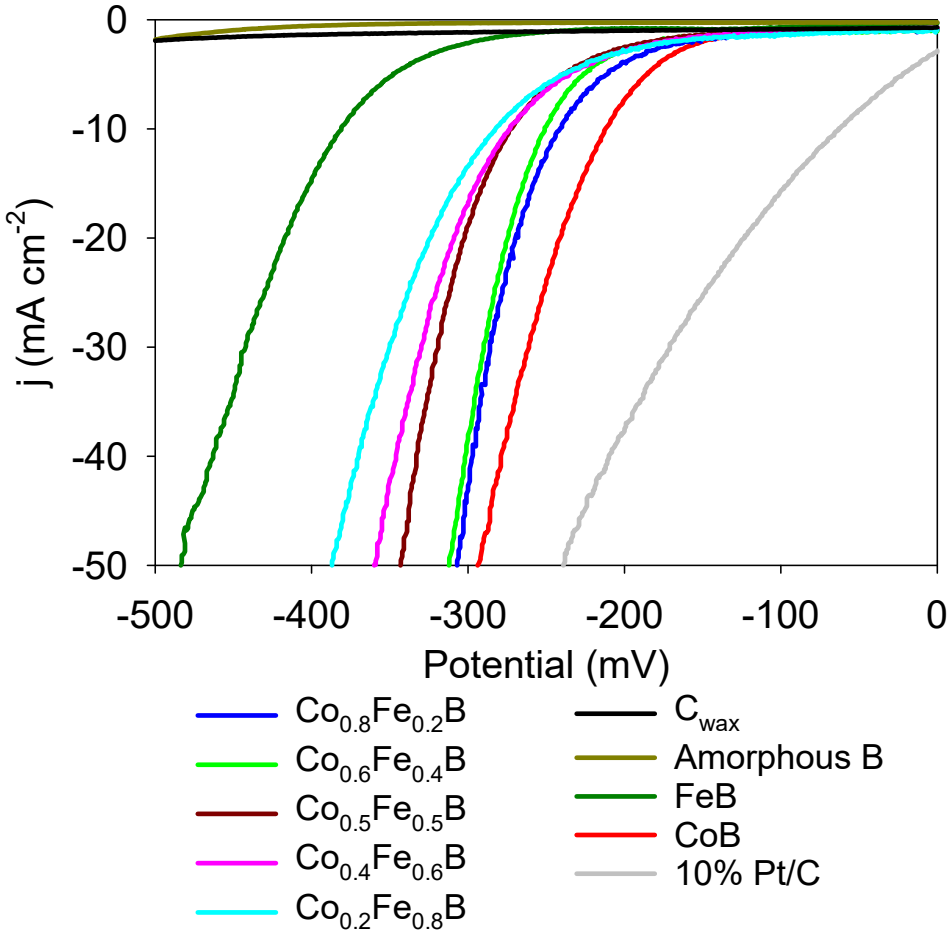

Figure S14. HER LSV overlay plots for metal borides with 85% iR compensation at 5 mV s^{-1} scan rate. A representative LSV run from 10 LSVs with iR on is shown in the graph. The working electrodes are metal boride powders embedded on C_{wax} tips.

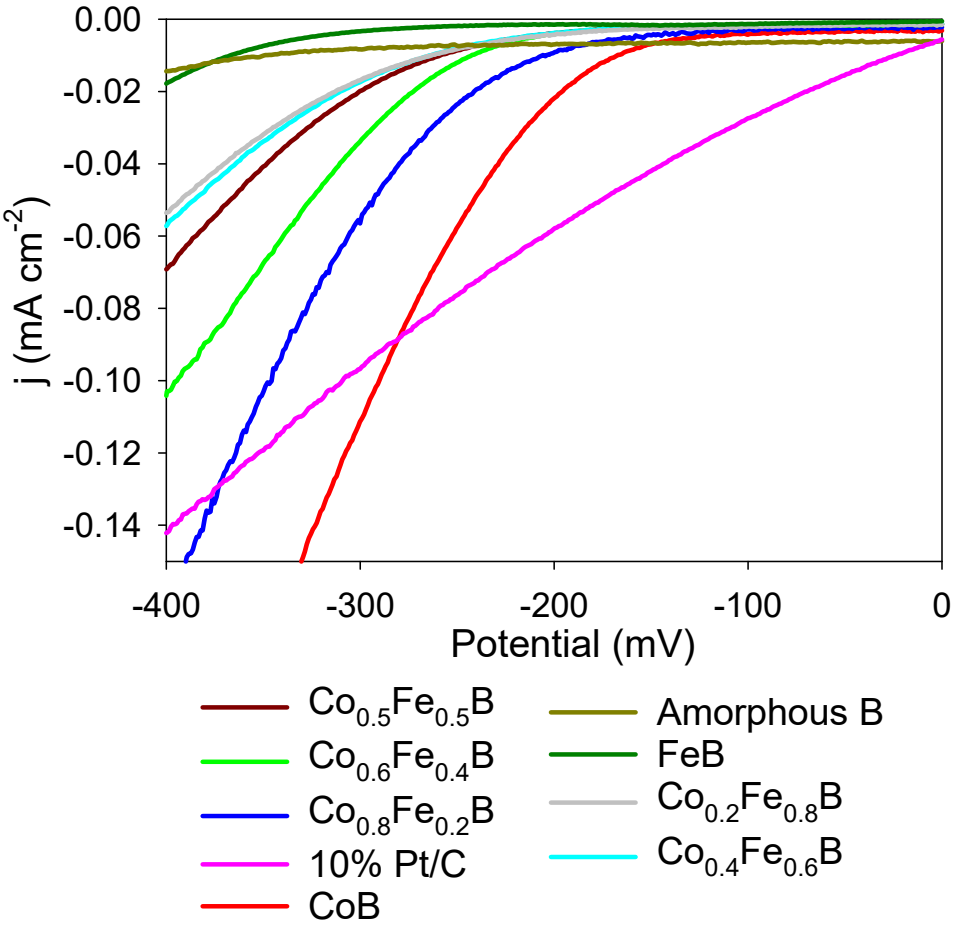

Figure S15. HER LSV overlay plots for metal borides and 10% Pt/C with ECSA normalized current densities in 1.0 M KOH.

Table S9. HER electrocatalysis of CoB + FeB physical mixing samples in 1.0 M KOH (average of 50 HERs were reported in the table).

Sample	(η_{10}) (mV)[1]	(η_{20}) (mV)	Tafel (mV dec^{-1})	ECSA (cm^2)
CoB	-223 ± 4	-265 ± 4	-105	22
4 CoB + FeB	-293 ± 1	-355 ± 1	-121	23
3 CoB + 2 FeB	-298 ± 1	-356 ± 2	-139	29
2.5 CoB + 2.5 FeB	-305 ± 1	-372 ± 2	-148	54
2 CoB + 3 FeB	-313 ± 2	-378 ± 2	-153	35
CoB + 4 FeB	-364 ± 5	-430 ± 6	-155	31
FeB	-395 ± 3	-444 ± 3	-136	43

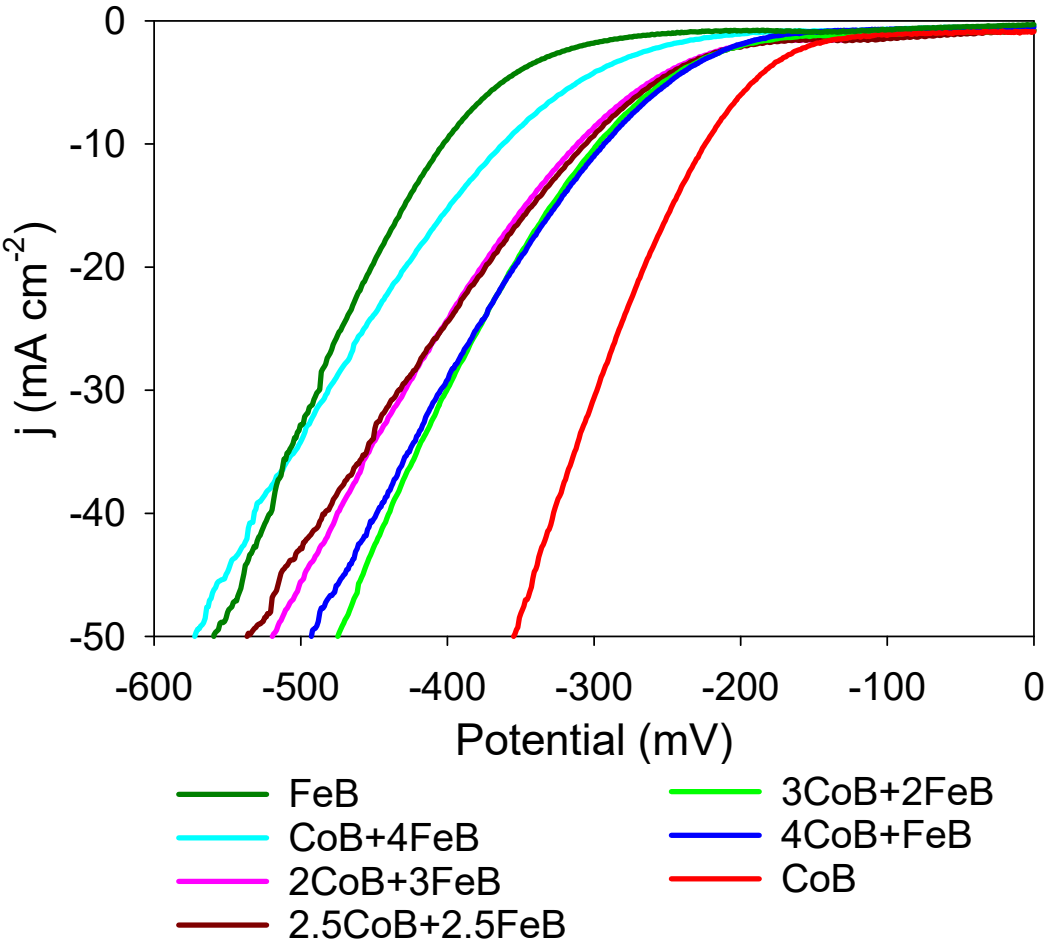

Figure S16. Representative HER LSV results of physically mixed (hand-grinding in a mortar and pestle) CoB + FeB mixtures. Data was obtained using 1.0 M KOH in a three-electrode cell at 5 mV/s scan rate with Hg/HgO reference and graphite rod counter electrodes. Current densities are scaled using the geometric electrode area (0.08 cm^2).

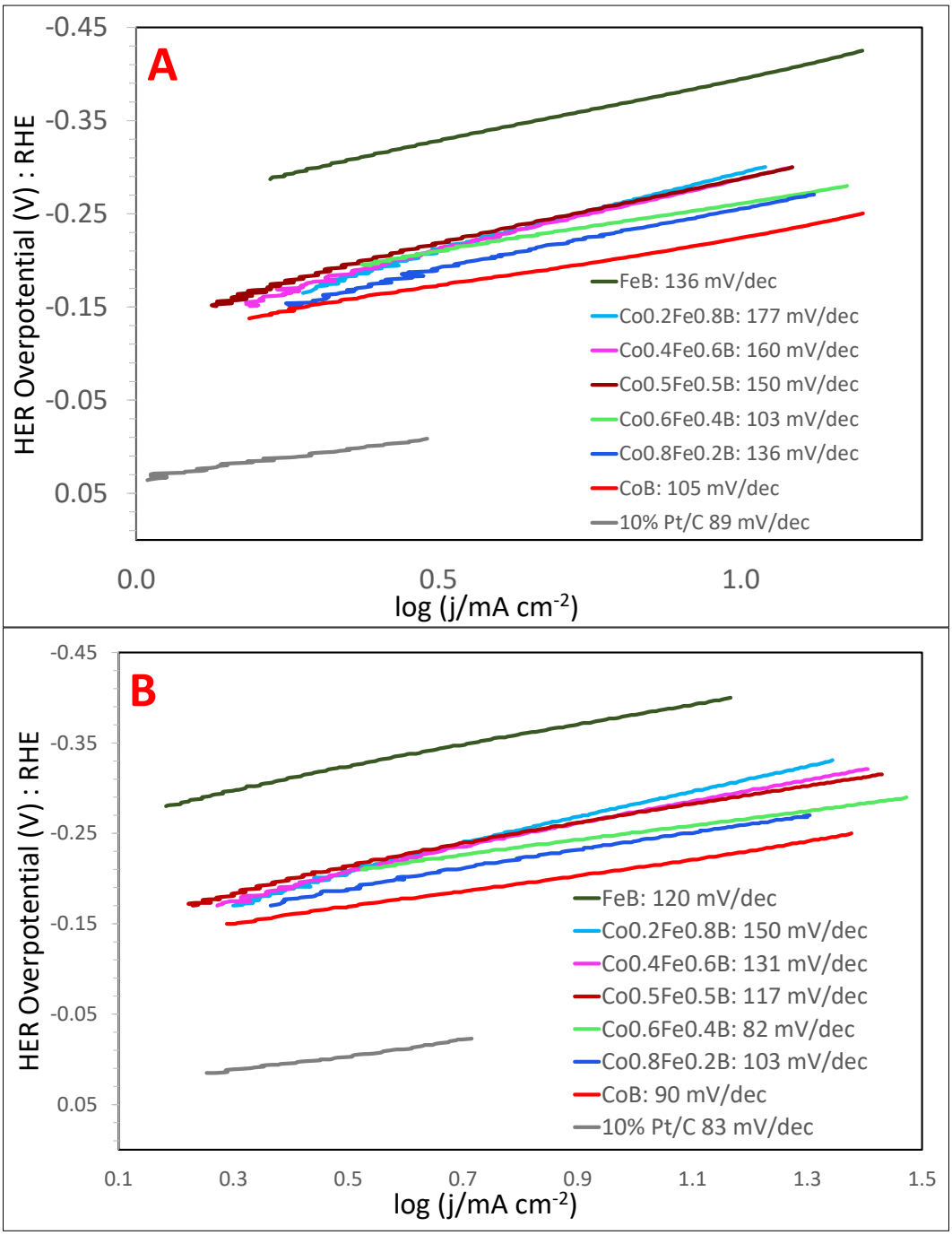

Figure S17. The Tafel slopes of metal borides and 10% Pt/C representative HER LSV runs in 1.0 M KOH. **A**. without iR correction, **B**. with 85% iR correction.

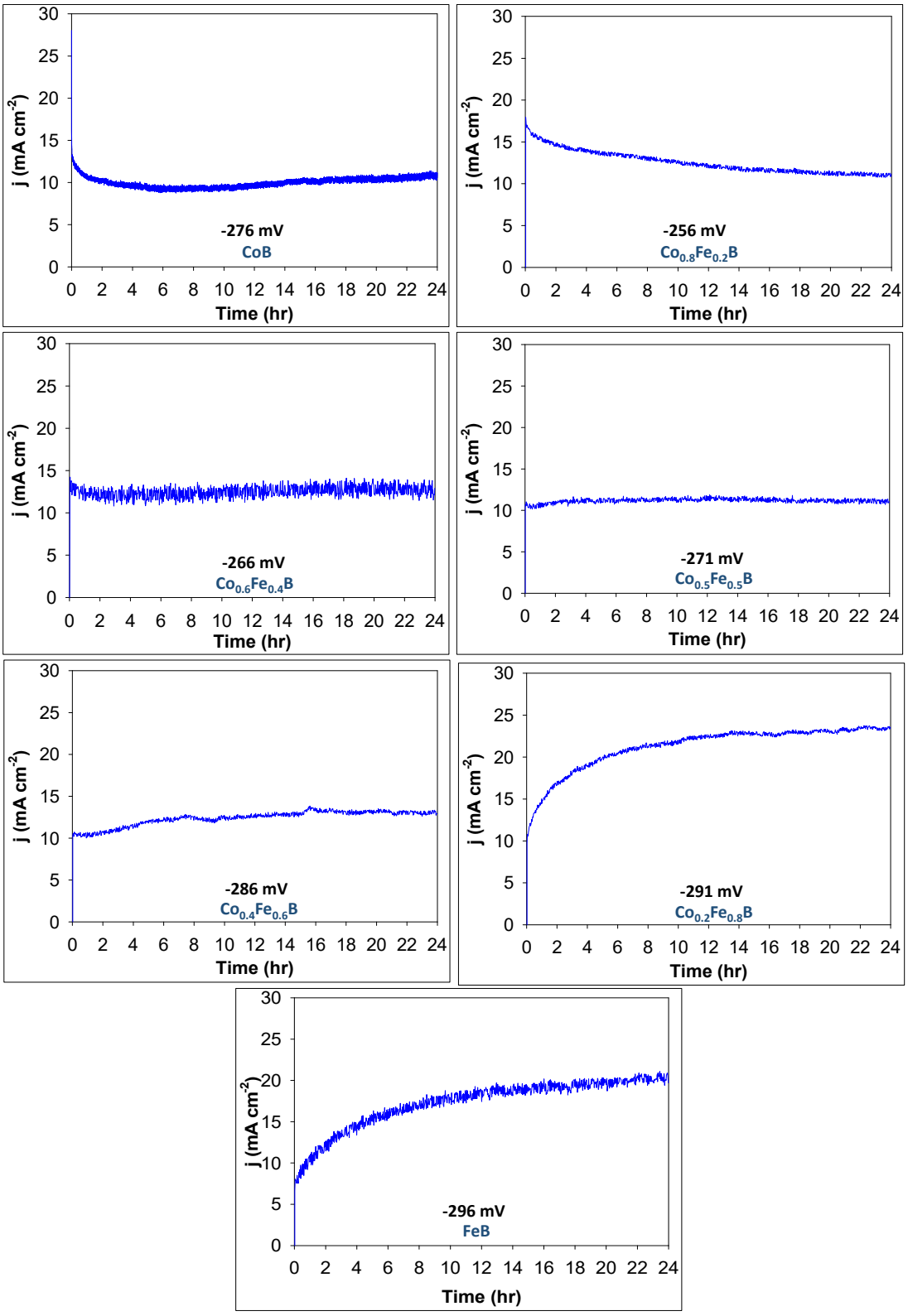

Figure S18. Applied negative potential HER chronoamperometry data (current versus time at constant potential) for metal borides in 1.0 M KOH for 24 hrs. The potentials used are indicated and were chosen to ideally sustain 10 mA cm^{-2}. The working electrodes are metal boride powders embedded on C_{wax} tips.

Table S10. Summary of post-chronoamperometry HER electrocatalysis of SSM synthesized metal borides in 1.0 M KOH (average of 10 HERs were reported in the table) (manually corrected 85% iR compensation results in parentheses).

Sample	(η_{10}) (mV)[1]	(η_{20}) (mV)	Tafel (mV dec^{-1})
CoB	-255 ± 2 (-240 ± 2)	-303 ± 2 (-273 ± 2)	-121 (-103)
$Co_{0.8}Fe_{0.2}B$	-230 ± 6 (-217 ± 6)	-279 ± 4 (-252 ± 4)	-134 (-110)
$Co_{0.6}Fe_{0.4}B$	-264 ± 5 (-254 ± 5)	-303 ± 4 (-282 ± 4)	-119 (-100)
$Co_{0.5}Fe_{0.5}B$	-287 ± 10 (-266 ± 10)	-343 ± 10 (-299 ± 10)	-162 (-138)
$Co_{0.4}Fe_{0.6}B$	-267 ± 8 (-237 ± 8)	-326 ± 8 (-266 ± 8)	-161 (-130)
$Co_{0.2}Fe_{0.8}B$	-275 ± 3 (-257 ± 3)	-335 ± 3 (-298 ± 3)	-170 (-146)
FeB	-324 ± 10 (-306 ± 10)	-382 ± 9 (-346 ± 9)	-169 (-149)

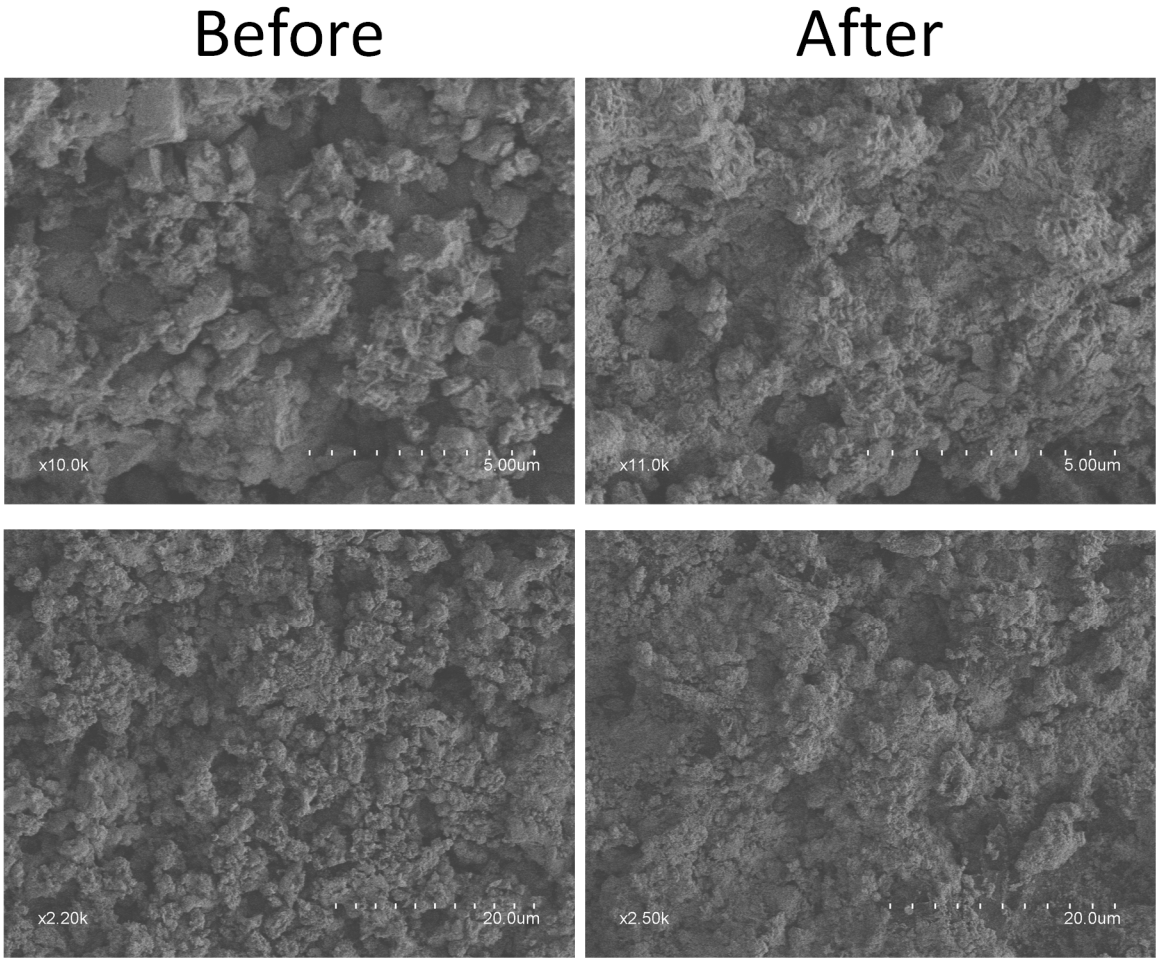

Figure S19. SEM surface comparison of FeB electrodes before (left) and after (right) HER electrochemistry measurements. Top two images are high-magnification (5 μm) and bottom two images are low-magnification (20 μm) images.

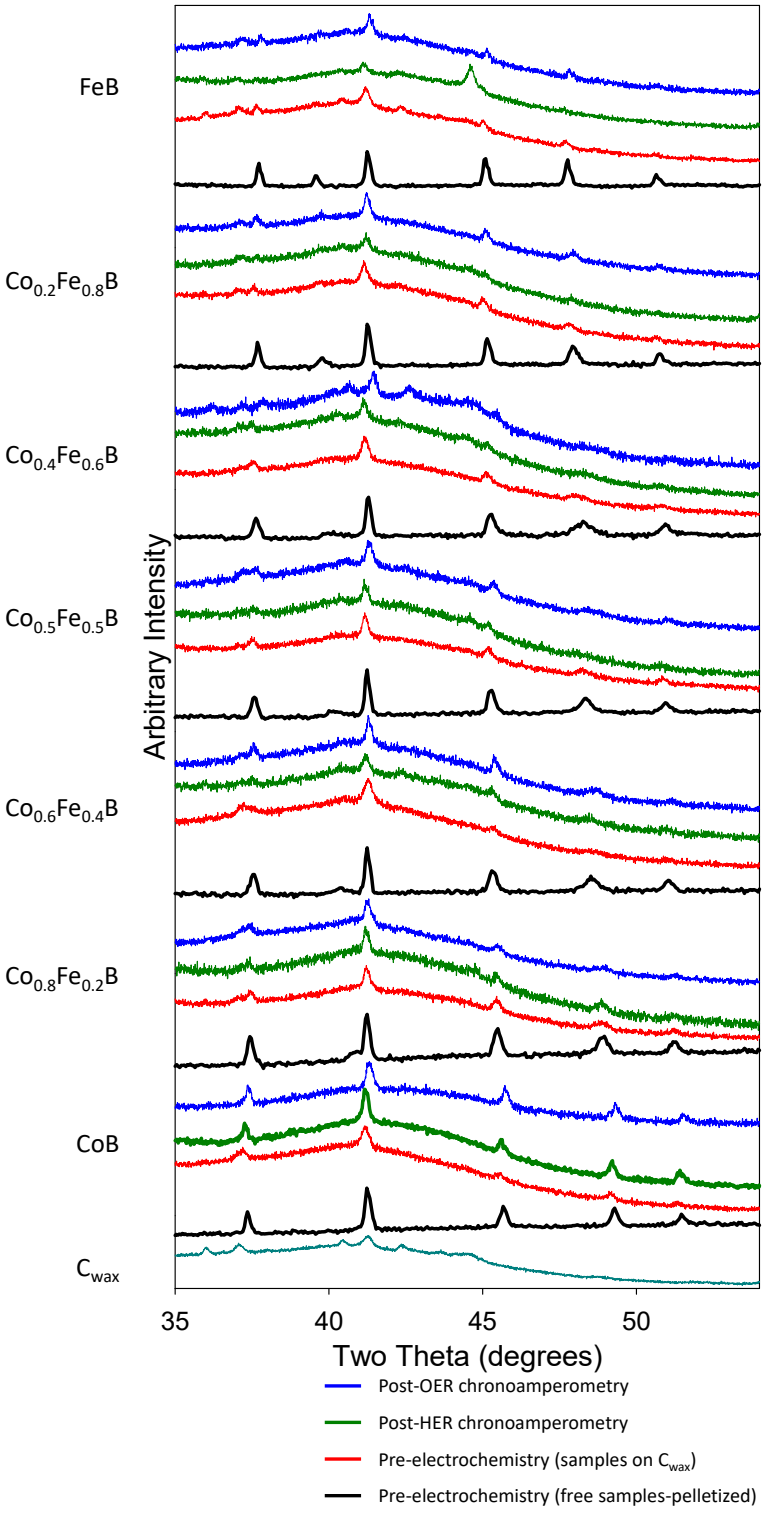

Figure S20. Powder XRD results of pre- and post-positive potential OER chronoamperometry (red and blue diffractograms) and post-negative potential HER chronoamperometry (green diffractograms) of powders on C_{wax} tips for CoB, FeB, and $Co_{1-x}Fe_xB$ solid-solutions. Metal borides pelletized free sample XRDs (black diffractograms), and diffractogram of C_{wax} are also shown for the comparison. The C_{wax} electrode has several broad XRD peaks that are a combination of graphite and paraffin wax diffraction.

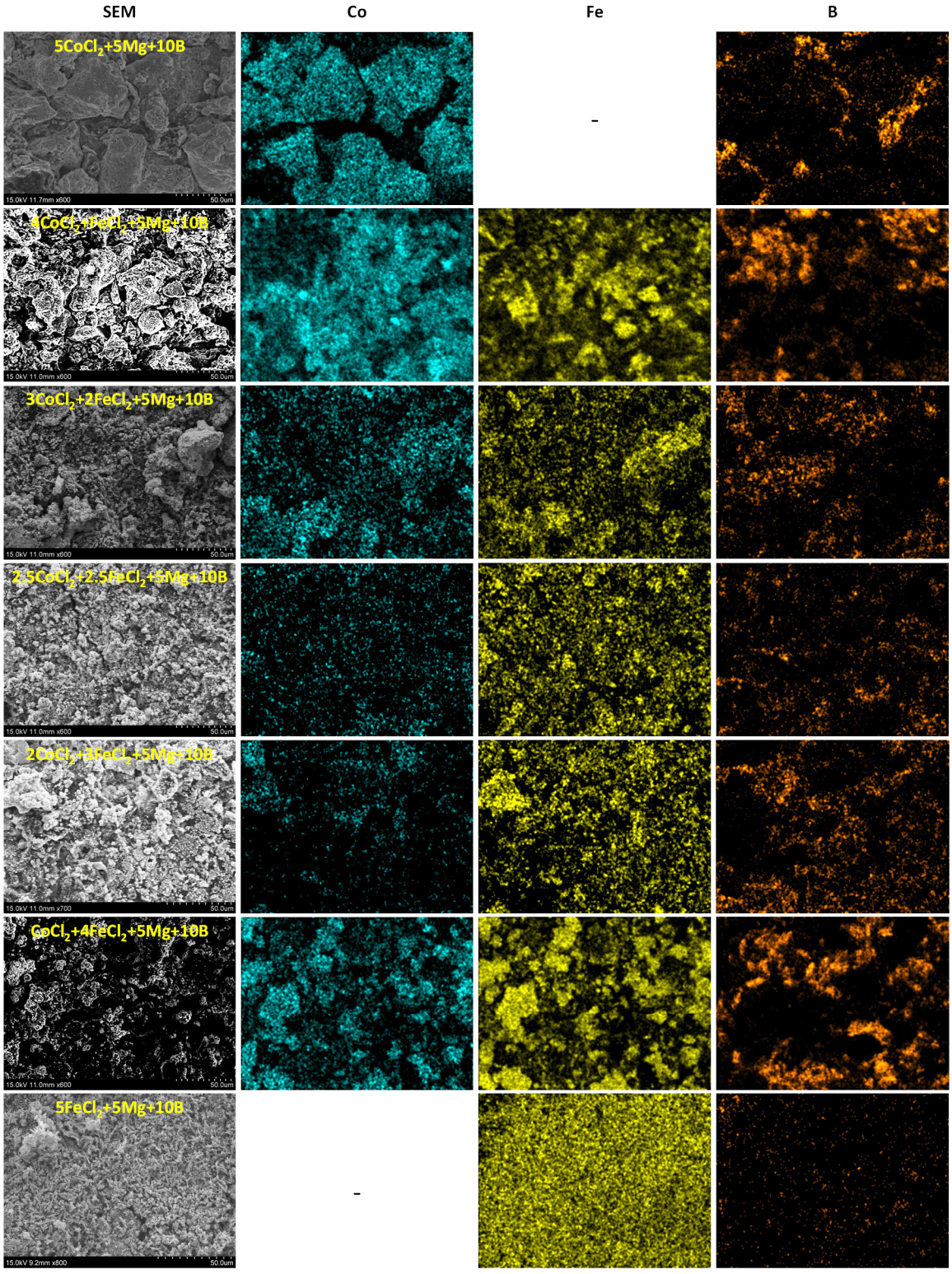

Figure S21. Post-negative potential HER chronoamperometry EDS maps of CoB, FeB, and $Co_{1-x}Fe_xB$ solid-solutions. Images are from powders embedded on C_{wax} tip.

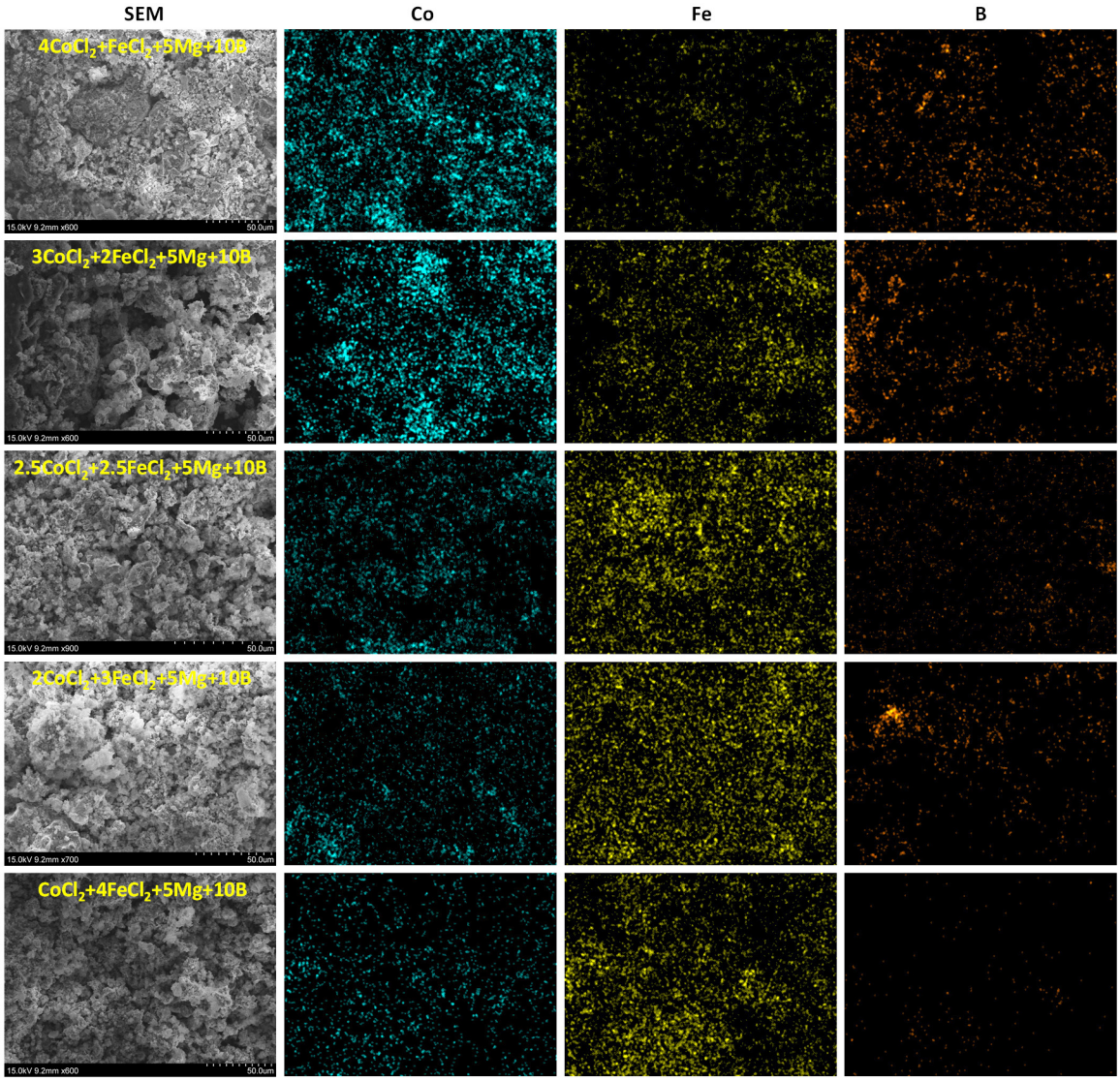

Figure S22. EDS maps of CoB, FeB, and $Co_{1-x}Fe_xB$ solid-solutions on C_{wax} tips before electrochemistry measurements (pre-electrochemistry). Images are from powders embedded on C_{wax} tip.

Table S11. EDS Co/Fe ratios of $Co_{1-x}Fe_xB$ solid-solutions before and after electrochemistry measurements.

Sample	Before electrochemistry (free powder pelletized)	Before electrochemistry (on C_{wax})	After electrochemistry (HER)	After electrochemistry (OER)
	Co/Fe ratio	Co/Fe ratio	Co/Fe ratio	Co/Fe ratio
$4CoCl_2$+$FeCl_2$	78/22	78/22	62/38	78/22
$3CoCl_2$+$2FeCl_2$	55/45	57/43	57/43	63/37
$2.5CoCl_2$+$2.5FeCl_2$	45/55	50/50	32/68	51/49
$2CoCl_2$+$3FeCl_2$	33/67	34/66	23/77	36/64
$CoCl_2$+$4FeCl_2$	19/81	19/81	16/84	23/77

EDS of fresh metal borides as pelletized free powder form or pressed and embedded on C_{wax} electrode tips were used as before electrochemistry EDS samples. EDS of metal borides on C_{wax} after electrochemistry was obtained after initial 50 HERs or 56 OERs, 24-hour chronoamperometry run, and post 10 LSV runs.

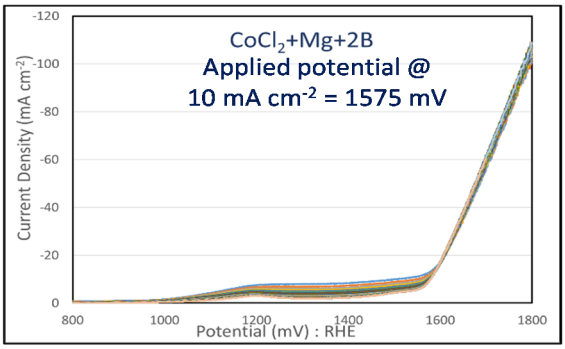
$CoCl_2$+Mg+2B
Applied potential @
10 mA cm^{-2} = 1575 mV
Current Density (mA cm^{-2})
Potential (mV) : RHE

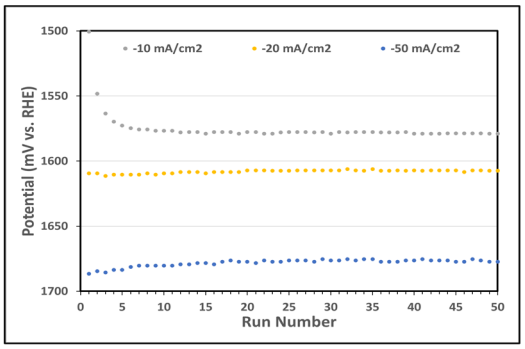
-10 mA/cm2
-20 mA/cm2
-50 mA/cm2
Potential (mV vs. RHE)
Run Number

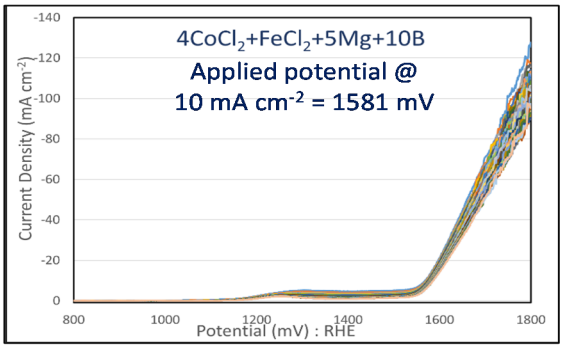
$4CoCl_2$+$FeCl_2$+5Mg+10B
Applied potential @
10 mA cm^{-2} = 1581 mV
Current Density (mA cm^{-2})
Potential (mV) : RHE

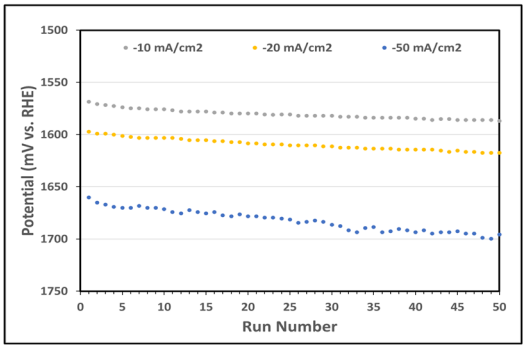
-10 mA/cm2
-20 mA/cm2
-50 mA/cm2
Potential (mV vs. RHE)
Run Number

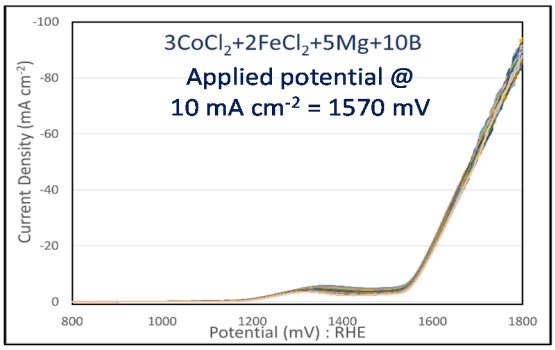
$3CoCl_2$+$2FeCl_2$+5Mg+10B
Applied potential @
10 mA cm^{-2} = 1570 mV
Current Density (mA cm^{-2})
Potential (mV) : RHE

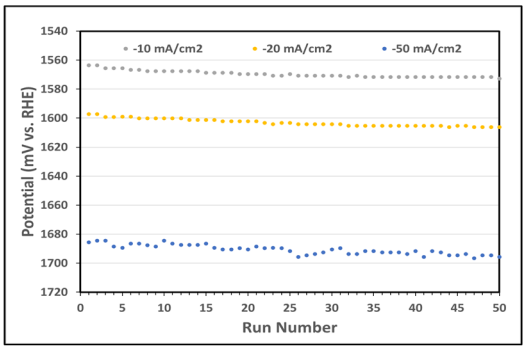
-10 mA/cm2
-20 mA/cm2
-50 mA/cm2
Potential (mV vs. RHE)
Run Number

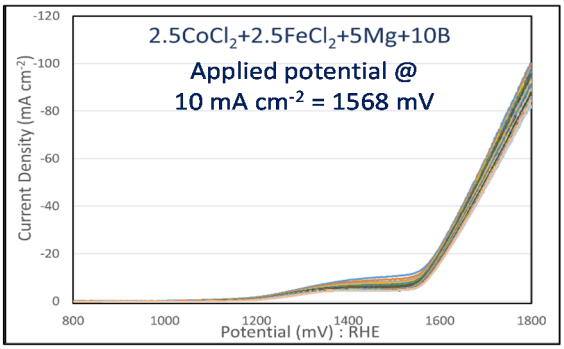
$2.5CoCl_2$+$2.5FeCl_2$+5Mg+10B
Applied potential @
10 mA cm^{-2} = 1568 mV
Current Density (mA cm^{-2})
Potential (mV) : RHE

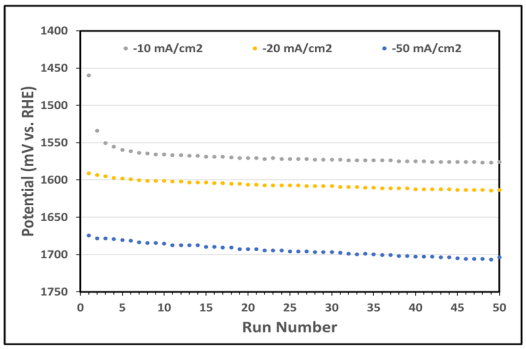
-10 mA/cm2
-20 mA/cm2
-50 mA/cm2
Potential (mV vs. RHE)
Run Number

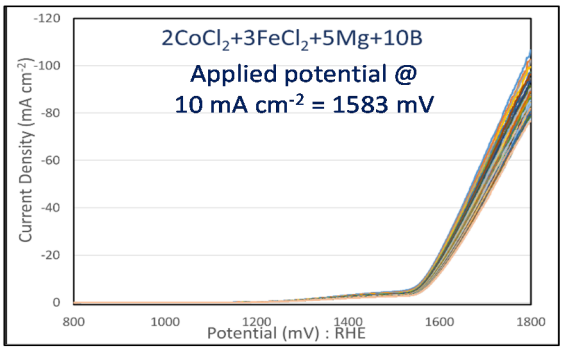
$2CoCl_2$+$3FeCl_2$+5Mg+10B
Applied potential @
10 mA cm^{-2} = 1583 mV
Current Density (mA cm^{-2})
Potential (mV) : RHE

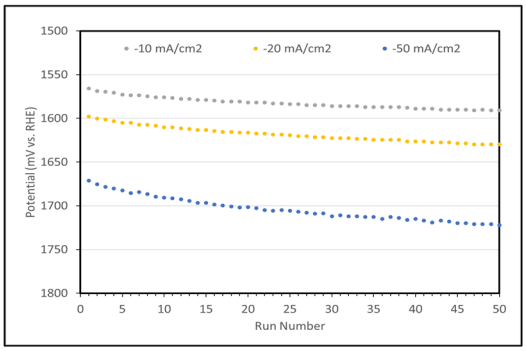
-10 mA/cm2
-20 mA/cm2
-50 mA/cm2
Potential (mV vs. RHE)
Run Number

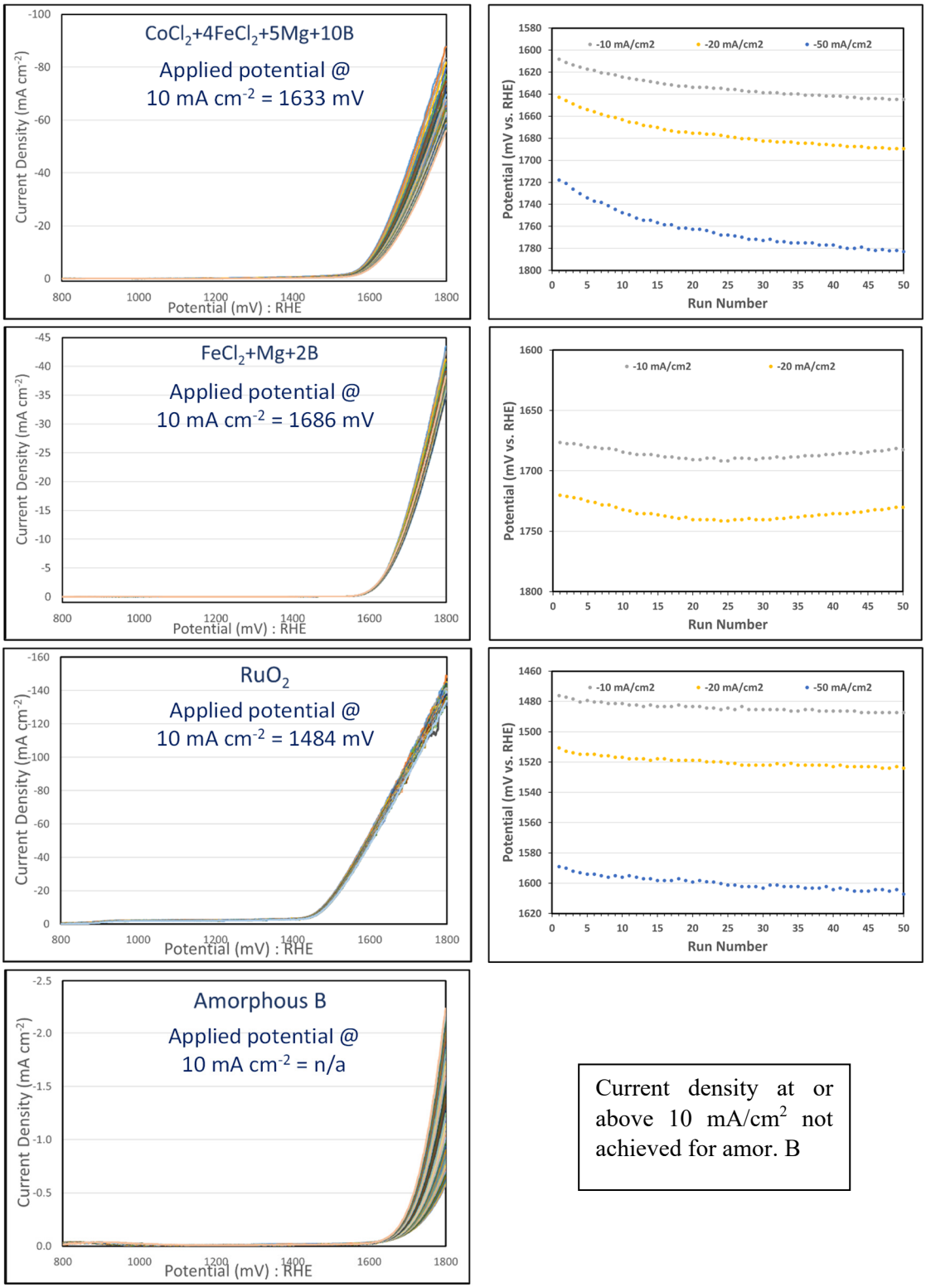

Current density at or above 10 mA/cm^2 not achieved for amor. B

Figure S23. Left column: Overlay plots of 50 LSV runs of CoB, FeB, $Co_{1-x}Fe_xB$, RuO_2, and B for OER experiments in 1.0 M KOH at 5 mV s^{-1} scan rate. Right column: Plots of run number versus potentials at 10, 20 and 50 mA/cm^2 current densities extracted from left column overlay plots. The working electrodes are metal boride powders embedded on C_{wax} tips.

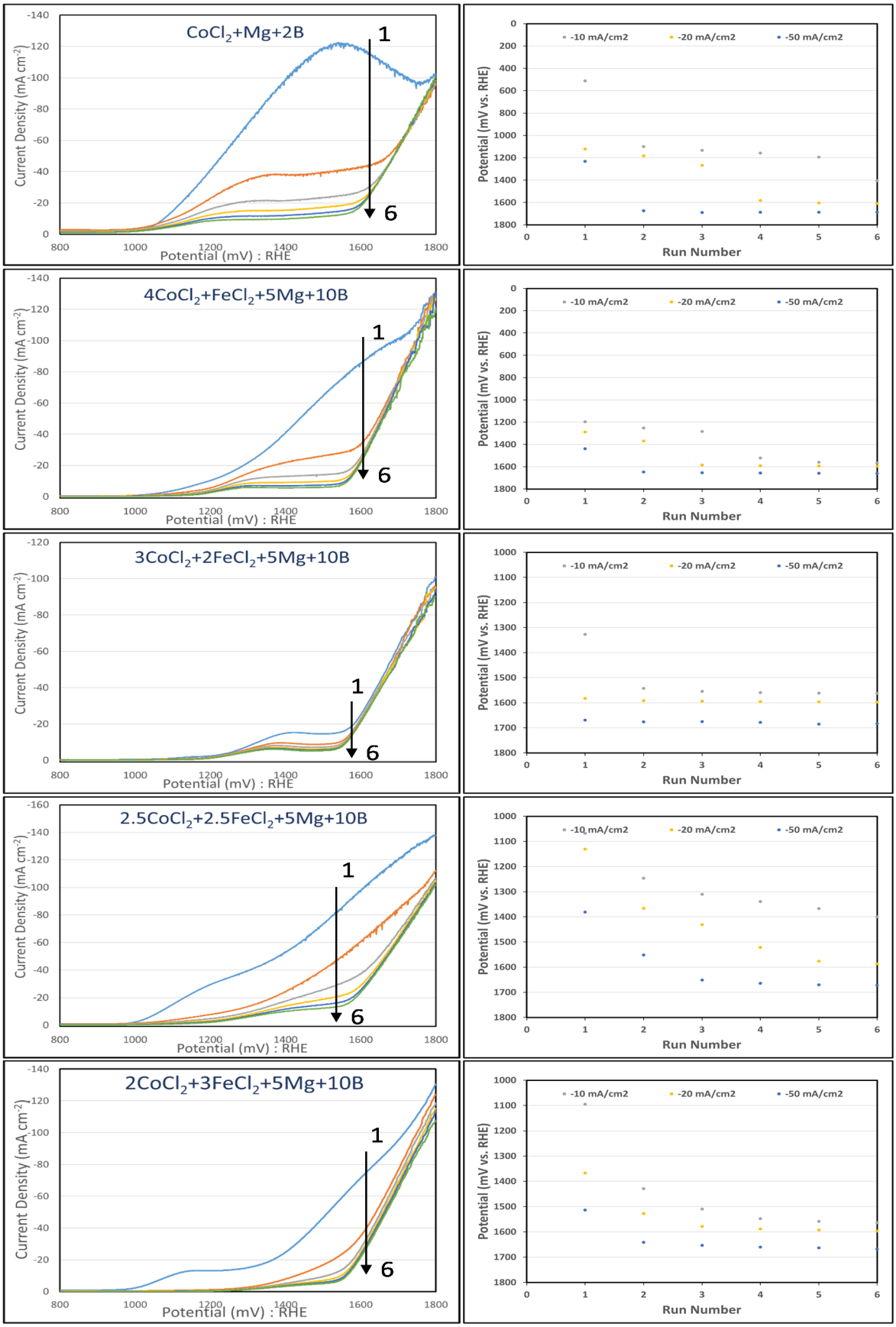
CoCl2+Mg+2B
4CoCl2+FeCl2+5Mg+10B
3CoCl2+2FeCl2+5Mg+10B
2.5CoCl2+2.5FeCl2+5Mg+10B
2CoCl2+3FeCl2+5Mg+10B
Current Density (mA cm-2)
Potential (mV) : RHE
Potential (mV vs. RHE)
Run Number
-10 mA/cm2
-20 mA/cm2
-50 mA/cm2
1
6

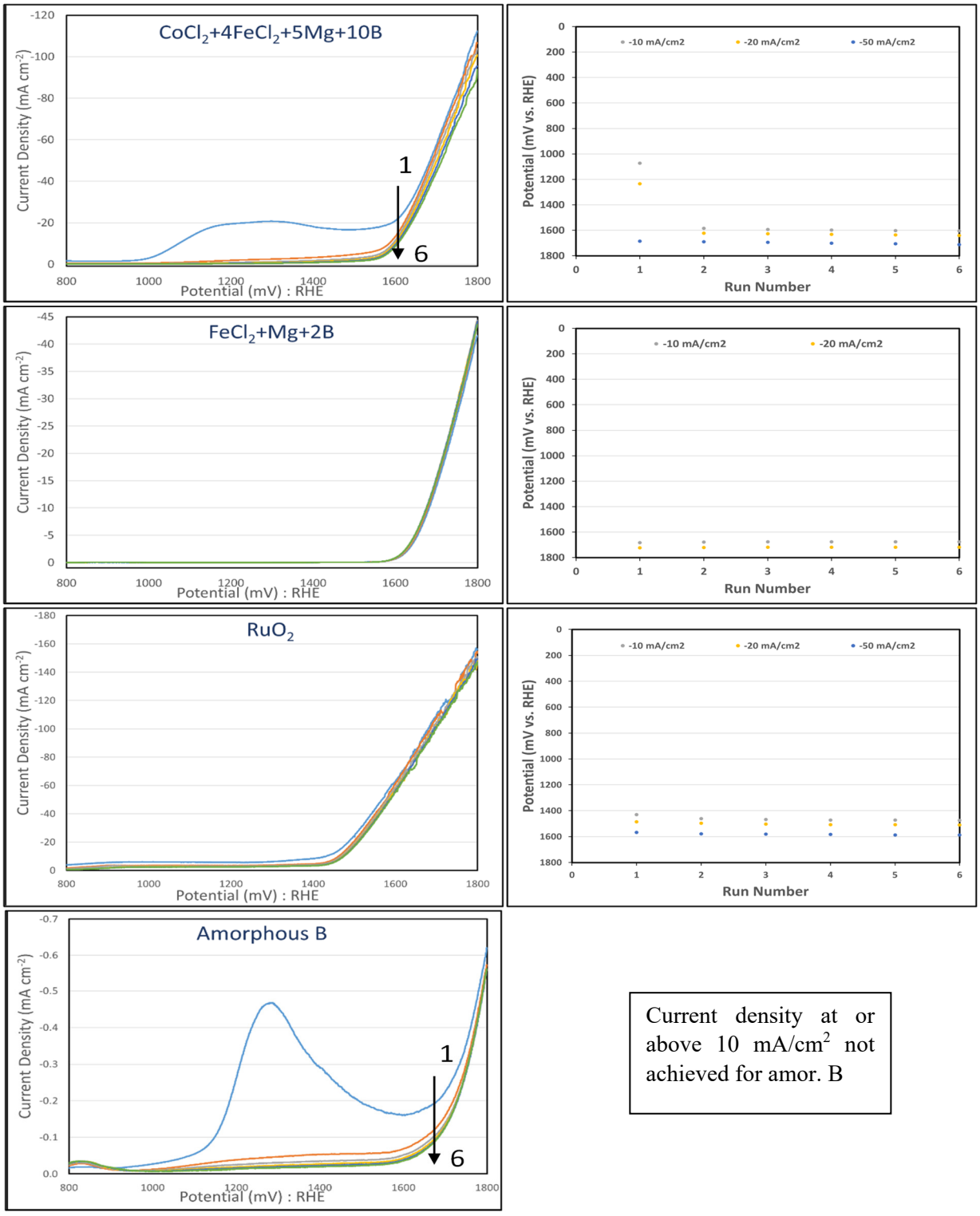

Figure S24. First six OER conditioning runs overlay plots and their corresponding potential versus run number plots in 1.0 M KOH at 5 mV s^{-1} scan rate. The working electrodes are metal boride powders embedded on C_{wax} tips. It is obvious that CoB and $Co_{1-x}Fe_xB$ solid solutions' OER active stable surfaces formed after surface modifications of conditioning runs. LSV curves moved from run 1 to run 6 as represented by the arrow.

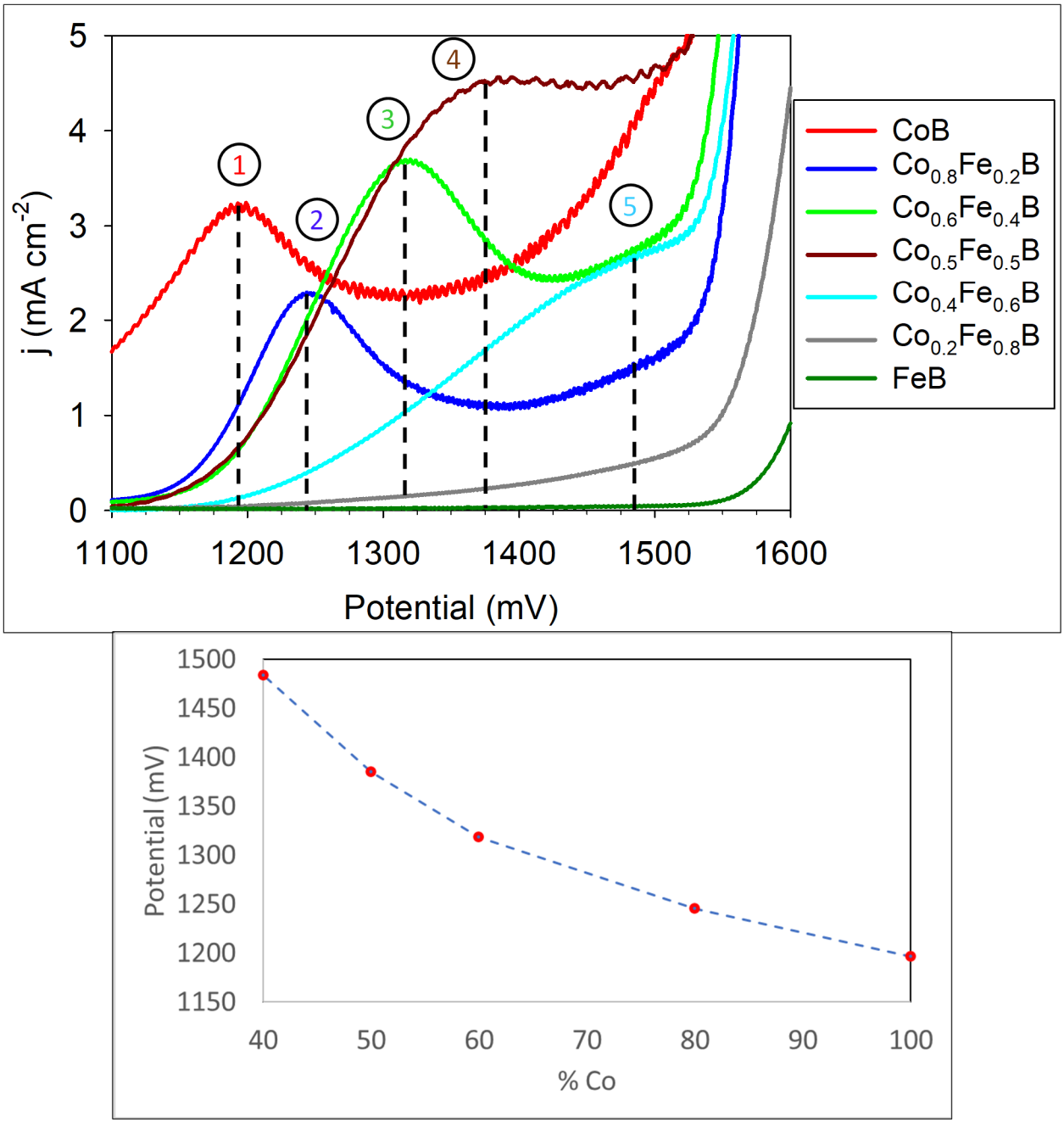

Figure S25. Top: Additional oxidation peak in CoB and $Co_{1-x}Fe_xB$ samples formed around 1200-1500 mV potential range. Representative (25th run) data were obtained for the comparison. Peaks positions at 1196 mV (1), 1245 mV (2), 1318 mV (3), 1385 mV (4), and 1492 mV (5) for CoB, $Co_{0.8}Fe_{0.2}B$, $Co_{0.6}Fe_{0.4}B$, $Co_{0.5}Fe_{0.5}B$, $Co_{0.4}Fe_{0.6}B$ samples, respectively. Bottom: Graph of %Co versus peak potentials.

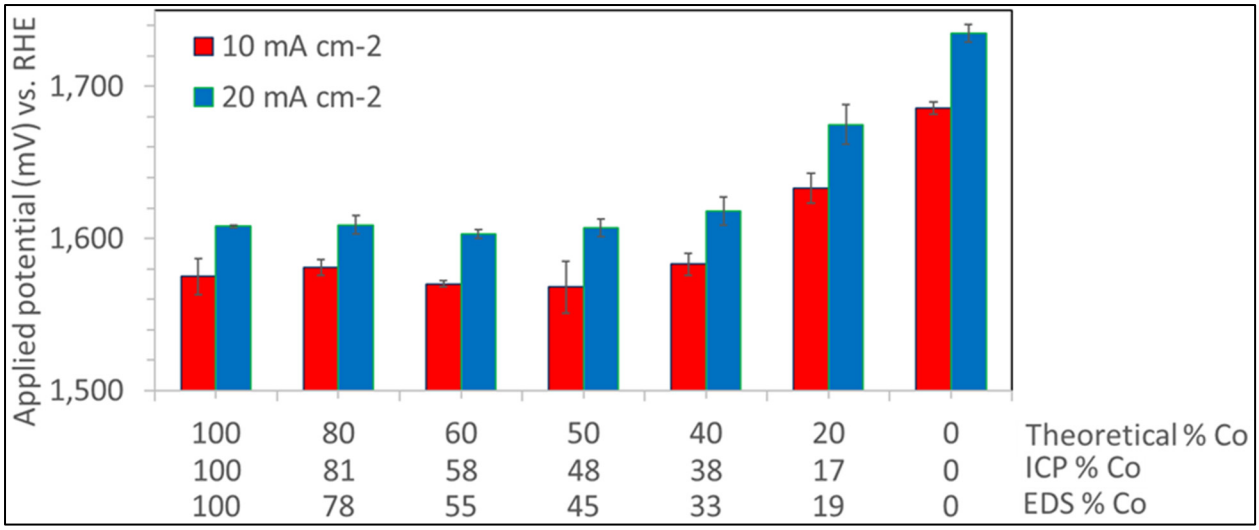

Figure S26. OER current density (10 mA cm^{-2} and 20 mA cm^{-2}) changes with % Co (theoretical, ICP, and EDS).

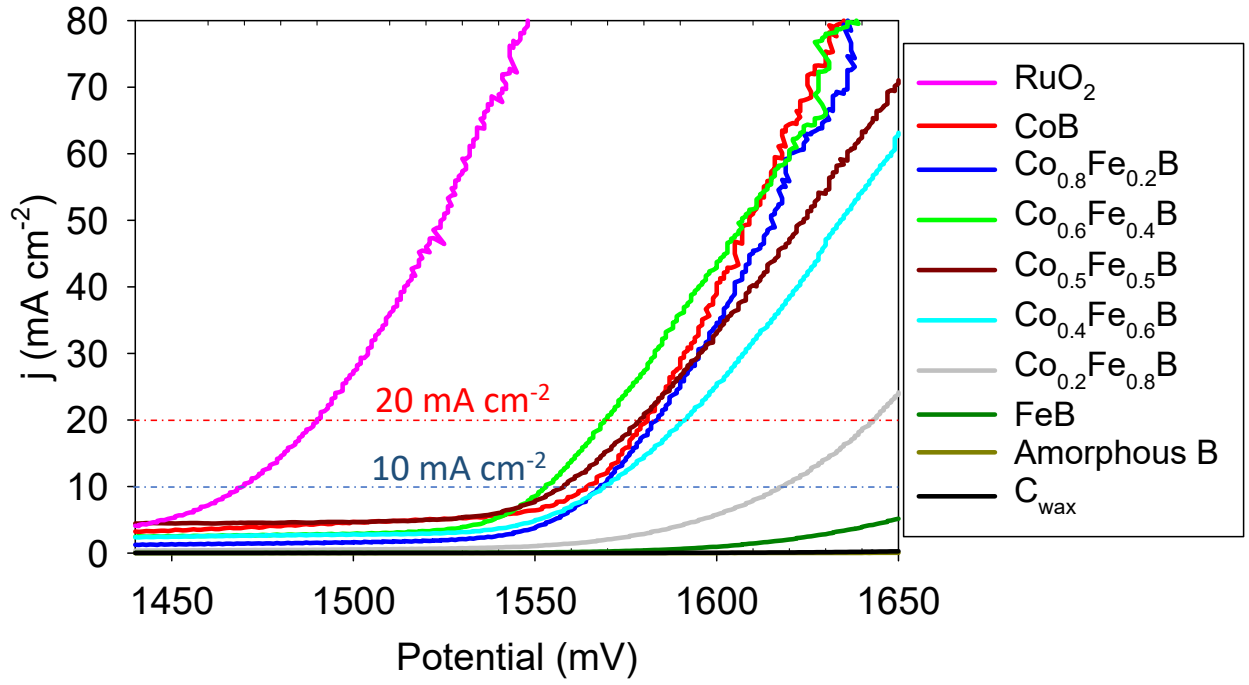

Figure S27. OER LSV overlay plots for metal borides with 85% iR compensation at 5 mV s^{-1} scan rate. A representative LSV run from 10 LSVs with iR on is shown in the graph. The working electrodes are metal boride powders embedded on C_{wax} tips.

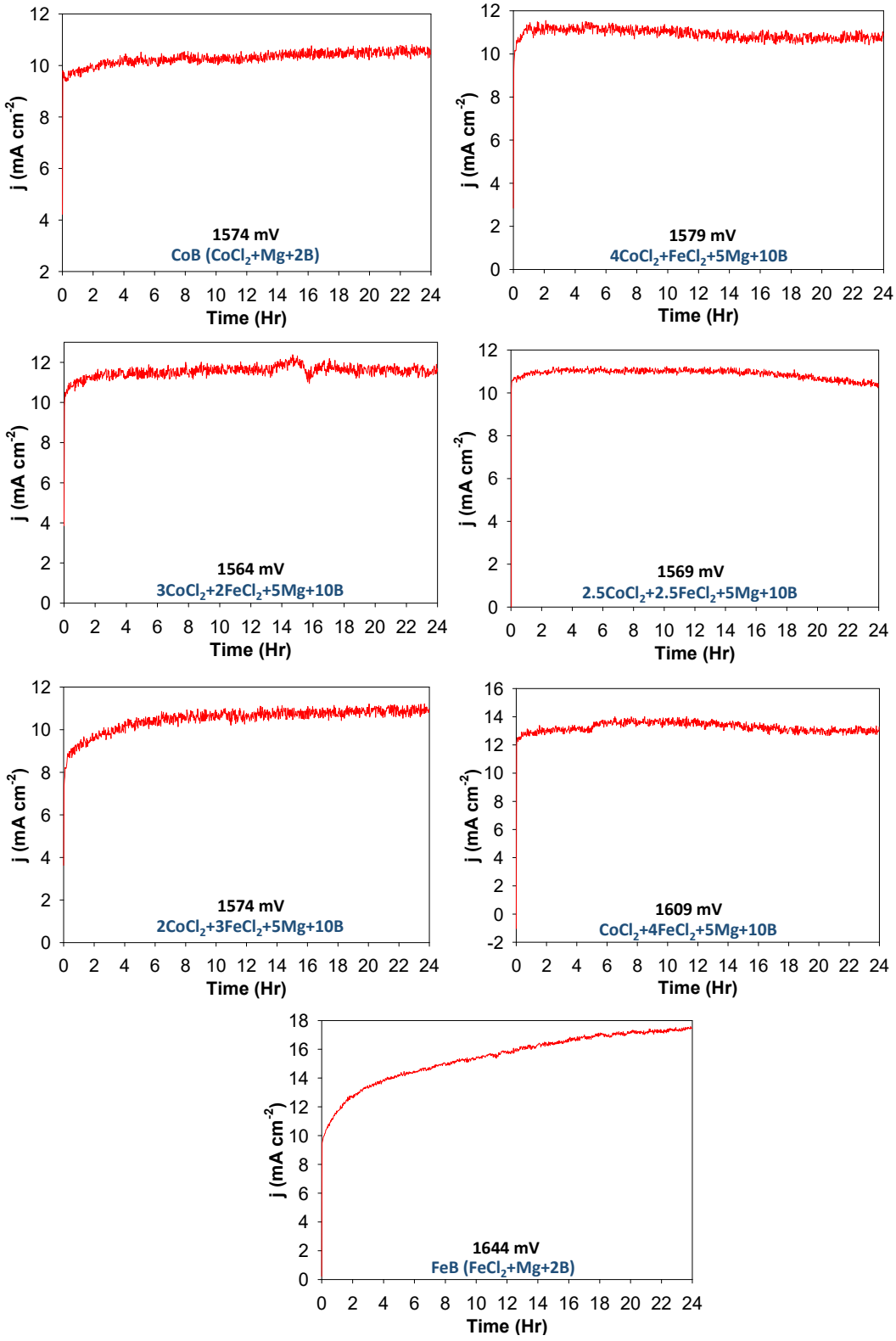

Figure S28. Applied positive potential OER chronoamperometry data (current versus time at constant potential) for metal borides in 1.0 M KOH for 24 hrs. The potentials used are indicated and were chosen to ideally sustain 10 mA/cm^2. The working electrodes are metal boride powders embedded on C_{wax} tips.

Table S12. Summary of post-chronoamperometry OER electrocatalysis of SSM synthesized metal borides in 1.0 M KOH (average of 10 HERs were reported in the table).

Sample	(η_{10}) (mV)[1]	(η_{20}) (mV)	Tafel (mV/dec)
CoB	1572.3±2.9 (1547.9±2.9)	1603.1±2.2 (1554.5±2.4)	102 (48)
$Co_{0.8}Fe_{0.2}B$	1588.4±2.3 (1570.2±2.4)	1621.3±3.3 (1584.9±3.1)	79 (50)
$Co_{0.6}Fe_{0.4}B$	1571.0±1.4 (1562.3±1.3)	1603.1±1.7 (1584.9±1.7)	81 (63)
$Co_{0.5}Fe_{0.5}B$	1577.5±2.0 (1557.4±1.8)	1614.5±2.5 (1574.0±2.7)	109 (55)
$Co_{0.4}Fe_{0.6}B$	1590.2±3.6 (1575.7±3.7)	1626.1±4.7 (1597.0±4.9)	99 (67)
$Co_{0.2}Fe_{0.8}B$	1622.4±6.0 (1607.9±5.9)	1656.7±8.3 (1627.7±8.2)	72 (60)
FeB	1654.7±4.6 (1633.7±4.5)	1690.4±6.0 (1648.8±5.9)	53 (45)

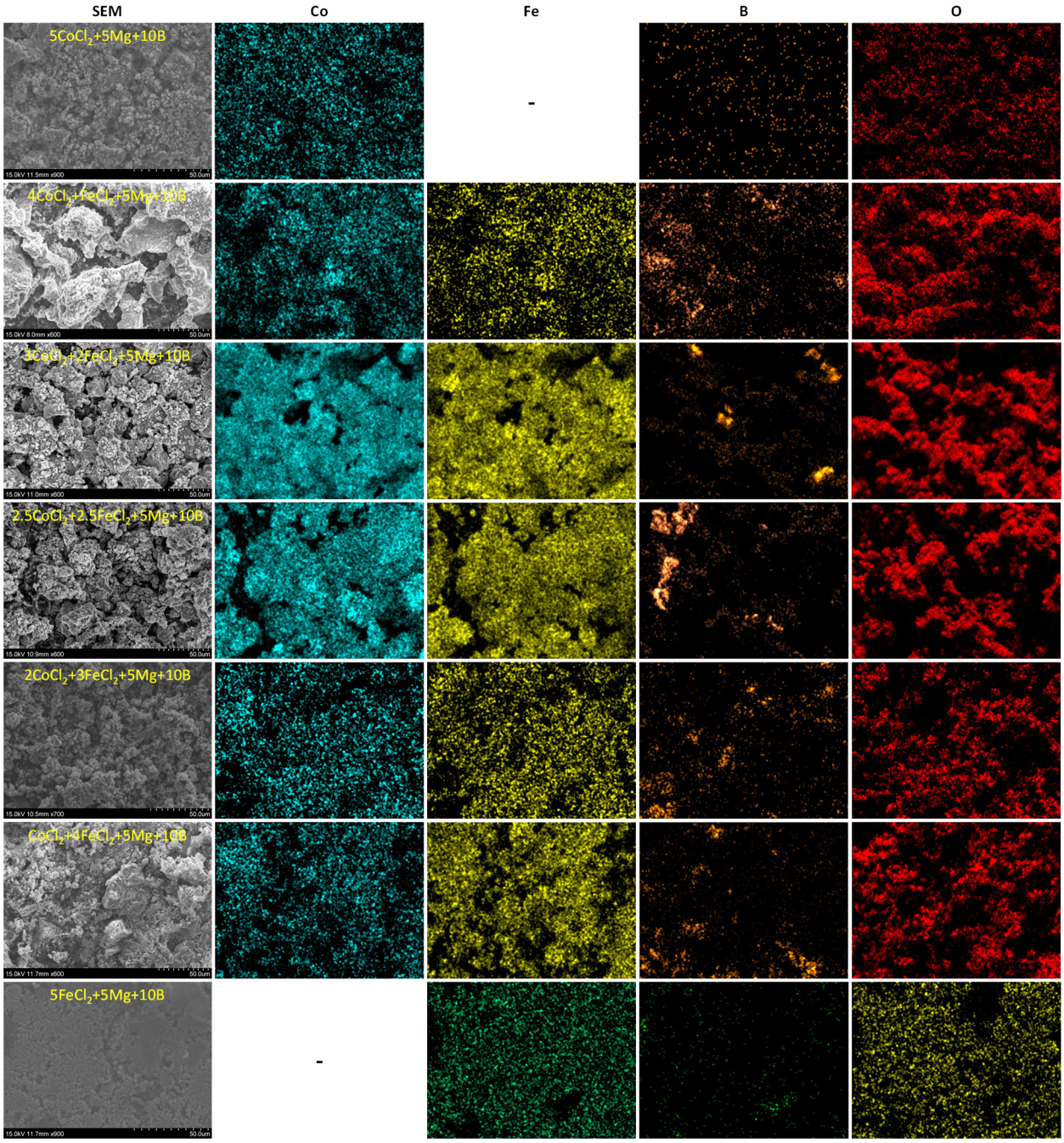

Figure S29. Post-positive potential OER chronoamperometry EDS maps of CoB, FeB, and $Co_{1-x}Fe_xB$ solid-solutions. Images are from powders embedded on C_{wax} tip.

Reference

(1) Rao, L.; Gillan, E. G.; Kaner, R. B. Rapid synthesis of transition-metal borides by solid-state metathesis. *J. Mater. Res.* **1995**, *10* (2), 353-361.
(2) Lupinetti, A. J.; Fife, J. L.; Garcia, E.; Dorhout, P. K.; Abney, K. D. Low-Temperature Synthesis of Uranium Tetraboride by Solid-State Metathesis Reactions. *Inorg. Chem.* **2002**, *41* (9), 2316-2318. DOI: 10.1021/ic015607a.
(3) Aprea, A.; Maspero, A.; Figini Albisetti, A.; Giunchi, G. Synthesis of Alkaline-earth hexaborides, MB_6 (M = Ca, Ba, Sr), by a solid state metathesis (SSM) reaction. *Solid State Sci.* **2012**, *14* (11-12), 1587-1590. DOI: 10.1016/j.solidstatesciences.2012.03.002.
(4) Aprea, A.; Maspero, A.; Masciocchi, N.; Guagliardi, A.; Albisetti, A. F.; Giunchi, G. Nanosized rare-earth hexaborides: Low-temperature preparation and microstructural analysis. *Solid State Sci.* **2013**, *21*, 32-36. DOI: 10.1016/j.solidstatesciences.2013.04.001.
(5) Jothi, P. R.; Zhang, Y.; Scheifers, J. P.; Park, H.; Fokwa, B. P. T. Molybdenum diboride nanoparticles as a highly efficient electrocatalyst for the hydrogen evolution reaction. *Sustainable Energy Fuels* **2017**, *1*, 1928-1934. DOI: 10.1039/c7se00397h.
(6) Li, Q.; Zou, X.; Ai, X.; Chen, H.; Sun, L.; Zou, X. Revealing Activity Trends of Metal Diborides Toward pH-Universal Hydrogen Evolution Electrocatalysts with Pt-Like Activity. *Adv. Energy Mater.* **2019**, *9*, 1803369. DOI: 10.1002/aenm.201803369.
(7) Ai, X.; Zou, X.; Chen, H.; Su, Y.; Feng, X.; Li, Q.; Liu, Y.; Zhang, Y.; Zou, X. Transition-Metal-Boron Intermetallics with Strong Interatomic d-sp Orbital Hybridization for High-Performance Electrocatalysis. *Angew. Chem. Int. Ed.* **2020**, *59* (10), 3961-3965. DOI: 10.1002/anie.201915663.
(8) Zou, X.; Wang, L.; Ai, X.; Chen, H.; Zou, X. Crystal phase-dependent electrocatalytic hydrogen evolution performance of ruthenium-boron intermetallics. *Chem. Commun.* **2020**, *56* (20), 3061-3064. DOI: 10.1039/d0cc00070a.
(9) Abeysinghe, J. P.; Kolln, A. F.; Gillan, E. G. Rapid and Energetic Solid-State Metathesis Reactions for Iron, Cobalt, and Nickel Boride Formation and Their Investigation as Bifunctional Water Splitting Electrocatalysts. *ACS Mater. Au* **2022**, *2* (4), 489-504. DOI: 10.1021/acsmaterialsau.1c00079.
(10) Binnewies, M.; Milke, E. *Thermochemical Data of Elements and Compounds*; Weinheim, 1999.
(11) Kubaschewski, O.; Alcock, C. B. *Metallurgical Thermochemistry*; Pergamon Press Inc., Maxwell House, 1979. *CRC Handbook of Chemistry and Physics, 102nd Edition (Internet Version 2021)*; Rumble, J. R., Ed.; CRC Press/Taylor & Francis. NIST Chemistry Webbook. Standard Reference Database. (accessed 7/5/2021).
(12) Li, H.; Wen, P.; Li, Q.; Dun, C.; Xing, J.; Lu, C.; Adhikari, S.; Jiang, L.; Carroll, D. L.; Geyer, S. M. Earth-Abundant Iron Diboride (FeB_2) Nanoparticles as Highly Active Bifunctional Electrocatalysts for Overall Water Splitting. *Adv. Energy Mater.* **2017**, *7* (17), 1700513. DOI: 10.1002/aenm.201700513.
(13) Ma, X.; Wen, J.; Zhang, S.; Yuan, H.; Li, K.; Yan, F.; Zhang, X.; Chen, Y. Crystal Co_xB (x = 1-3) Synthesized by a Ball-Milling Method as High-Performance Electrocatalysts for the Oxygen Evolution Reaction. *ACS Sustainable Chem. Eng.* **2017**, *5* (11), 10266-10274. DOI: 10.1021/acssuschemeng.7b02281.
(14) Klemenz, S.; Schuch, J.; Hawel, S.; Zieschang, A.-M.; Kaiser, B.; Jaegermann, W.; Albert, B. Synthesis of a Highly Efficient Oxygen-Evolution Electrocatalyst by Incorporation of Iron into Nanoscale Cobalt Borides. *ChemSusChem* **2018**, *11* (18), 3150-3156. DOI: 10.1002/cssc.201801547.
(15) Masa, J.; Weide, P.; Peeters, D.; Sinev, I.; Xia, W.; Sun, Z.; Somsen, C.; Muhler, M.; Schuhmann, W. Amorphous Cobalt Boride (Co_2B) as a Highly Efficient Nonprecious Catalyst for Electrochemical Water Splitting: Oxygen and Hydrogen Evolution. *Adv. Energy Mater.* **2016**, *6*, 1502313. DOI: 10.1002/aenm.201502313.

(16) Xu, X.; Deng, Y.; Gu, M.; Sun, B.; Liang, Z.; Xue, Y.; Guo, Y.; Tian, J.; Cui, H. Large-scale synthesis of porous nickel boride for robust hydrogen evolution reaction electrocatalyst. *Appl. Surf. Sci.* **2019**, *470*, 591-595. DOI: 10.1016/j.apsusc.2018.11.127.
(17) Masa, J.; Piontek, S.; Wilde, P.; Antoni, H.; Eckhard, T.; Chen, Y.-T.; Muhler, M.; Apfel, U.-P.; Schuhmann, W. Ni-Metalloid (B, Si, P, As, and Te) Alloys as Water Oxidation Electrocatalysts. *Adv. Energy Mater.* **2019**, *9*, 1900796. DOI: 10.1002/aenm.201900796.
(18) Jothi, P. R.; Zhang, Y.; Yubuta, K.; Culver, D. B.; Conley, M.; Fokwa, B. P. T. Abundant Vanadium Diboride with Graphene-like Boron layers for Hydrogen Evolution. *ACS Appl. Energy Mater.* **2019**, *2* (1), 176-181. DOI: 10.1021/acsaem.8b01615.
(19) Mazanek, V.; Nahdi, H.; Luxa, J.; Sofer, Z.; Pumera, M. Electrochemistry of layered metal diborides. *Nanoscale* **2018**, *10* (24), 11544-11552. DOI: 10.1039/c8nr02142b.
(20) Kirshenbaum, M. J.; Richter, M. H.; Dasog, M. Electrochemical Water Oxidation in Acidic Solution Using Titanium Diboride (TiB_2) Catalyst. *ChemCatChem* **2019**, *11* (16), 3877-3881. DOI: 10.1002/cctc.201801736.
(21) Lim, C. S.; Sofer, Z.; Mazanek, V.; Pumera, M. Layered titanium diboride: towards exfoliation and electrochemical applications. *Nanoscale* **2015**, *7* (29), 12527-12534. DOI: 10.1039/c5nr02692j.
(22) Zhuang, Z.; Li, Y.; Li, Z.; Lv, F.; Lang, Z.; Zhao, K.; Zhou, L.; Moskaleva, L.; Guo, S.; Mai, L. MoB/g-C_3N_4 Interface Materials as a Schottky Catalyst to Boost Hydrogen Evolution. *Angew. Chem. Int. Ed.* **2018**, *57* (2), 496-500. DOI: 10.1002/anie.201708748.
(23) Wang, Y.; Mayorga-Martinez, C. C.; Chia, X. Y.; Sofer, Z.; Latiff, N. M.; Pumera, M. Bipolar Electrochemistry as a Simple Synthetic Route toward Nanoscale Transition of Mo_2B_5 and W_2B_5 for Enhanced Hydrogen Evolution Reaction. *ACS Sustainable Chem. Eng.* **2019**, *7* (14), 12148-12159. DOI: 10.1021/acssuschemeng.9b01251.
(24) Guo, F.; Wu, Y.; Ai, X.; Chen, H.; Li, G.-D.; Chen, W.; Zou, X. A class of metal diboride electrocatalysts synthesized by a molten salt-assisted reaction for the hydrogen evolution reaction. *Chem. Commun.* **2019**, *55* (59), 8627-8630. DOI: 10.1039/c9cc03638e.
(25) Nsanzimana, J. M. V.; Peng, Y.; Xu, Y. Y.; Thia, L.; Wang, C.; Xia, B. Y.; Wang, X. An Efficient and Earth-Abundant Oxygen-Evolving Electrocatalyst Based on Amorphous Metal Borides. *Adv. Energy Mater.* **2018**, *8*, 1701475. DOI: 10.1002/aenm.201701475.
(26) Zieschang, A.-M.; Bocarsly, J. D.; Schuch, J.; Reichel, C. V.; Kaiser, B.; Jaegermann, W.; Seshadri, R.; Albert, B. Magnetic and Electrocatalytic Properties of Nanoscale Cobalt Boride, Co_3B. *Inorg. Chem.* **2019**, *58*, 16609-16617. DOI: 10.1021/acs.inorgchem.9b02617.
(27) Gupta, S.; Patel, N.; Miotello, A.; Kothari, D. C. Cobalt-Boride: An efficient and robust electrocatalyst for Hydrogen Evolution Reaction. *J. Power Sources* **2015**, *279*, 620-625. DOI: 10.1016/j.jpowsour.2015.01.009.
(28) Gupta, S.; Patel, N.; Fernandes, R.; Kadrekar, R.; Dashora, A.; Yadav, A. K.; Bhattacharyya, D.; Jha, S. N.; Miotello, A.; Kothari, D. C. Co–Ni–B nanocatalyst for efficient hydrogen evolution reaction in wide pH range. *Appl. Catal. B* **2016**, *192*, 126-133. DOI: 10.1016/j.apcatb.2016.03.032.
(29) Li, Y.; Xu, H.; Huang, H.; Gao, L.; Zhao, Y.; Ma, T. Synthesis of Co–B in porous carbon using a metal-organic framework (MOF) precursor: A highly efficient catalyst for the oxygen evolution reaction. *Electrochem. Commun.* **2018**, *86*, 140-144.
(30) Jiang, Y.; Fang, Y.; Chen, C.; Ni, P.; Kong, B.; Song, Z.; Lu, Y.; Niu, L. Amorphous Cobalt Boride Nanosheets Directly Grown on Nickel Foam: Controllable Alternately Dipping Deposition for Efficient Oxygen Evolution. *ChemElectroChem* **2019**, *6* (14), 3684-3689. DOI: 10.1002/celc.201900897.
(31) Hao, W.; Wu, R.; Zhang, R.; Ha, Y.; Chen, Z.; Wang, L.; Yang, Y.; Ma, X.; Sun, D.; Fang, F.; et al. Electroless Plating of Highly Efficient Bifunctional Boride-Based Electrodes toward Practical Overall Water Splitting. *Adv. Energy Mater.* **2018**, *8* (26), 1801372. DOI: 10.1002/aenm.201801372.

(32) Tan, T.; Han, P.; Cong, H.; Cheng, G.; Luo, W. An Amorphous Cobalt Borate Nanosheet-Coated Cobalt Boride Hybrid for Highly Efficient Alkaline Water Oxidation Reaction. *ACS Sustainable Chem. Eng.* **2019**, *7*, 5620-5625. DOI: 10.1021/acssuschemeng.9b00258.
(33) Arivu, M.; Masud, J.; Umapathi, S.; Nath, M. Facile synthesis of Ni_3B/rGO nanocomposite as an efficient electrocatalyst for the oxygen evolution reaction in alkaline media. *Electrochem. Commun.* **2018**, *86*, 121-125. DOI: 10.1016/j.elecom.2017.12.002.
(34) Masa, J.; Andronescu, C.; Antoni, H.; Sinev, I.; Seisel, S.; Elumeeva, K.; Barwe, S.; Marti-Sanchez, S.; Arbiol, J.; Cuenya, B. R.; et al. Role of Boron and Phosphorus in Enhanced Electrocatalytic Oxygen Evolution by Nickel Borides and Nickel Phosphides. *ChemElectroChem* **2019**, *6*, 235-240. DOI: 10.1002/celc.201800669.
(35) Zeng, M.; Wang, H.; Zhao, C.; Wei, J.; Qi, K.; Wang, W.; Bai, X. Nanostructured Amorphous Nickel Boride for High-Efficiency Electrocatalytic Hydrogen Evolution over a Broad pH Range. *ChemCatChem* **2016**, *8* (4), 708-712. DOI: 10.1002/cctc.201501221.
(36) Cao, M.; Zhang, X.; Qin, J.; Liu, R. Enhancement of Hydrogen Evolution Reaction Performance of Graphitic Carbon Nitride with Incorporated Nickel Boride. *ACS Sustainable Chem. Eng.* **2018**, *6* (12), 16198-16204. DOI: 10.1021/acssuschemeng.8b02994.
(37) Zhao, S.; Xu, S.; Yao, J.; Chen, N.; Gong, Y.; Zhang, X.; Hao, X.; Zhang, L.; Pei, C.; Tian, R.; et al. Elucidating the reaction pathway of crystalline multi-metal borides for highly efficient oxygen-evolving electrocatalysts. *J. Mater. Chem. A* **2022**, *10* (3), 1569-1578. DOI: 10.1039/d1ta09078j.
(38) Zou, X.; Zhang, W.; Zhou, X.; Song, K.; Ge, X.; Zheng, W. The surface of metal boride tinted by oxygen evolution reaction for enhanced water electrolysis. *J. Energy Chem.* **2022**, *72*, 509-515. DOI: 10.1016/j.jechem.2022.05.0392095-4956.
(39) Patil, K.; Babar, P.; Li, X.; Karade, V.; Kim, S.; Jang, S. Y.; Bhoite, P.; Kim, J. H. Co–Fe–B Nanochain Electrocatalysts for Oxygen Evolution at High Current Density. *ACS Appl. Nano Mater.* **2022**, *5* (5), 6260-6267. DOI: 10.1021/acsanm.2c00312.
(40) Liu, X.; He, G.; Liu, H.; Zhu, Y.; Xiao, J.; Han, L. Boron-doped cobalt-iron bimetal phosphides nanosheets for enhanced oxygen evolution. *J. Alloys Compd.* **2022**, *893*. DOI: 10.1016/j.jallcom.2021.162208.
(41) Wang, N.; Xu, A.; Ou, P.; Hung, S. F.; Ozden, A.; Lu, Y. R.; Abed, J.; Wang, Z.; Yan, Y.; Sun, M. J.; et al. Boride-derived oxygen-evolution catalysts. *Nat. Commun.* **2021**, *12* (1), 6089. DOI: 10.1038/s41467-021-26307-7.
(42) Qiang, C.; Zhang, L.; He, H.; Liu, Y.; Zhao, Y.; Sheng, T.; Liu, S.; Wu, X.; Fang, Z. Efficient electrocatalytic water splitting by bimetallic cobalt iron boride nanoparticles with controlled electronic structure. *J. Colloid Interface Sci.* **2021**, *604*, 650-659. DOI: 10.1016/j.jcis.2021.07.024.
(43) Nsanzimana, J. M. V.; Gong, L.; Dangol, R.; Reddu, V.; Jose, V.; Xia, B. Y.; Yan, Q.; Lee, J. M.; Wang, X. Tailoring of Metal Boride Morphology via Anion for Efficient Water Oxidation. *Adv. Energy Mater.* **2019**, *9* (28), 1901503. DOI: 10.1002/aenm.201901503.
(44) Mann, D. K.; Xu, J.; Mordvinova, N. E.; Yannello, V.; Ziouani, Y.; Gonzalez-Ballesteros, N.; Sousa, J. P. S.; Lebedev, O. I.; Kolen'ko, Y. V.; Shatruk, M. Electrocatalytic water oxidation over $AlFe_2B_2$. *Chem. Sci.* **2019**, *10* (9), 2796-2804. DOI: 10.1039/c8sc04106g.
(45) Li, Y.; Huang, B.; Sun, Y.; Luo, M.; Yang, Y.; Qin, Y.; Wang, L.; Li, C.; Lv, F.; Zhang, W.; et al. Multimetal Borides Nanochains as Efficient Electrocatalysts for Overall Water Splitting. *Small* **2019**, *15*, 1804212. DOI: 10.1002/smll.201804212.
(46) Sheng, M.; Wu, Q.; Wang, Y.; Liao, F.; Zhou, Q.; Hou, J.; Weng, W. Network-like porous Co-Ni-B grown on carbon cloth as efficient and stable catalytic electrodes for hydrogen evolution. *Electrochem. Commun.* **2018**, *93*, 104-108. DOI: 10.1016/j.elecom.2018.06.017.

(47) Gupta, S.; Patel, N.; Fernandes, R.; Hanchate, S.; Miotello, A.; Kothari, D. C. Co-Mo-B Nanoparticles as a non-precious and efficient Bifunctional Electrocatalyst for Hydrogen and Oxygen Evolution. *Electrochim. Acta* **2017**, *232*, 64-71. DOI: 10.1016/j.electacta.2017.02.100.
(48) Chen, H.; Ouyang, S.; Zhao, M.; Li, Y.; Ye, J. Synergistic Activity of Co and Fe in Amorphous Co*x*-Fe-B Catalyst for Efficient Oxygen Evolution Reaction. *ACS Appl. Mater. Interfaces* **2017**, *9* (46), 40333-40343. DOI: 10.1021/acsami.7b13939.